Chaos
An Interdisciplinary Journal of Nonlinear Science

RESEARCH ARTICLE | OCTOBER 20 2026

Data-driven reduced modeling of delayed dynamical systems via spectral submanifolds

Giacomo Abbasciano ; Gergely Buza ; George Haller

Check for updates

Chaos 36, 103103 (2026)
https://doi.org/10.1063/5.0344712

View Online
Export Citation

Articles You May Be Interested In

Parametric spectral submanifolds across Hopf bifurcations with applications to fluid dynamics
Chaos (October 2026)

Data-driven modeling and forecasting of chaotic dynamics on inertial manifolds constructed as spectral submanifolds
Chaos (March 2024)

General oblique projections for model reduction via spectral submanifolds
Chaos (May 2026)

10 November 2026 11:30:50

AIP Publishing
Chaos
Special Topics Open for Submissions
Learn More

AIP Publishing

Data-driven reduced modeling of delayed dynamical systems via spectral submanifolds

Cite as: Chaos 36, 103103 (2026); doi: 10.1063/5.0344712
Submitted: 21 May 2026 · Accepted: 11 September 2026 ·
Published Online: 20 October 2026

View Online Export Citation CrossMark

Giacomo Abbasciano, Gergely Buza, and George Haller[a)]

AFFILIATIONS

Department of Mechanical and Process Engineering, ETH Zurich, 8092 Zurich, Switzerland

[a)]Author to whom correspondence should be addressed: georgehaller@ethz.ch

ABSTRACT

We show how the recent extension of spectral submanifold (SSM) theory to delay differential equations (DDEs) enables data-driven model reduction of nonlinear delay systems. First, using a scalar DDE with a single discrete delay, we compare equation-based and data-driven SSM reductions, to illustrate the need for the latter. We then use the same algorithm to obtain purely data-driven, SSM-reduced, delay-free ordinary differential equation models for several nonlinear delayed systems. Our approach requires no information about the form of the underlying DDE, or about the number and magnitude of the delays it contains. Our SSM-reduced, low-dimensional models remain predictive even for chaotic dynamics. We also illustrate the use of parametric SSM reduction to capture bifurcations in systems with both distributed and discrete delays. Finally, we extend the theoretical underpinning of delayed SSM reductions to non-autonomous systems with periodic delays and apply these results to experimental data from a control system with feedback delay and quantization.

© 2026 Author(s). All article content, except where otherwise noted, is licensed under a Creative Commons Attribution (CC BY) license (https://creativecommons.org/licenses/by/4.0/). https://doi.org/10.1063/5.0344712

10 November 2026 11:30:50

Data-driven methods for constructing predictive models are increasingly important for complex dynamical systems whose full equations of motion are unknown. Many such systems display dominant, low-dimensional behavior confined to attracting spectral submanifolds (SSMs), which are nonlinear continuation of dominant linear modes of the system. The mathematical theory of SSMs has only been extended recently to delay dynamical systems, i.e., to systems whose evolution depends on their past states. Here, we develop a methodology to identify SSMs in such systems purely from numerical or experimental data.

I. INTRODUCTION

Many systems in nature and engineering exhibit dynamics that depend on past states. In epidemiology, the spread of diseases is delayed by the incubation time,[1] and delays in vaccine production can destabilize the disease-free equilibrium. In autonomous vehicle control,[2–4] delays arise from human reaction times. More generally, feedback-control systems involve delays due to measurement, computation, and zero-order hold (ZOH) effects.[5–8]

Such delays can often be neglected without compromising model performance. Indeed, for sufficiently small delays, the dominant dynamics remain close to those of the corresponding delay-free system. More specifically, as shown in Ref. 9, the spectrum of the delayed system retains the eigenvalues of the undelayed system, which remain dominant for small delays, while infinitely many additional eigenvalues originate from the leftmost part of the complex plane, whose associated dynamics decay rapidly. This explains the effectiveness of low-dimensional models and linear controllers that do not account for small delays, enabling the construction of such low-dimensional yet accurate models for computational cost reduction. However, as the delay increases, the additional eigenvalues move toward the imaginary axis and may become dominant, eliminating the spectral gap between delay-induced and undelayed eigenvalues. These may then cross the imaginary axis, leading to bifurcations that are absent in the undelayed system.[8]

At the same time, delay differential equations (DDEs) are inherently infinite-dimensional, because their phase space is the Banach space of continuous history functions. Consequently, they can exhibit richer dynamics than ordinary differential equations (ODEs) of the same nominal dimension. Indeed, even scalar delay equations may display chaotic dynamics.[10]

Beyond delay effects, nonlinearizable phenomena, such as the coexistence of isolated steady states and bifurcations, are ubiquitous in applied sciences and engineering. Spectral submanifolds

© Author(s) 2026

(SSMs) enable the construction of mathematically justified reduced models for such nonlinearizable dynamics on the slowest family of low-dimensional, normally attracting invariant manifolds emanating from a hyperbolic fixed point. These manifolds form a family whose members all have the same dimension and are tangent to a direct sum of dominant eigenspaces at the fixed point, i.e., to a slow spectral subspace (see Refs. 11–13).

Prior work based on SSM has analyzed and modeled such behaviors in systems including turbulent flows,[14,15] fluid sloshing,[13,16] nonsmooth dynamics,[17–19] control of soft robots,[20–24] alongside global and local bifurcations.[19,25]

Equation-driven approaches for nonlinear delay systems have been extensively employed. Most pertinent to this work, classic center-manifold reduction[26,27] has recently been formally extended to SSMs directly in the function space,[28] without the need for discretization of the delay equation. A rigorous existence and regularity result for such SSMs in delay systems has subsequently been established in Ref. 9. Despite its interpretability, equation-driven SSM-reduction is computationally demanding and therefore typically limited to low-dimensional systems, as the cost increases with both the SSM dimension and the polynomial order desired to parametrize the manifold and reduced dynamics. Moreover, equation-driven SSM reduction requires full knowledge of the governing equations, parameters, and delays, which is often unavailable in real-world applications.

These limitations of equation-driven model reduction motivate the development of data-driven methods for modeling delay systems. Approaches such as neural delay differential equations (NDDEs) and SINDy-based[29] methods have been successfully applied to systems with multiple discrete delays.[30–34] These methods are formulated under different assumptions on the available prior knowledge about the delays. For instance, when the number and magnitude of the delays are not known a priori, E-SINDy estimates the delay magnitudes from data after specifying an upper bound on their number.[32] In the absence of any prior knowledge of the number of delays, P-SINDy instead estimates the maximum delay directly from data. This leads to a trajectory-based formulation that focuses on reproducing the observed trajectory and extending the simulation beyond the measurement window, rather than explicitly identifying the right-hand side of the system.[32]

In addition, these approaches rely on the explicit form of the DDE to select basis functions. The choice of these functions may in turn strongly impact the performance of the algorithm.[32] This restriction is particularly relevant when the full dynamics include non-polynomial terms, such as those in the Mackey–Glass equation.[32] Finally, NDDEs provide a neural-network-based framework and likewise require delay values to be identified from data when they are not known a priori.[30–32]

Here, we show how SSM-based reduction can be extended to data-driven settings for DDEs. This approach enables the modeling of nonlinear phenomena, including coexisting isolated steady states and bifurcations, directly from observed data. In particular, the specific form of the DDE plays no role and number and magnitude of the delays need not be *a priori* known. As long as the delayed system has class C^1 governing equations, SSMs always exist with at least C^1 regularity and are tangent to finite-dimensional slow spectral subspaces in the infinite-dimensional phase space of a generally unknown DDE. In order to handle control applications with ZOH effects, we also prove an extension of the SSM results of Ref. 9 to systems with periodic delays.

This paper is organized as follows. Section II recalls the settings for nonlinear autonomous DDEs and the main theoretical results on their SSMs and extends the theory to periodically delayed DDEs. Section III presents the data-driven procedures used for SSM-based model reduction, with particular emphasis on the estimation of the quantities required directly from data. Section IV demonstrates the proposed methodology through a sequence of examples. It begins by comparing equation-driven and data-driven SSM reductions for the Hutchinson equation, thereby motivating the need for data-driven approaches. The section then applies data-driven SSM reduction to numerically simulated systems of increasing complexity, including single-delay systems with limit cycles, multiple-delay systems exhibiting chaotic dynamics, and a distributed-delay system with multiple saddle-node bifurcations of limit cycles, analyzed through parametric SSMs. Finally, the theoretical extension to periodically delayed DDEs is illustrated on experimental data involving delay and quantization effects typical of digital controllers.

II. EXISTENCE OF SSMs FOR NONLINEAR DDEs

In this section, we provide a high-level overview of delay differential equations on infinite-dimensional spaces and introduce the relevant theory, following Refs. 27, 35, before recalling the main results of Ref. 9 on the existence and regularity of SSMs in delay systems. Finally, we show how these results can be applied to justify and carry out data-driven SSM reduction in such systems.

A. Analogies between ODEs and differential equations on infinite dimensional spaces

We recall the notion of strongly continuous semigroups,[35] fundamental to the study of linear evolutionary systems on Banach spaces (in particular, delay equations). In finite dimensions, they coincide with matrix exponentials arising from first-order linear ODEs. This extends naturally to a Banach space X. Specifically, if $A \in \mathcal{L}(X)$ is bounded, where $\mathcal{L}(X)$ is the space of bounded linear operators acting on X, the Cauchy problem

$$\dot{x} = Ax, \qquad x(0) = x_0,$$

admits the unique solution

$$x(t) = e^{tA}x_0 = \sum_{k=0}^{\infty} \frac{t^k}{k!} A^k x_0, \quad t \in \mathbb{R}.$$

For unbounded operators, typical in PDEs and DDEs, this representation may fail and solutions may exist only for $t \geq 0$. It is, therefore, preferable to describe the dynamics via solution operators, leading to the notion of strongly continuous semigroups, namely, a family of linear operators $T : [0, \infty) \to \mathcal{L}(X)$ satisfying

$$T(0) = I, \quad T(t+s) = T(t)T(s), \quad t, s \geq 0$$

and

$$\lim_{t \downarrow 0} \|T(t)x - x\| = 0, \quad \text{for all } x \in X. \tag{1}$$

10 November 2026 11:30:50

© Author(s) 2026

The classical notions of continuous dependence on time and initial conditions are encoded in (1) and in the boundedness of $T(t)$, respectively.

The infinitesimal generator $A{:}\mathrm{dom}(A) \to X$ of the semigroup $T(t)$ is the linear operator defined on

$$\mathrm{dom}(A) \doteq \left\{ x \in X \;\middle|\; \lim_{\tau \downarrow 0} \frac{T(\tau)x - x}{\tau} \text{ exists} \right\},$$

as

$$Ax \doteq \lim_{\tau \downarrow 0} \frac{T(\tau)x - x}{\tau}, \quad x \in \mathrm{dom}(A).$$

The fundamental qualitative behavior of solutions to nonlinear ordinary differential equations induced by vector fields on open subsets of $\mathbb{R}^n$ is classically described through the notion of the flow map. In the setting of Banach spaces, we have to distinguish the forward time direction, which leads to the notion of a semiflow. Indeed, the backward initial value problem is usually not well posed: backward solutions do not exist or may fail to be unique.[27]

To introduce the concept of a semiflow following Ref. 9, we let X be a Banach space. A family of maps $\{\varphi_t\}_{t\geq 0}$, $\varphi_t{:}X \to X$, is called a *semiflow* on X if

$$\varphi_0 = \mathrm{id}_X,$$

$$\varphi_t \circ \varphi_s = \varphi_{t+s} \quad \text{for all } t, s > 0,$$

and $\{\varphi_t\}_{t\geq 0}$ is jointly continuous in space and time. It is known that DDEs, under mild assumptions, generate semiflows.[27]

B. Existence of SSMs for nonlinear autonomous DDEs

We briefly recall the setting for nonlinear autonomous delay differential equations and the main results from Ref. 9 that will be used in the examples below. We consider the phase space

$$X := C([-\tau, 0]; \mathbb{R}^n),$$

namely, the Banach space of continuous $\mathbb{R}^n$-valued functions on $[-\tau, 0]$, with the supremum norm

$$\|\cdot\|_X := \|\cdot\|_\infty,$$

where $\tau > 0$ represents the maximal delay and $n \in \mathbb{N}$. Let $O \subset X$ be an open set, and let $f: O \to \mathbb{R}^n$ be locally Lipschitz continuous. On X, we study autonomous delay differential equations of the form

$$\dot{x}(t) = f(x_t), \tag{2a}$$

$$x_0 = u. \tag{2b}$$

Here, for each t, the history segment $x_t \in X$ is defined by $x_t(\vartheta) = x(t+\vartheta)$, $\vartheta \in [-\tau, 0]$, while $u \in O$ is the prescribed initial datum. A solution of (2) is a map

$$x: [-\tau, t^*) \to \mathbb{R}^n, \quad t^* \in (0, \infty) \cup \{\infty\},$$

such that (2b) is satisfied, x is continuously differentiable on $(0, t^*)$, and (2a) holds throughout that interval. In addition, the right derivative of $x(t)$ at $t = 0$ must exist and coincide with $f(x_0)$. Classic well-posedness results[27] show that, when f is locally Lipschitz, every initial condition $u \in O$ gives rise to a unique solution of (2). We write $\{\varphi_t\}_{t\geq 0}$ for the semiflow induced by (2).

Assume now that the semiflow φ has an equilibrium at the origin, i.e., $0 \in O$ and $f(0) = 0$. Let A be the infinitesimal generator of the semigroup $t \mapsto D\varphi_t(0)$, and let $\Sigma \subset \sigma(A)$ be a nonempty bounded set of the spectrum with associated spectral projection P_Σ. For simplicity, we also assume that f is of class C^k for some $k \geq 1$. We will use the notation $\sigma(A)$ for the spectrum of a linear operator A, we will denote by P_Σ the spectral projection associated with a bounded spectral subset $\Sigma \subset \sigma(A)$ and its image by $\mathrm{im}(P_\Sigma)$.

Theorem 1 ([9]): *Suppose that a spectral subset Σ is of the form $\Sigma = \{\lambda \in \sigma(A) \mid \mathrm{Re}\,\lambda \geq \gamma\}$ for some $\gamma \in \mathbb{R}$. Then, there exists a neighborhood $U \subset O$ of the stationary state $0 \in O$ and a locally invariant (under the semiflow φ) C^ℓ manifold $W^\Sigma \subset U$ (an SSM) tangent to the spectral subspace $\mathrm{im}(P_\Sigma)$ at 0. Here, the integer $1 \leq \ell \leq k$ is determined by the spectral gap condition*

$$\sup \mathrm{Re}\,(\sigma(A) \setminus \Sigma) < \ell \inf \mathrm{Re}\,\Sigma. \tag{3}$$

Moreover, W^Σ attracts trajectories that remain in U at an exponential rate of γ, synchronized along the leaves of a C^0 foliation.

Trajectories approaching an attracting SSM synchronize exponentially fast with trajectories on the SSM. For each on-SSM trajectory, the off-SSM initial conditions that converge to it most rapidly form its stable fiber. These fibers define a foliation over the SSM that is invariant under the semiflow, although individual leaves need not be invariant.[11,36–38]

We emphasize that the sole assumption for the existence of a C^1 SSM W^Σ is f being C^1. A more detailed and precise treatment can be found in Ref. 9.

C. Existence of SSMs for nonlinear nonautonomous DDEs with periodic delay

We now recall the setting for nonautonomous DDEs with periodic delay and state the corresponding existence and regularity result. Its proof, together with further details, is provided in Appendix C. This result will be applied to a control example in which the periodic delay arises from ZOH.

Let $X := C([-\tau, 0]; \mathbb{R}^n)$; here $\tau > 0$ denotes the maximal delay and $n \in \mathbb{N}$. Let $O \subset X$ denote an open set containing the origin. We consider systems of the form

$$\dot{x}(t) = f(t, x_t), \qquad t \geq s \in \mathbb{R}, \tag{4a}$$

$$x_s = u, \tag{4b}$$

for $f: \mathbb{R} \times O \to \mathbb{R}^n$ continuous, time-periodic, i.e., $f(t+p, u) = f(t, u)$ for some $p > 0$ and all $(t, u) \in \mathbb{R} \times O$, and $f(t, 0) = 0$ for all $t \in \mathbb{R}$. This last requirement is usually achieved by mapping a nontrivial periodic orbit to the origin via a time-periodic change of coordinates. We suppose moreover that $f(t, \cdot)$ is C^k with $k \geq 1$ for all $t \in \mathbb{R}$. We shall also assume that $(t, u) \mapsto D_2^j f(t, u)$ is continuous for all $j \leq k$. Here, $D_2^j f$ denotes the jth partial derivative of f with respect to its second argument.

Equation (4) determines a time-dependent semiflow, $S: \mathcal{D}(S) \to X$, mapping initial conditions $u \in X$ prescribed at time s to their state $S(t, s; u) \in X$ at time t, for $(t, s, u) \in \mathcal{D}(S)$. Here, $\mathcal{D}(S) \subset [s, \infty) \times \mathbb{R}_s \times X$ is the open domain of definition of S [see (C3) and (C4) for the details]. We denote by U the linear part of S and by $\sigma(U)$ the associated Floquet spectrum.

10 November 2026 11:30:50

© Author(s) 2026

To make the statement more concise, we set, for a subset $V \subset O$,

$$\mathcal{U}(V) = \left\{(t,s,u) \in \mathcal{D}(S) \;\middle|\; S([t,s] \times \{s\} \times \{u\}) \subset V\right\},$$

and $\mathcal{U}_{s,u}(V) = \{t \in [s,\infty) \mid (t,s,u) \in \mathcal{U}(V)\}$. Moreover, let us denote

$$X = X_\Sigma(t) \oplus X_{\Sigma'}(t) := \mathrm{im}(P_\Sigma(t)) \oplus \ker(P_\Sigma(t)), \quad t \in \mathbb{R},$$

with projection P_Σ as in Proposition 1.

Theorem 2: *Let $\Sigma = \{\lambda \in \sigma(U) \mid |\lambda| > \gamma\}$ for some $\gamma > 0$, $\gamma \notin |\sigma(U)|$. The following hold.*

(i) (Invariant manifold) *There exists an open neighbourhood $V \subset O$ of 0 and a continuous family of C^1 submanifolds $W_t^\Sigma \subset V$ tangent to $X_\Sigma(t)$ at 0, which is locally invariant under S: If $u \in W_s^\Sigma$, then $S(t,s;u) \in W_t^\Sigma$ for all $(t,s,u) \in \mathcal{U}(V)$.*

(ii) (Smoothness) *If $k > 1$, the smoothness of W_t^Σ is C^ℓ for all $t \in \mathbb{R}$, where ℓ is the maximal $\ell \leq k$ for which*

$$(\sup|\sigma(U)\setminus\Sigma|) < (\inf|\Sigma|)^\ell$$

holds.

(iii) (Attractivity) *There exist a continuous map $\pi_t : V \to W_t^\Sigma$, $t \in \mathbb{R}$, such that*

$$\pi_t \circ S(t,s;u) = S(t,s;\pi_s(u)), \quad \text{for all } (t,s,u) \in \mathcal{U}(V). \tag{5}$$

Moreover, for any $u \in U$ and $s \in \mathbb{R}$, there exists $C > 0$ such that

$$|S(t,s;u) - S(t,s;\pi_s(u))| < Ce^{(t-s)\ln(\gamma)/p}, \quad \text{for all } t \in \mathcal{U}_{s,u}(V). \tag{6}$$

The preimages $\{\pi_t^{-1}(w)\}_{w \in W_t^\Sigma}$ are Lipschitz submanifolds foliating V for each $t \in \mathbb{R}$.

D. Data-driven approximation of SSMs of nonlinear autonomous DDEs with bounded delay

We leverage the existence of finite-dimensional SSMs in the phase space of a DDE to construct data-driven approximations of such manifolds and their topologically conjugate reduced dynamics. Based on Takens' theorem,[39] a diffeomorphic copy of a d-dimensional smooth manifold is embedded with probability one in a finite-dimensional delay embedding space $\mathbb{R}^k$ via delayed non-degenerate observables of dimension $k > 2d$.

Specifically, time series of observables are used through the SSMLearn algorithm[13] to reconstruct a manifold at $\vartheta = 0$, that is, at the present time, together with its ϑ-independent reduced dynamics. The result is a low-dimensional system of ODEs that captures the dominant behavior after transient decay to the SSM, which takes place exponentially fast along the stable foliation over the attracting invariant manifold.[9]

As an advantage, reduction to an SSM enables backward-time advection of initial conditions, now represented as finite-dimensional vectors rather than history functions. This is not possible in the full phase space of a DDE, where the solution operator defines only a forward semiflow, since backward-time advection would require specifying future histories as initial conditions. An overview of data-driven SSM modeling for autonomous systems via delay embedding is provided in Appendix A.

III. METHODOLOGY

We describe the data-driven procedures used in this paper to construct SSM-reduced models of delayed dynamical systems. Since the phase space of a delay differential equation (DDE) is infinite dimensional and is therefore not accessible from measurements, the reduction is performed in a finite-dimensional delay-coordinate embedding space constructed from observed time series. Within this space, we identify an SSM, learn the reduced dynamics, and validate the resulting model using trajectory prediction errors or, in the presence of chaotic dynamics, invariant quantities.

A. Correlation dimension estimation from data

For systems exhibiting chaotic dynamics, the dimension of the reduced model must be sufficiently high to embed the chaotic invariant set of interest. We estimate the fractal dimension of the attractor from data using the correlation dimension m introduced by Ref. 40. Since the full phase space of a DDE is infinite dimensional, we first construct a delay-coordinate embedding from a scalar observable x, following Ref. 39, and then estimate the correlation dimension in the resulting finite-dimensional delay-embedding space.

Choosing the embedding dimension k to be at least twice the SSM dimension d, ensures that the SSM $W \subset X$ can be embedded into the delay space.[39] Furthermore, assuming the chaotic attractor is contained in one of the SSMs in X, once in the delay embedding space we invoke[41] to ensure that an orthogonal projection embeds the attractor into a d-dimensional spectral subspace, provided that $d > 2m$. This condition determines the sufficient, not necessary, dimension of the SSM.

Given N embedded data points x_i, the correlation integral is defined as

$$C(l) = \frac{1}{N^2} \#\left\{(i,j) : 1 \leq j < i \leq N,\ \|x_i - x_j\|_2 < l\right\}.$$

For sufficiently small l, the correlation integral scales as

$$C(l) \sim l^m, \quad l \to 0.$$

Hence, m is estimated via linear regression as the slope of the approximately linear scaling region in the log-log plane $(\log l, \log C(l))$.

It suffices to carry out this computation in the delay-embedding space, since Sauer *et al.*[41] guarantee that the delay coordinate map F preserves the correlation dimension m of the attractor A in X, i.e., $\dim(F(A)) = \dim(A)$.

We compare the correlation dimension estimated from trajectories in the delay-embedding space with that estimated after orthogonal projection onto the reduced coordinates to verify that no topological information is lost during the projection.[15]

B. Lyapunov exponent estimation from data

In the presence of chaotic dynamics, we estimate the leading Lyapunov exponent from data in order to validate the SSM-reduced model. The procedure follows,[42] as also used in Ref. 15. The leading Lyapunov exponent quantifies the average exponential separation rate of nearby trajectories, and its reciprocal provides an estimate of the predictability horizon of a chaotic solution.

10 November 2026 11:30:50

© Author(s) 2026

Consider an autonomous system of the form (2a), with initial conditions x_0 and x_0^* of the form (2b), both close to the attractor. Let

$$\varepsilon(0) = x_0^* - x_0, \quad \delta(0) = \|\varepsilon(0)\|_X$$

be the initial perturbation and its norm in the phase space X. The evolution of the perturbation can be locally approximated by

$$\varepsilon(t) = D\varphi_t(x_0)\varepsilon(0).$$

Thus,

$$\delta(t) = \|x^*(t) - x(t)\|_X \approx \|D\varphi_t(x_0)(x_0^* - x_0)\|_X.$$

For sufficiently small perturbations, the dominant exponential growth rate is characterized by

$$\delta(t) \approx \delta(0)e^{\lambda t},$$

where λ denotes the leading Lyapunov growth rate. If $\lambda > 0$, nearby trajectories separate exponentially due to a stretching mechanism, while the folding mechanism of the chaotic attractor keeps trajectories bounded in a compact set.

For DDEs, distances in the full phase space are generally unavailable from data. We therefore compute separations in the delay-coordinate embedding space $\mathbb{R}^k$, using the Euclidean norm. Sauer *et al.*[41] justify estimating the Lyapunov exponent from the image $F(A)$ of the attractor A. To estimate the leading Lyapunov exponent, we first advect an initial condition until the trajectory reaches the chaotic attractor. Denoting this state by $x(t_{Ch})$, we then reset the time origin to $t_{Ch} = t_0$. We initialize N nearby trajectories, typically $N \approx 50$, in a small neighborhood of $x(t_{Ch})$. For the full DDE, we prescribe these initial conditions as constant history functions with values chosen in a small ball around $x(t_{Ch})$. All trajectories are then advanced forward in time. For each pair of trajectories $1 \le j < i \le N$, we compute the separation

$$\delta_{ij}(t) = \|x_i(t) - x_j(t)\|_2$$

in the delay-embedding space. The mean normalized separation is then defined as

$$\frac{\delta(t)}{\delta(0)} = \frac{1}{N_t}\sum_{(i,j)} \frac{\delta_{ij}(t)}{\delta_{ij}(0)},$$

where N_t is the number of trajectory pairs. The leading Lyapunov exponent is obtained by linear regression of $\log(\frac{\delta(t)}{\delta(0)})$ against t, restricted to the initial time interval over which the separation grows approximately exponentially. For validation, we apply the same procedure both to trajectories generated by the full system, when the equations are available, and to trajectories predicted by the SSM-reduced model. When only experimental data are available, this estimation becomes more challenging because one usually has limited control over the initialization of nearby trajectories, especially for DDEs, whose initial conditions are history functions.

C. Invariant measure estimation via probability density functions

To further validate SSM-reduced models in the presence of chaotic dynamics, we compare statistical properties of the chaotic attractor. In particular, we estimate probability density functions (PDFs) of training trajectories in the reduced space and use them to estimate a physically relevant invariant measure of the chaotic attractor, following.[43,44] The agreement between the PDFs obtained from the full system and from the SSM-reduced model indicates that the reduced dynamics reproduces the long-term statistical behavior of the original system, even when test trajectory prediction is no longer meaningful due to high sensitivity to initial conditions.

D. Systematic data-driven SSM reduction for autonomous DDEs

We now summarize the data-driven procedure used to construct SSM-reduced models for autonomous DDEs with bounded delay.

(Step 1) **Verification of the hypothesis of Theorem 1.** For autonomous DDEs of the form introduced in Sec. II B, we first verify the assumptions of Theorem 1. This theorem guarantees the existence of a finite-dimensional invariant manifold emanating from an equilibrium in the infinite-dimensional phase space X, tangent to the selected spectral subspace. As long as the delayed system has class C^1 governing equations, low-dimensional SSMs always exist with at least C^1 regularity. This follows from the fact that we can always choose the spectral subset Σ in Theorem 1 containing the rightmost eigenvalues associated to eigenvectors spanning the spectral subspace $\mathrm{im}(P_\Sigma)$ at 0 with Eq. (3) satisfied with $\ell = 1$.

(Step 2) **Selection of the SSM dimension.** The slow SSM dimension d is determined by the selected slow spectral subspace associated with Σ. This is therefore determined by the configuration of the rightmost eigenvalues in the complex plane. In equation-free settings, this information may be inferred from data using, for example, spectrograms or the observed behavior of trajectories. For chaotic behavior, assuming the chaotic attractor is contained in one of the SSMs in X, once in the delay embedding space we invoke[41] to ensure that an orthogonal projection embeds the attractor into a d-dimensional spectral subspace, provided that $d > 2m$.

(Step 3) **Assessment of SSM smoothness.** After selecting d, the smoothness of the SSM can be estimated from data by comparing the reduced dynamics on a d-dimensional SSM with that on a larger d^*-dimensional SSM, where $d^* > d$. The enlarged spectral set Σ^* includes the slowest real eigenvalue or complex-conjugate pair outside Σ. The spectral gap can then be estimated from the real parts of the eigenvalues inferred from the reduced models. The smoothness of the SSM is ℓ respecting the spectral gap condition (3). If unstable eigenvalues are present, the selected spectral subspace must include all unstable directions for an SSM to be attracting. If Σ contains only unstable eigenvalues, then the corresponding SSM coincides with the (strong) unstable manifold, it is thus unique, and it is as smooth as the full system by Theorem 1. We emphasize that the smoothness of the SSM is not required explicitly for the data-driven SSM reduction to be carried out. Indeed, both the SSM parametrization and the reduced dynamics are

10 November 2026 11:30:50

© Author(s) 2026

approximated directly from data using multivariate polynomial regression in SSMLearn.[13] Consequently, no Taylor expansion needs to be computed.

(Step 4) **Delay-coordinate embedding.**

1. Dimension

Since the full phase space X is infinite-dimensional and hence not reconstructable from finite data, we construct a finite-dimensional delay-coordinate embedding from the available observables, as in (A2). This transforms the data into a delay-embedding space $\mathbb{R}^k$, where k is the embedding dimension. In this space, we seek an embedded SSM, $\widetilde{\mathcal{W}(E)}$, that is diffeomorphic to an SSM, $\mathcal{W}(E) \subset X$, whose existence has been established in Step 1,[39] as detailed in Appendix A 1. Since a generic delay embedding map is an embedding of a d-dimensional invariant manifold once $k > 2d$, the value $2d$ serves as a theoretical lower bound on k.

This bound may be insufficient in practice, as the theorem concerns trajectories lying on the SSM, whereas our data consist of finitely many points that never lie exactly on $\widetilde{\mathcal{W}(E)}$. Ultimately, the optimal embedding dimension for a given problem is the one bringing the invariance error, quantified as the NMTE defined in Eq. (8), below a preselected bound (5% here, and slightly higher for noisy experimental data).

The roles of the lag and the embedding dimension in the geometry of the embedded SSM can be seen by Taylor expanding a delay-embedded scalar time series

$$\mathbf{y}(t) = \begin{pmatrix} s(t) \\ s(t+\Delta t) \\ \vdots \\ s(t+(k-1)\Delta t) \end{pmatrix} \in \mathbb{R}^k$$

around $\Delta t = 0$, which gives

$$\mathbf{y}(t) = \sum_{\ell=0}^{m} \frac{\Delta t^\ell}{\ell!} s^{(\ell)}(t)\mathbf{v}_\ell + \mathcal{O}\big((k-1)^{m+1}\Delta t^{m+1}\big), \qquad \mathbf{v}_\ell = \begin{pmatrix} 0^\ell \\ 1^\ell \\ \vdots \\ (k-1)^\ell \end{pmatrix}. \tag{7}$$

Therefore, up to an error of order $\mathcal{O}((k-1)^{m+1}\Delta t^{m+1})$, the trajectory lies in $\mathcal{P}_m = \mathrm{span}\{\mathbf{v}_0, \ldots, \mathbf{v}_m\} \subseteq \mathbb{R}^k$, yielding a hierarchy of linear approximating subspaces $\mathcal{P}_0 \subset \mathcal{P}_1 \subset \cdots \subset \mathbb{R}^k$. In particular, for sufficiently small Δt, the embedded trajectory lies close to the two-dimensional plane $\mathcal{P}_1 = \mathrm{span}\{\mathbf{v}_0, \mathbf{v}_1\}$, while larger embedding lags require higher-dimensional subspaces for the same accuracy. Since Δt^{m+1} typically dominates the growth of $(k-1)^{m+1}$, a small lag keeps the linear manifold approximation accurate.

One wishes to keep the embedding dimension k close to its theoretical minimal value for several reasons. First, a small k keeps the SSM approximately flat, ensuring that it can be parametrized as a graph over its tangent space; in contrast, an overly large k may induce folding of the manifold, which prevents such a parametrization.[45] Second, a larger k worsens the conditioning of the SSM regression: it adds directions along which the data vary little, especially when the SSM is fitted using portions of training trajectories that already lie very close to the SSM. At the same time, k must be large enough to guarantee an embedding, to provide good predictive accuracy, and, for noisy experimental trajectories, to compensate for off-SSM data points. A dimension above the minimum may also help by making the delayed coordinates less collinear for certain embedding lags.

2. Time lag

On the one hand, the lag must be small enough to satisfy the Nyquist criterion and avoid aliasing, which would entail a loss of information on the underlying dynamics, and small enough to keep the linear approximation of the manifold accurate. On the other hand, it must be large enough to avoid ill-conditioning of the regression, and hence to prevent the model from becoming overly sensitive to small disturbances: when the lag is too small, the delayed coordinates become nearly linearly dependent, as seen from (7), the condition number grows, and small perturbations in the data give rise to very different regression solutions.

(Step 5) **Selection of the SSM polynomial approximation order.**

The $\theta = 0$ slice of an SSM, corresponding to the current-time component of history functions in X, is identified in the delay-embedding space by multivariate polynomial regression, as detailed in Appendix A 2. When the delay-embedding lag Δt is small, trajectories in $\mathbb{R}^k$ tend to flatten,[46] which often makes linear manifold approximations accurate, as can be seen by the expansion (7). In case the invariance error threshold is not met, the polynoimal order can be increased.

(Step 6) **Learning the reduced dynamics.**

The reduced dynamics is approximated from data in the reduced space using multivariate polynomial regression, or radial basis function (RBF) interpolation in the presence of chaotic dynamics when this yields better performance, as detailed in Appendix A 3. The graph-style parametrization of the SSM provides a one-to-one lifting from the reduced coordinates to the delay-coordinate embedding space. This avoids introducing artificial self-intersections in the reconstructed manifold and thereby preserves the uniqueness of solutions for smooth autonomous DDEs.[27]

When polynomial reduced dynamics are used, the polynomial order n_{red} is selected together with the SSM approximation order n_{SSM} by minimizing the normalized mean trajectory error (NMTE) on test data. For a test trajectory $\mathbf{y}_{\mathrm{test}}$ and its SSM-based prediction $\mathbf{y}_{\mathrm{model}}$, the NMTE is defined[13] as

$$\mathrm{NMTE}(n_{\mathrm{SSM}\star}, n_{\mathrm{red}\star}) = \frac{1}{N_p \|\mathbf{y}_{\mathrm{test}}\|_{\max}} \sum_{j=1}^{N_p} \left\| \mathbf{y}^j_{\mathrm{test}}(t_j) - \mathbf{y}^j_{\mathrm{model}}(t_j; n_{\mathrm{SSM}\star}, n_{\mathrm{red}\star}) \right\|. \tag{8}$$

10 November 2026 11:30:50

© Author(s) 2026

The selected orders are then

$$(n_{\mathrm{SSM}}, n_{\mathrm{red}}) = \arg \min_{n_{\mathrm{SSM}\star}, n_{\mathrm{red}\star}} \mathrm{NMTE}(n_{\mathrm{SSM}\star}, n_{\mathrm{red}\star}),$$

where N_p is the number of points of the time series. Too high polynomials lead to overfitting, while too low polynomials lead to underfitting. For chaotic systems, short-time trajectory prediction is not a reliable validation criterion due to high sensitivity to initial conditions. In that case, n_{red} is selected based on the ability of the reduced model to reproduce the statistics of the chaotic attractor, as presented in Step 7.

(Step 7) **Validation of the SSM-reduced model.** For nonchaotic dynamics, model quality is assessed using the NMTE on test trajectories. Each test trajectory is orthogonally projected onto the reduced coordinates to approximate the base point of the leaf of the foliation, the reduced initial condition is advected under the learned reduced dynamics, and the resulting prediction is lifted back to the delay-coordinate embedding space using the learned SSM parametrization. For better approximation of leaves' base points see the works on linear oblique projections[37] and nonlinear oblique projections.[38]

For chaotic dynamics, pointwise trajectory prediction is meaningful only over short times because of sensitive dependence on initial conditions. Therefore, we validate the reduced model by comparing PDFs of training trajectories in the reduced coordinates, comparing leading Lyapunov exponents, and qualitatively assessing whether test trajectories of the reduced model reconstruct the chaotic attractor in the delay-coordinate embedding space.

E. Systematic data-driven SSM reduction for nonautonomous DDEs with periodic delay

For nonautonomous DDEs with periodic delay, the data-driven reduction procedure is performed in a Poincaré section. In this section, the dynamics is described by an autonomous discrete-time map, i.e., the Poincaré map. The reduction procedure is therefore analogous to Steps (1)–(7) above for autonomous DDEs, with the following modifications.

(Step 1) The assumptions of Theorem 2 are verified instead of those of Theorem 1. For C^1 periodic-delay DDEs, this theorem guarantees the existence of a time-periodic family of C^1 SSMs tangent to a time-periodic family of slow spectral subspaces.

(Step 3) The smoothness of the SSM is estimated using the eigenvalues of the discrete map approximating the Poincaré map, rather than the eigenvalues of a continuous-time SSM-reduced model.

(Step 6) The reduced dynamics in the Poincaré section is learned as a discrete-time reduced map. As in the autonomous case, this map may be approximated using either polynomial regression or radial basis function interpolation.

IV. DATA-DRIVEN SSM REDUCTION FOR DELAY DIFFERENTIAL EQUATIONS

In this section, we apply Theorem 1 to examples of increasing complexity drawn from Refs. 2, 9, 32. We begin with the Hutchinson equation,[32,47] a scalar DDE with a single discrete delay that exhibits a stable limit cycle for a suitable choice of parameters. For this system, we first derive an SSM-reduced model through the formal equation-driven calculations of Szaksz *et al.*,[28] based on Diekmann *et al.*,[27] as detailed in Appendix B 1. We then show in Appendix B 2 that this result is equivalent to the equation-based formulation of Buza and Haller,[9] which relies on the rigorous results summarized in Theorem 1. This equivalence is verified for the manifold parametrization up to second order in Fig. 25 and for the reduced dynamics up to third order in Table I.

The equation-driven SSM reduction is used here only as a benchmark to identify the limitations that the data-driven approach aims to overcome. We therefore compare the equation-driven results with a data-driven SSM reduction obtained by applying SSMLearn[13] directly to trajectories generated by the governing equations, following the procedure outlined in Sec. III. This comparison highlights the limitations of equation-based SSM reduction and motivates the use of data-driven SSM methods.

We then analyze several numerically simulated systems with multiple discrete and distributed bounded delays, including examples exhibiting chaotic dynamics. We find that the SSM-based approach captures both local and global bifurcations, consistently with the results reported in Refs. 19, 25. These examples also illustrate some limitations of existing data-driven reduction approaches for DDEs discussed in Ref. 32. In particular, we obtain SSM-reduced ODE-models with predictive power, without prior knowledge of the specific form of the DDE, including the number and magnitude of discrete and distributed delays.

Finally, we apply Theorem 2, the new theoretical result established in this paper for nonautonomous DDEs with periodic delay, to experimental control data affected by ZOH and quantization effects.

All numerical trajectories are obtained by integrating the corresponding DDE with MATLAB's **ddesd** solver, sampled uniformly at $dt = 0.01$ s. The experimental data of Sec. IV G are sampled at 0.002 s. These sampling rates avoid aliasing, keep the regressions in the delay embedding space well conditioned and remain experimentally realizable. Trajectory lengths follow the characteristic timescales of each system and are longest for the traffic model, wherein the dominant dynamics slows down near the Hopf bifurcation. Their number and length are not optimized but merely sufficient, and remain well within experimental reach, reflecting the data economy of our approach.

We note that SSMs are normally hyperbolic by construction, hence they persist smoothly under small perturbations of the dynamics or of the measurements. This property is particularly useful for experimental data, which are inherently affected by measurement noise. Persistence of SSMs under small random noise has been established rigorously for randomly forced systems in Ref. 48. This persistence has also been confirmed by the several SSM-reduced models successfully constructed from noisy experimental data (see

10 November 2026 11:30:50

© Author(s) 2026

Refs. 13, 23, 24, 37, 44 and 46 and the experiments revisited in Sec. IV G.

A. Hutchinson DDE—Equation-driven vs data-driven reduced modeling

A powerful equation-driven reduction method in the context of DDEs has been developed in Ref. 27 and extended to SSMs in Ref. 28, whose existence for DDEs has recently been rigorously established by Buza and Haller.[9] Two equivalent approaches have been proposed by Szaksz *et al.*[28] and Buza and Haller[9] to compute finite-dimensional SSMs emanating from equilibria of delay equations in an infinite dimensional phase space. The core idea is to approximate the solution of the invariance PDE via arbitrarily high-order truncated Taylor expansions. This leads to homological equations that can be solved as linear algebraic systems whose solutions yield the coefficients of both the SSM parametrization and the reduced dynamics up to the desired polynomial order. These constructions require sufficient smoothness of the DDE right-hand side and generic nonresonance conditions on the spectrum of the linearization, as detailed in Refs. 9 and 28. However, the amount of computations required by these equation-driven SSM reduction approaches is high and increases rapidly with both the dimension of the SSM and the truncation order, as the number of coefficients grows combinatorially. We apply both methods to the Hutchinson delay system, as detailed in Appendix B, reducing it to a two-dimensional (2D) SSM to motivate the need for data-driven methods in real-world applications, where the underlying equations are unknown and parameter estimation is uncertain.

The Hutchinson DDE is of the form

$$x'(t) = r\,x(t)\left(1 - \frac{x(t-\tau)}{K}\right), \tag{9}$$

as discussed in Ref. 47. After shifting the equilibrium $x_* = K$ to the origin, the state at time t is represented by the history segment

$$y_t(\vartheta) = y(t+\vartheta), \qquad \vartheta \in [-\tau, 0],$$

defined on the phase space $X := C([-\tau, 0], \mathbb{R})$, as detailed in Appendix B. Throughout, we use the parameter values $r = 1.8$, $K = 10$, and $\tau = 1$.

The dominant modes arise from an unstable complex conjugate pair of eigenvectors of the linearized system about the origin equilibrium. Applying Theorem 1, and choosing $\gamma > 0$, this ensures the existence of an SSM as smooth as the full system, thus C^∞. The spectrum in Fig. 1 is computed using the toolbox developed in Refs. 49 and 50, a root-finding algorithm for quasi-polynomials arising from the characteristic equations of DDEs.

The SSM parametrization and the reduced dynamics up to third order, computed via the procedure outlined in Ref. 28, are given by

$$W(\vartheta = 0, z, \bar{z}) = z + \bar{z} + \frac{1}{2}\left((0.0046 - 0.021i)\,z^2 + (0.0024)\,z\bar{z} + (0.0046 + 0.021i)\,\bar{z}^2\right) + \frac{1}{6}\left((-0.0019 + 0.0025i)\,z^3 + (-0.0017 + 0.0026i)\,z^2\bar{z} + (-0.0017 - 0.0026i)\,z\bar{z}^2 + (-0.0019 - 0.0025i)\right)\bar{z}^3 + \mathcal{O}(|z|^4), \tag{10}$$

$$\dot{z} = (0.097 - 1.6i)\,z + (0.072 - 0.042i)\,z^2 + (0.0055 + 0.0082i)\,z\bar{z} - (0.066 - 0.050i)\,\bar{z}^2 - (0.0039 + 0.00073i)\,z^3 - (0.0034 - 0.00054i)\,z^2\bar{z} + (0.0018 - 0.0030i)\,z\bar{z}^2 + (0.000\,80 - 0.0039i)\,\bar{z}^3 + O(|z|^4), \tag{11}$$

$$\dot{\bar{z}} = (0.097 + 1.6i)\,\bar{z} - (0.066 + 0.050i)\,z^2 + (0.0055 - 0.0082i)\,z\bar{z} + (0.072 + 0.042i)\,\bar{z}^2 + (0.000\,80 + 0.0039i)\,z^3 + (0.0018 + 0.0030i)\,z^2\bar{z} - (0.0034 + 0.00054i)\,z\bar{z}^2 - (0.0039 - 0.00073i)\,\bar{z}^3 + O(|z|^4). \tag{12}$$

In Fig. 2, we plot the objects depicted in a three-dimensional observable space. The left panel shows the spectral subspace, an SSM obtained from the second-order Taylor truncation of the manifold parametrization, and a trajectory of the full system approaching the limit cycle shown in red. This limit cycle is obtained by lifting the prediction of the SSM-reduced model. The right panel shows SSM slices for three values of ϑ in the phase space X. Each red line represents a state, i.e., a history function in X, while markers indicate intersections of the states with the SSM slices. Advecting the state generates trajectories evolving from initial conditions near the unstable fixed point at the origin toward a stable limit cycle. A marker on the SSM at $\vartheta = 0$ corresponds to the marker evaluated one second later on the SSM at $\vartheta = -1$, since for a DDE the state satisfies

$$y_{t+1}(\vartheta) = y(t+1+\vartheta) = y\big(t + (\vartheta + 1)\big) = y_t(\vartheta + 1).$$

This relation holds up to an $O(|z|^4)$ correction on the manifold, as we use a third-order Taylor expansion to approximate the spectral submanifold near the origin. Time-shift invariance is incorporated into the manifold through the interior equations in Appendix B 1.

The SSM that we are going to approximate from data using SSMLearn[13] corresponds to the slice at $\vartheta = 0$ (yellow) in Fig. 2(b),

10 November 2026 11:30:50

© Author(s) 2026

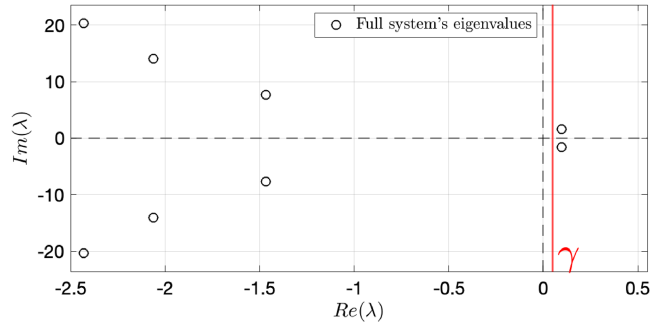


FIG. 1. Eigenvalues of the linearization of the full system (9) at the fixed point at the origin (black markers). The red vertical line indicates the value γ chosen to satisfy the assumptions of Theorem 1.

representing the invariant manifold of states, now the red markers $\vartheta = 0$ at the current time $y_t(0) = y(t)$. Slices with $\vartheta < 0$ correspond to time-shifted states and thus provide backward-shifted predictions.

Projecting the initial condition of a numerically advected full system trajectory onto the spectral subspace using the pairing (B6) enables a linear approximation of the base point of the nonlinear leaf of the stable foliation over the finite-dimensional dominant spectral submanifold. The reduced initial condition is then evolved using the SSM-reduced model and lifted via the manifold parametrization at $\vartheta = 0$ in Fig. 3 to compare full-system simulations with equation-driven SSM predictions.

Prediction errors in the limit-cycle amplitude are observed, while a frequency error induces a phase discrepancy that increases toward the end of the time series [Fig. 3(a)]. These errors can be reduced by increasing the truncation order of the reduced dynamics, at the cost of a higher-order manifold expansion.

A data-driven approach can accelerate this process while eliminating the need for explicit knowledge of the governing delay equations. More generally, when higher-dimensional SSMs are required, the computational cost of equation-driven reductions increases substantially. In an equation-driven setting, deriving higher-order reduced dynamics typically requires computing the SSM parametrization to sufficiently high order, at least one order below that of the reduced dynamics, in order to solve the

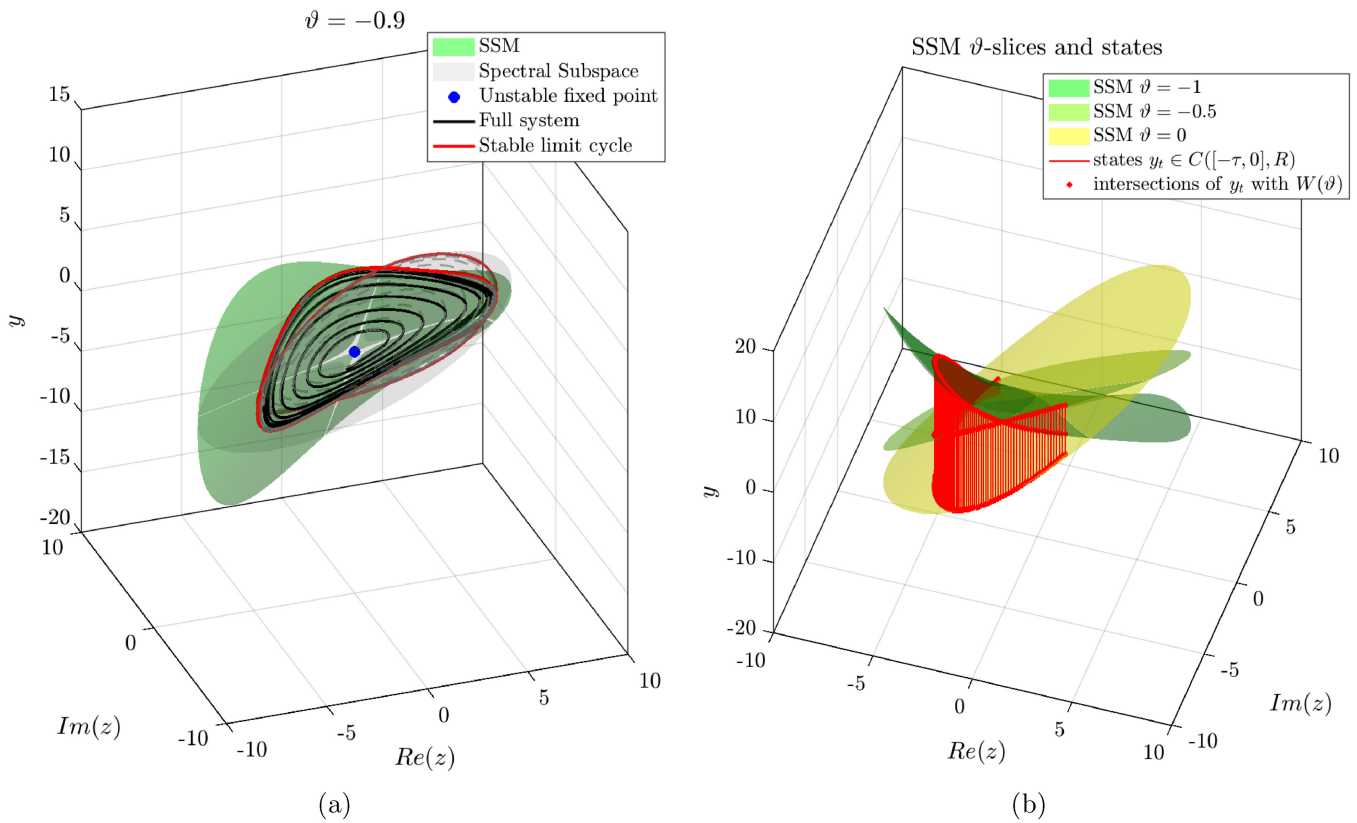


FIG. 2. (a) Comparison between a full-system trajectory (black) of system (9) and the SSM-reduced model (10)–(12) prediction (gray) obtained projecting the full trajectory's initial condition onto the spectral subspace via the pairing, lifted with the cubic equation-driven SSM parametrization at $\vartheta = -0.9$. (b) Equation-driven SSM slices for different values of ϑ (yellow: $\vartheta = 0$, medium green: $\vartheta = -0.5$, dark green: $\vartheta = -1$). Red curves denote the states in X, i.e., history functions, and red markers indicate their intersections with each slice.

10 November 2026 11:30:50

© Author(s) 2026

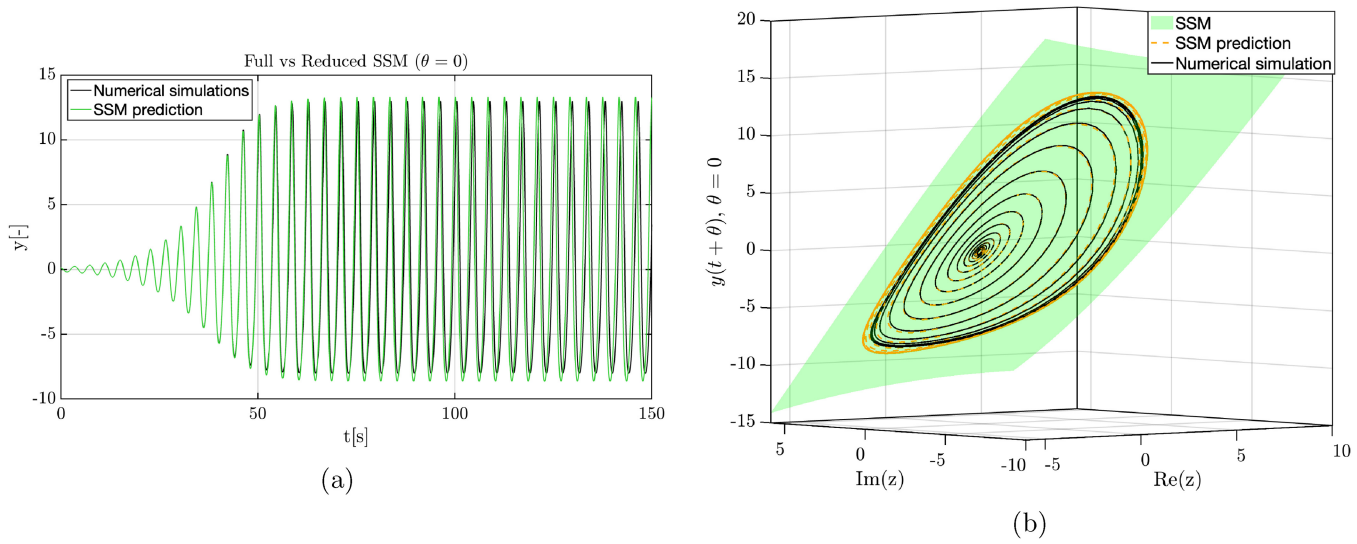


FIG. 3. (a) Comparison between a trajectory of system (9) and the corresponding equation-driven SSM-reduced model prediction. (b) Reconstructed SSM used to lift reduced dynamics into the full space.

corresponding homological equations. This requirement is avoided in the proposed data-driven approach, where the approximation orders of the SSM and of the reduced dynamics can be selected independently. Furthermore, the data-driven approach does not require the explicit verification of nonresonance conditions, since the SSM is fitted directly using polynomial regression. Most importantly, a data-driven approach is particularly advantageous for real-world systems, where the governing equations and parameter values are rarely known with high accuracy. Identifying the number and magnitude of delays from data is even more challenging, especially in the presence of distributed delays.

To address these limitations identified with equation-driven SSM reduction, we propose in this paper a data-driven SSM-reduction approach for DDEs, and start by applying it to the Hutchinson delay Eq. (9) following the procedure described in Sec. III. Numerical data are generated from the DDE (9) with the same parameter values used for the equation driven reduction.

Finite-dimensional SSMs exist under generic conditions, i.e., f in (2) being C^1.[9] In this example, inspection of a spectrogram of the initial transient indicates that the dominant eigenvalues form an unstable complex conjugate pair, ensuring the existence of a 2D C^∞ SSM W in X. Since the phase space X is infinite-dimensional, it cannot be fully observed. We therefore leverage Takens' theorem,[39] which, under generic nondegeneracy conditions on the dynamics and observables, guarantees the existence of a copy $\tilde{W}$ diffeomorphic to W, i.e., an embedding of the selected SSM W, in a delay-coordinate space of dimension k strictly greater than twice that of the SSM d.

To embed the 2D SSM capturing the dominant dynamics, we construct a delay-embedding space of dimension at least 5, using y as the observable. We approximate $\tilde{W}$, the embedding of the smooth SSM W, directly from data via polynomials. In this particular case, being the slow manifold built on all the unstable linear modes, the SSM W coincides with the unstable manifold emanating from the equilibrium and hence is unique in any smoothness class. The eigenvalues of the reduced dynamics correctly capture the two dominant eigenvalues of the full system, computed using the root-finding toolbox[49,50] (see Fig. 4).

Six training trajectories are sufficient to construct a predictive fifth-order SSM-reduced ODE model that captures the dominant dynamics of the underlying delay equation on an SSM approximated with cubic polynomials. The cubic SSM approximation significantly improves prediction accuracy as the delay-embedding lag $\Delta t = 5$

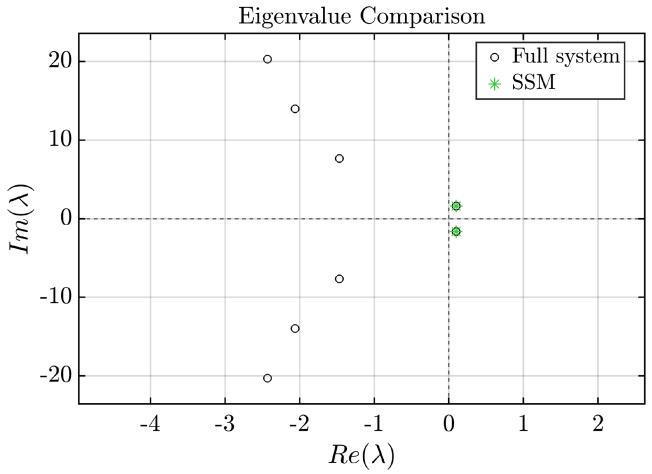


FIG. 4. Comparison between true dominant eigenvalues of the data-driven 2D SSM-reduced dynamics of system (9) (green) and those from the full system obtained via root-finding[49,50] (black).

10 November 2026 11:30:50

© Author(s) 2026

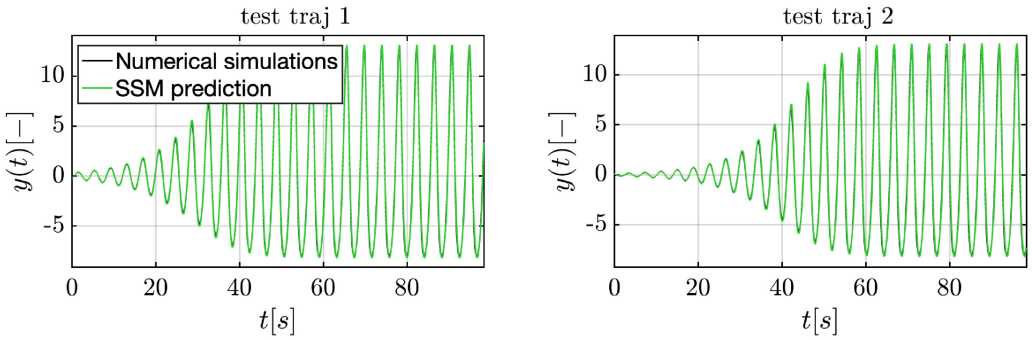


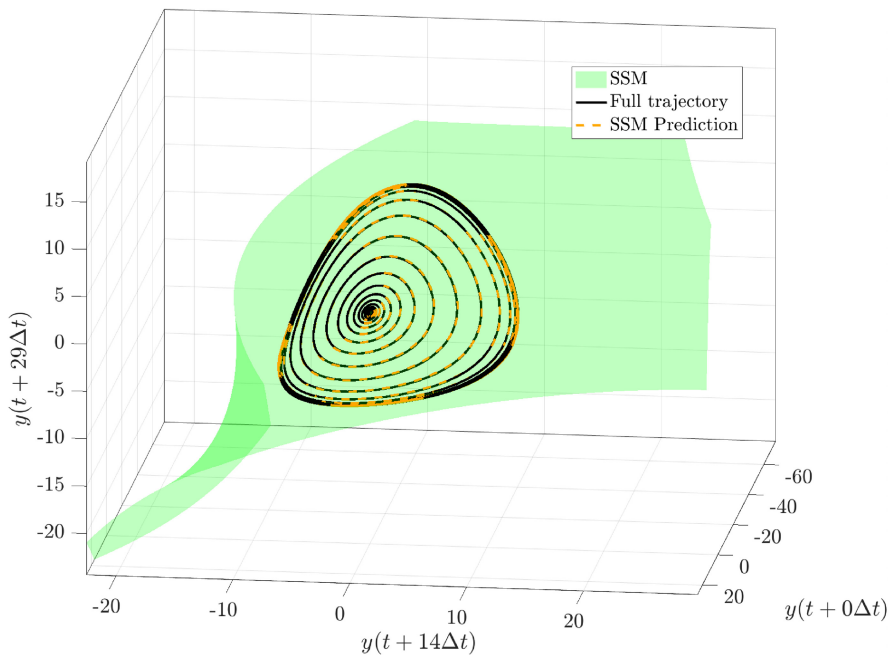
FIG. 5. Comparison between two test trajectories of the full system (9) (black) and their data-driven SSM-based predictions (green).

was selected to further reduce the NMTE. The initial conditions of the training trajectories, generated via numerical simulation of the DDE, are placed near the unstable anchor fixed point to accurately reconstruct unstable directions. These trajectories are eventually attracted to the stable limit cycle as they lie within its domain of attraction.

We evaluate the predictive power of the SSM model on previously unseen trajectories in Fig. 5 and obtain a normalized mean trajectory error (NMTE)[13] of 1.7%.

Data-driven SSM reduction seeks an optimal polynomial approximation of a diffeomorphic copy of $W(z, \bar{z}, \vartheta = 0)$ directly from data at $\vartheta = 0$, rather than recovering the Taylor expansion derived from an equation-driven formulation. Figure 6 shows a three-dimensional projection of the regressed SSM, a test trajectory with its SSM-based prediction, and the corresponding polynomial reduced dynamics.

The estimation of the spectral gap from data serves only to identify the smoothness class of W and its associated reduced dynamics ensured by Theorem 1. This requirement does not restrict the use of higher-order polynomial approximations for both the manifold and the reduced dynamics, since SSMLearn does not reconstruct the Taylor expansions produced by equation-driven methods, instead, it fits multivariate polynomials to data through regression.



$$\dot{\eta}_1 = -0.002\eta_1 - 2\eta_2 - 0.0009\eta_1^2 \\ 0.002\eta_1\eta_2 + 0.001\eta_2^2 - 2\times 10^{-5}\eta_1^2\eta_2$$

$$\dot{\eta}_2 = 1\eta_1 + 0.2\eta_2 + 0.01\eta_1^2 \\ 0.01\eta_1\eta_2 - 0.01\eta_2^2 - 0.0001\eta_1^3 \\ -0.0003\eta_1^2\eta_2 + 9\times 10^{-5}\eta_1\eta_2^2 - 5\times 10^{-5}\eta_2^3$$

FIG. 6. Left: Comparison between a full system (9) test trajectory (black) together with its prediction (orange) on the data-driven SSM (green). Right: Polynomial of the SSM-reduced dynamics, with monomials whose coefficients are smaller than 10^{-5} omitted for plot clarity.

10 November 2026 11:30:50

© Author(s) 2026

B. Chaotic attractor in a single discrete time delay system

The Mackey–Glass system,[10] a model for blood cell production, is described by the delay differential equation

$$\dot{x}(t) = \beta \frac{x(t-\tau)}{1+x(t-\tau)^{\alpha}} - \gamma x(t), \tag{13}$$

where $x(t) \in \mathbb{R}$, $\tau = 1$ is a constant discrete delay, and the parameter values are $\beta = 4.0$, $\gamma = 2.0$, and $\alpha = 9.6$ as in Ref. 32. The system admits an equilibrium at the origin. Despite being only one-dimensional, the system is known to exhibit chaotic behavior for suitable parameter choices,[10] as the delay renders the phase space infinite-dimensional. This contrasts with finite-dimensional ODEs, where chaos requires a phase space of dimension at least three.

Following the steps outlined in Sec. III, we first find the correlation dimension of the chaotic attractor to be $m \approx 2.2$ (Fig. 7).

Assuming that the chaotic attractor is contained in one of the SSMs whose existence in X is guaranteed by Theorem 1, we seek $d = 6$ dimensional SSM, following the procedure outlined in Sec. III. This choice is motivated by the oscillatory character of the dynamics and by the correlation dimension estimate $m = 2.2$. Indeed, $d = 6$ is the smallest even integer satisfying the sufficient embedding condition $d > 2m = 4.4$. This choice is further supported by a preliminary identification of the rightmost eigenvalues in the complex plane, revealing three pairs of weakly damped oscillatory modes.

Accordingly, the minimum delay embedding dimension is $k = 13$, which we further increase by 6 to improve predictive accuracy on test trajectories. Finally, we verify that the estimated correlation dimension of the attractor A is preserved under projection from the delay embedding space to the reduced space (Fig. 7), confirming that no topological information about the attractor is lost.

We identify the reduced SSM dynamics by applying polynomial regression to delay-embedded trajectories converging to the chaotic attractor A, after projecting them onto the tangent space. The graph-style parametrization of the SSM provides a one-to-one lift from the reduced coordinates to the delay-embedding space, thereby avoiding spurious self-intersections. This preserves the uniqueness of the predicted solutions, consistently with the well-posedness of smooth autonomous DDEs.[27]

The eigenvalues of the reduced dynamics, obtained from data, match those obtained via root-finding applied to the equation (Fig. 7). Additionally, by estimating eigenvalues from an 8D SSM, one can approximate the dominant spectral gap and conclude that 6D SSMs are of class C^1.

A data-driven 6D linear SSM with third-order polynomial reduced dynamics accurately reproduces key features of the attractor, including a physically relevant invariant measure and leading Lyapunov exponent. Although Theorem 1 guarantees only C^1 reduced dynamics, we employ a third-order polynomial model for two reasons: first, we seek a smooth ODE that best fits the data, without aiming to recover a Taylor expansion; second, linear ODE systems cannot exhibit chaotic dynamics.

Model performance is assessed via short-time trajectory prediction, as long-term accuracy is inherently limited by sensitivity to initial conditions. The positive leading Lyapunov exponent implies that even small projection errors grow exponentially under the flow. Exploiting the topological transitivity of A, two sufficiently long trajectories are used for training, while one is reserved for testing. Figure 8 shows trajectory divergence over the first 30 s, occurring on a timescale of order $1/\lambda_{\text{Lyap}}$. A positive Lyapunov exponent can be approximated in the delay embedding space, as detailed in Sec. III.

A physically relevant invariant measure of the chaotic attractor can be estimated via probability density functions of the reduced coordinates and is accurately reconstructed from training trajectories (Fig. 9). The leading Lyapunov exponent is estimated from data by fitting an exponential growth to the mean deviation of

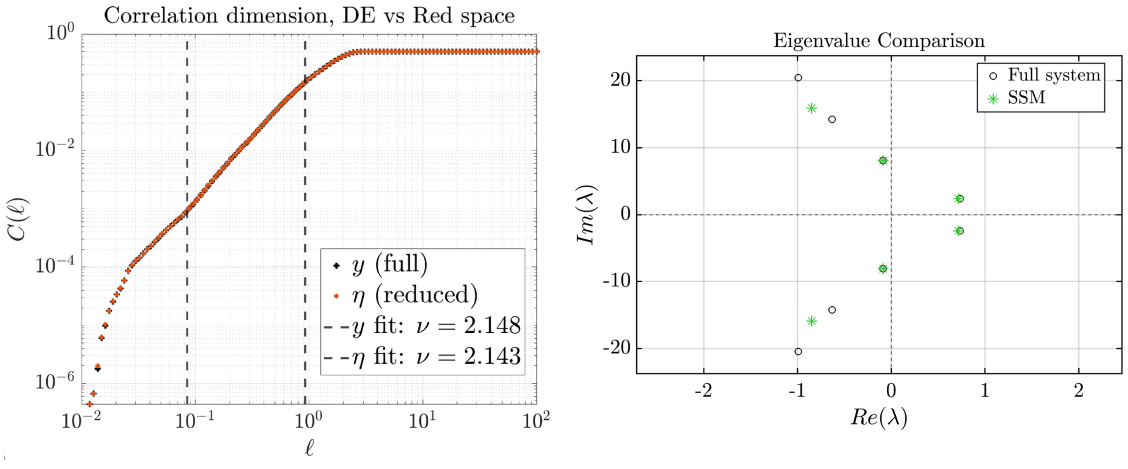


FIG. 7. Correlation dimension estimation and spectrum validation for the Mackey–Glass system (13). Left: log–log plot of the correlation sum vs radius,[40] showing a scaling region with slope $m \approx 2.2$. Right: comparison between eigenvalues of the reduced dynamics (green) and those from the full system obtained via root-finding (black).

10 November 2026 11:30:50

© Author(s) 2026

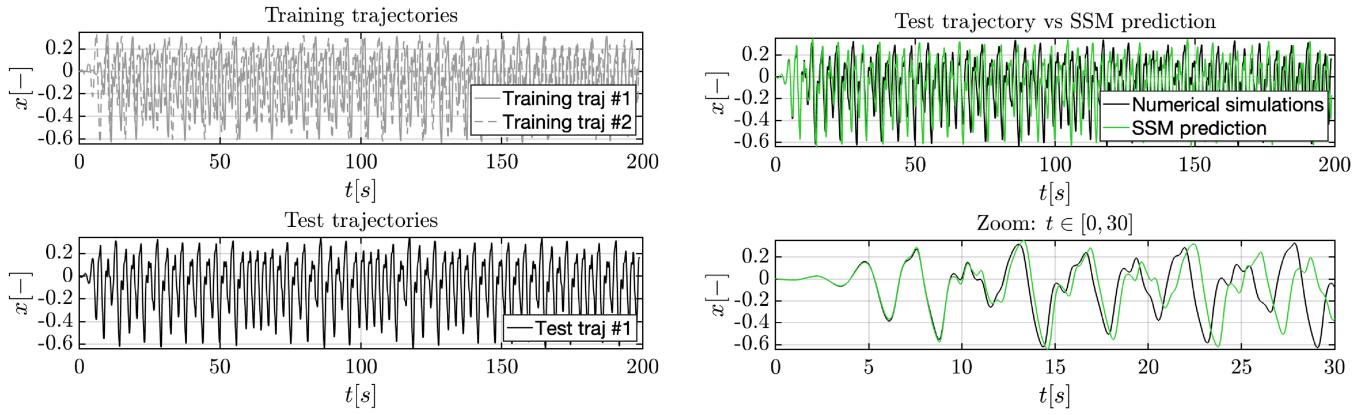


FIG. 8. Short-time prediction performance of the SSM- reduced model of system (13). Left: training and test trajectories in the observable $x(t)$ used for delay embedding. Right: comparison between full (black) and predicted (green) test trajectories, showing divergence only over a timescale consistent with the inverse leading Lyapunov exponent.

many trajectories, here we used 50, initialized within an $\epsilon = 10^{-3}$ neighborhood of a point on the attractor. The initial condition for the full model is taken as a constant history function in X. This requires access to the full DDE, but only for validation purposes. In contrast, Lyapunov exponents can be estimated directly from the SSM-based reduced dynamics, as the data-driven model allows controlled initialization near the attractor, even when only data are available.

A 3D projection in the delay embedding space shows the test trajectory together with its prediction converging to the chaotic attractor from the equilibrium (Fig. 10). The polynomial reduced dynamics for system (13) is plotted in Fig. 26 in Appendix D.

We emphasize that, even in an equation-driven setting, Taylor expansions are not guaranteed to give good approximation of global invariant structures such as chaotic attractors, as the attractor can lie outside the domain of convergence of the series. Moreover, we highlight that polynomial parametrizations suffice to obtain predictive reduced models, without the need for rational terms and subsequent knowledge of the underlying equations, as required for the Mackey–Glass equation in Ref. 32.

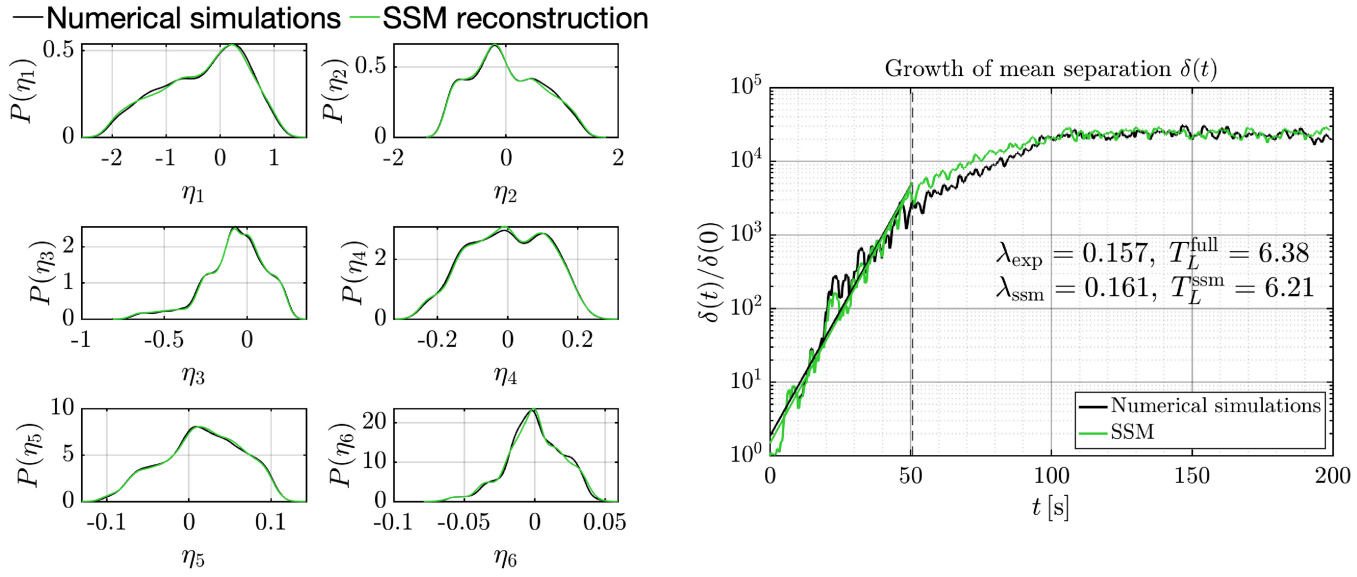


FIG. 9. Analysis of the chaotic attractor of system (13) and its SSM-reduced model. Left: probability density functions of all the reduced coordinates based on training trajectories (black) and their reconstruction (green). Right: estimation of the leading Lyapunov exponent from trajectory mean separation over time $\delta(t)$ for the full system (black) and for the SSM predictions (green).

10 November 2026 11:30:50

© Author(s) 2026

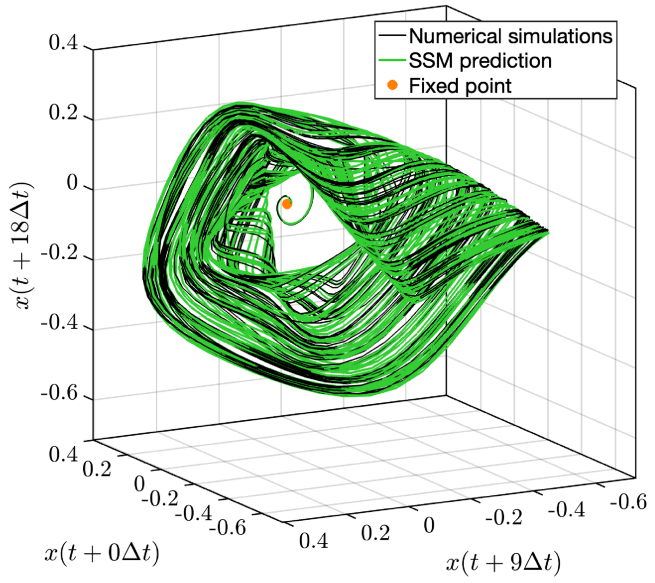


FIG. 10. 3D projection of the delay embedding space showing convergence of the test trajectory to the chaotic attractor for the full system (13) (black) and the SSM prediction (green).

C. Limit cycle in a multiple discrete time delays system

The two-neuron model with multiple discrete time delays[32] is described by

$$\begin{aligned}\dot{x}_1(t) &= -\kappa x_1(t) + \beta \tanh\left(x_1(t-\tau_s)\right) + a_{12}\tanh\left(x_2(t-\tau_2)\right),\\ \dot{x}_2(t) &= -\kappa x_2(t) + \beta \tanh\left(x_2(t-\tau_s)\right) + a_{21}\tanh\left(x_1(t-\tau_1)\right),\end{aligned} \tag{14}$$

where $x_1(t), x_2(t) \in \mathbb{R}$, with delays $\tau_s = 1.5$, $\tau_1 = 2.0$, $\tau_2 = 2.0$ and parameters $\kappa = 0.5$, $\beta = -1$, $a_{12} = 1$, $a_{21} = 2$. The system admits the trivial equilibrium $(x_1^*, x_2^*) = (0, 0)$. From the behavior of the training trajectories, we observe a 2D unstable manifold emanating from the equilibrium containing a stable limit cycle. Accordingly, we seek a 2D SSM associated with the dominant linear modes.

We follow the data-driven SSM-reduction outlined in Sec. III. A 2D C^∞ SSM exists for (14) based on Theorem 1. We learn a cubic 2D manifold with a fifth-order reduced dynamics from the scalar observable x_1 evolving on six training trajectories. The dominant eigenvalues are accurately captured by the reduced-order model, as shown in Fig. 11.

Four test trajectories of system (14), together with their predictions from the SSM-reduced model, are shown in Fig. 11, yielding a NMTE of 4.8%. A 3D projection of the delay embedding space is also reported in Fig. 12.

We observe that data-driven SSM reduction retains predictive power despite the presence of multiple discrete delays, both in number and in magnitude, which are assumed unknown throughout the reduction procedure. We next demonstrate that this performance extends to systems exhibiting chaotic attractors.

D. Chaotic attractor in a multiple discrete delays system

We now consider the system[32]

$$\begin{aligned}\dot{x}_1(t) &= -x_2(t) - x_3(t) + \alpha_1 x_1(t-\tau_1) + \alpha_2 x_1(t-\tau_2),\\ \dot{x}_2(t) &= x_1(t) + \beta_1 x_2(t),\\ \dot{x}_3(t) &= \beta_2 + x_3(t)x_1(t) - \gamma x_3(t),\end{aligned} \tag{15}$$

where $x_1(t), x_2(t), x_3(t) \in \mathbb{R}$. The delays, $\tau_1 = 1.0$ and $\tau_2 = 2.0$, and the parameter values $\alpha_1 = 0.2$, $\alpha_2 = 1.0$, $\beta_1 = 0.2$, $\beta_2 = 0.2$, $\gamma = 1.2$ are taken from Ref. 32. The system admits a nontrivial equilibrium,

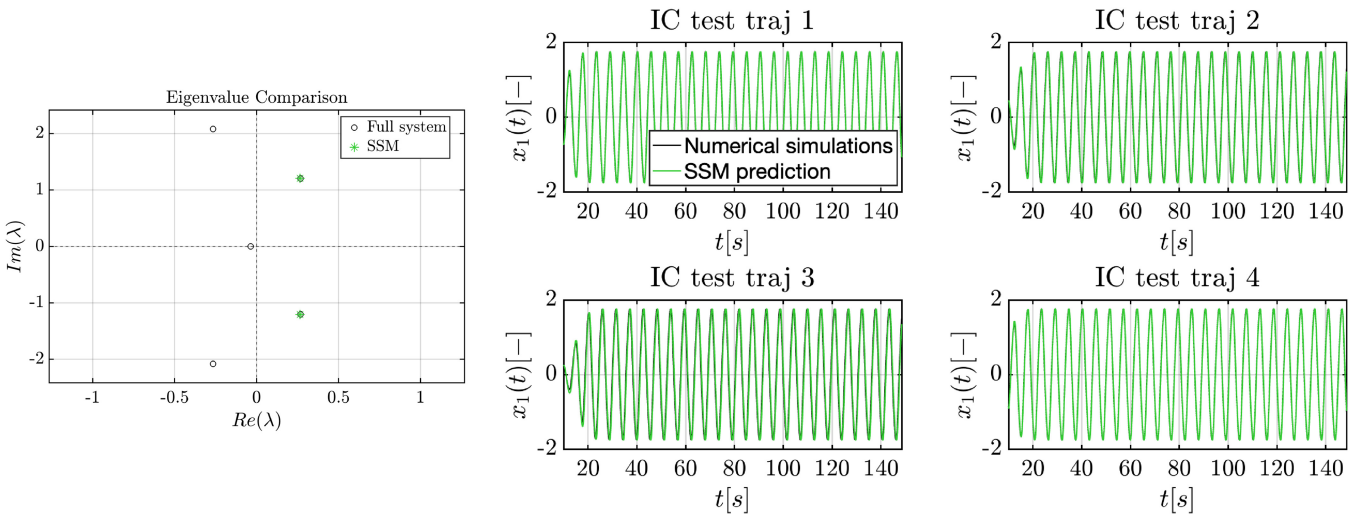
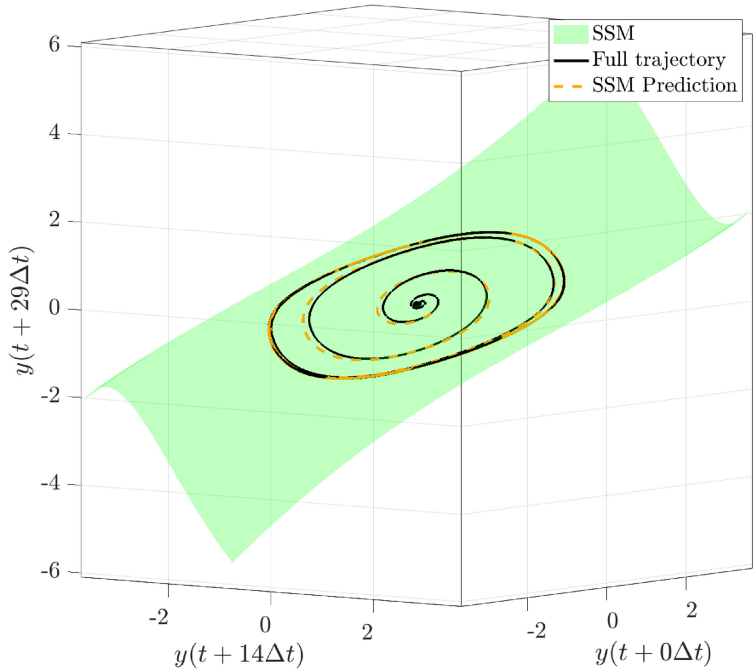


FIG. 11. Left: Comparison between eigenvalues of the data-driven reduced dynamics (green) and those obtained from the full system (14) (black) via root-finding. Right: Four test trajectories (black) and their SSM-based predictions (green).

10 November 2026 11:30:50

© Author(s) 2026



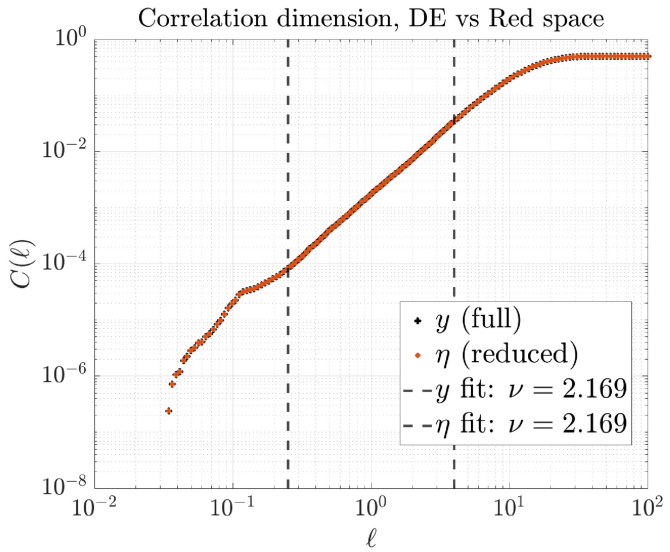
$$\begin{aligned}\dot{\eta}_1 = &-0.01\eta_1 + 2\eta_2 + 3\times10^{-5}\eta_1^2 \\ &0.0002\eta_1\eta_2 - 0.0002\eta_2^2 - 0.0001\eta_1^3 \\ &-0.002\eta_1^2\eta_2 + 0.006\eta_1\eta_2^2 - 0.001\eta_2^3 \\ &2\times10^{-5}\eta_1^4\eta_2 - 4\times10^{-5}\eta_1^3\eta_2^2 + 8\times10^{-5}\eta_1^2\eta_2^3 \\ &5\times10^{-5}\eta_1\eta_2^4 + 0.0002\eta_2^5\end{aligned}$$

$$\begin{aligned}\dot{\eta}_2 = &-0.7\eta_1 + 0.5\eta_2 - 0.0001\eta_1^2 \\ &-0.001\eta_1\eta_2 - 0.0001\eta_2^2 + 0.0008\eta_1^3 \\ &0.003\eta_1^2\eta_2 + 0.02\eta_1\eta_2^2 - 0.04\eta_2^3 \\ &1\times10^{-5}\eta_1^3\eta_2 + 1\times10^{-5}\eta_1^2\eta_2^2 + 6\times10^{-5}\eta_1\eta_2^3 \\ &-5\times10^{-5}\eta_1^4\eta_2 - 5\times10^{-5}\eta_1^3\eta_2^2 - 4\times10^{-5}\eta_1^2\eta_2^3 \\ &-0.0009\eta_1\eta_2^4 - 0.0001\eta_2^5\end{aligned}$$

FIG. 12. Data-driven SSM reduction for system (14). Left: 3D projection of the delay embedding space showing an SSM (green), with a test trajectory (black) and its prediction (orange). Right: Learned 5th order polynomial SSM-reduced dynamics. Monomials whose coefficients are smaller than 10^{-5} are omitted for plot clarity.

which we shift to the origin. This system exhibits a chaotic attractor resembling that of the Rössler system. As in the Mackey–Glass example, we estimate the correlation dimension of the attractor as $m \approx 2.17$ (Fig. 13).

Assuming again that the chaotic attractor is contained in one of the SSMs that exist in X by Theorem 1, and given the oscillatory nature of the dynamics, we seek a $d = 6$ dimensional SSM following Sec. III. Since $d > 2m$, this choice guarantees that the attractor can be



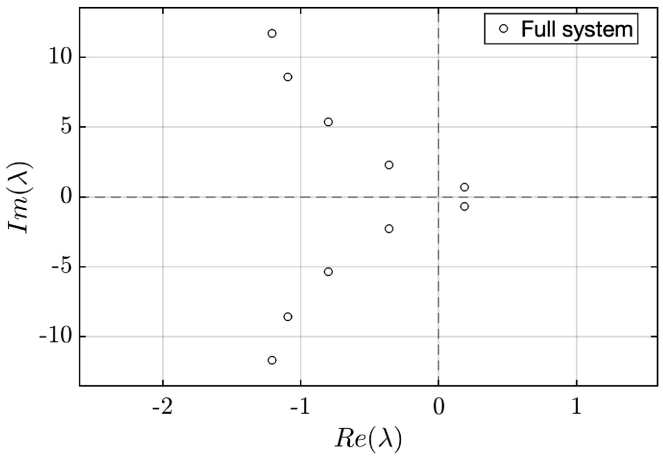


FIG. 13. Left: Correlation dimension estimation for the attractor of system (15) from data in the delay embedding space (black) and in the reduced space (orange), showing agreement in correlation dimension estimation around $m \approx 2.17$. Right: Eigenvalues of the full system (15) obtained via root-finding.[49,50]

10 November 2026 11:30:50

© Author(s) 2026

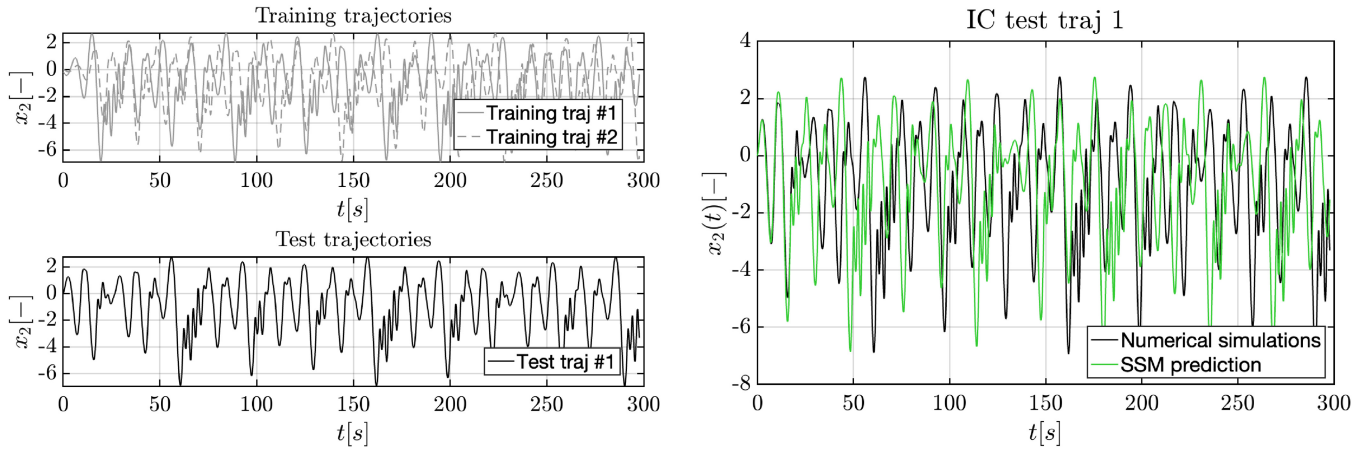


FIG. 14. Left: Training and test trajectories for the SSM-reduction of system (15) in the observable x_2. Right: Predictions (green) of a full system's test trajectory (black), with divergence at longer times due to sensitivity to initial conditions.

embedded in the reduced space within the delay-coordinate space.[41] We construct a delay embedding space of dimension $k = 23$ using the delay-coordinate map, exceeding the minimum requirement $k = 13$ to improve model accuracy.

The dominant SSM is approximated using first-order polynomials for the manifold, while the reduced dynamics are learned via radial basis functions (RBFs), as polynomial approximations are insufficiently accurate, as already noted in Refs. 15, 19 and 44. For the purpose of estimating the Lyapunov exponent from data, we regard the time series predicted by the RBF-based discrete map as a trajectory of an underlying continuous-time dynamical system, sampled at time instants separated by the discrete-map time step.

Two of the four training trajectories, together with predictions for four test trajectories, are shown in Fig. 14. As expected for chaotic dynamics, short-term predictions are accurate, while long-term prediction is limited by sensitivity to initial conditions.

A physically relevant invariant measure and the leading Lyapunov exponent are estimated from data and reported in Fig. 15.

A 3D projection of the delay embedding space (Fig. 16) illustrates the attractor and the convergence from the unstable equilibrium of a test trajectory and its prediction.

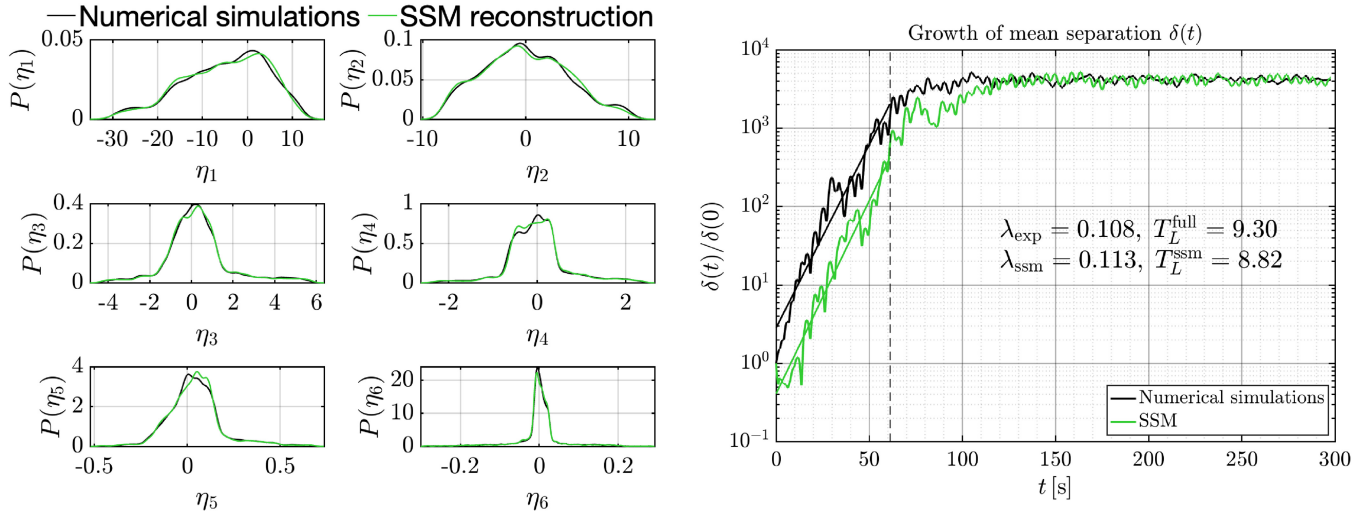


FIG. 15. Analysis of the attractor of system (15). Left: Probability density functions of the reduced coordinates, showing agreement between full system's training trajectories (black) and their SSM-based reconstruction (green). Right: Estimation of the leading Lyapunov exponent based on trajectory mean separation over time $\delta(t)$, comparing the full system (black) and the SSM-based prediction (green).

10 November 2026 11:30:50

© Author(s) 2026

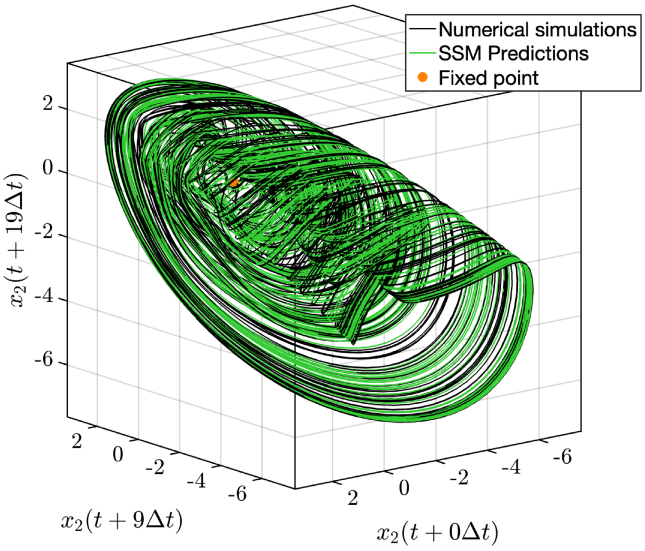


FIG. 16. 3D projection of the delay embedding space showing the chaotic attractor of system (15) and convergence of four test trajectories toward it, for both the full system (black) and the SSM-reduced model (green).

E. Parametric reduced model for delayed car-following system

We consider a time-delay traffic model describing the interaction between a human-driven vehicle (HV) and an autonomous vehicle (AV),[2] whose experimental relevance for autonomous driving control has been demonstrated in Ref. 4. The system is governed by

$$\begin{aligned}\dot{\tilde{h}}(t) &= \tilde{v}(t) - \tilde{v}_{-1}(t),\\ \dot{\tilde{v}}_{-1}(t) &= \alpha\Big(V\big(\tilde{h}(t-\tau)+h^*\big) - \big(\tilde{v}_{-1}(t-\tau)+v_{\mathrm{ref}}\big)\Big)\\ &\quad + \beta\Big(\tilde{v}(t-\tau) - \tilde{v}_{-1}(t-\tau)\Big),\\ \dot{\tilde{v}}(t) &= \hat{\beta}\Big(v_{\mathrm{ref}} - \big(\tilde{v}(t-\tau)+v_{\mathrm{ref}}\big)\Big) + \beta_{-1}\Big(\tilde{v}_{-1}(t-\tau) - \tilde{v}(t-\tau)\Big),\end{aligned} \tag{16}$$

where $\tilde{h}$ is the shifted headway between the two vehicles, and $\tilde{v}_{-1}$ and $\tilde{v}$ are the shifted velocities of the HV and AV relative to the reference speed v_{ref}. The delay τ represents the reaction time delay in the control loop of both the HV and the AV. The gains α and β describe the HV response, while $\hat{\beta}$ and β_{-1} play the analogous role in the AV controller, accounting for speed tracking and velocity-difference feedback. We use the same parameters as in Ref. 2,

$$\alpha = 0.3, \quad \beta = 0.4, \quad \hat{\beta} = 0.6, \quad \beta_{-1} = -0.4, \quad v_{\mathrm{ref}} = 26.55,$$

with

$$h_{\mathrm{stop}} = 5, \quad h_{\mathrm{go}} = 55, \quad v_{\max} = 30,$$

and h^* defined implicitly by $V(h^*) = v_{\mathrm{ref}}$.

We perform parameter-dependent SSM reduction for the traffic delay system with the equilibrium undergoing a Hopf bifurcation. Such reductions have been shown to accurately capture even global phenomena, including heteroclinic bifurcations of limit cycles,[19] as well as in fluid systems undergoing Hopf bifurcation.[25] We remark that in the DDE setting, we do not focus on uniqueness, since a smoothest nonlinear continuation of the SSM, called the primary SSM in Ref. 12, is generally not guaranteed to exist.

Before and after the supercritical Hopf bifurcation, we identify from data, at each fixed value of the delay parameter, one SSM among the infinitely many SSMs. We then interpolate the tangent space, the polynomial parametrization of the manifold, and the polynomial parametrization of the reduced dynamics across the sampled parameter values. This yields a parametric SSM model in the delay-embedding space augmented with the bifurcation parameter, following.[19] Each autonomous SSM reduction at a fixed value of the delay parameter is carried out according to the procedure detailed in Sec. III. The manifold and the dynamics are not necessarily smooth with respect to the delay parameter; nevertheless, their dependence on the delay can be approximated via smooth spline interpolation, rather than simple linear interpolation, when it provides better accuracy.

Resonances are less disruptive in the data-driven setting, as we do not compute Taylor expansions of the solutions to the invariance PDE, but approximate them directly from data. Nevertheless, they still provide useful guidance: if a good approximation of the manifold cannot be learned, we will restrict the parameter range or reduce the polynomial order, as lower-order approximations cut out resonance-induced differences, making different SSMs less distinguishable, and being that the resonances at lower order occur further away from the critical value of the parameter, as noted in Ref. 25.

The parametric SSM model is trained at four parameter values, $\tau = \{1.030\,\mathrm{s}, 1.050\,\mathrm{s}, 1.070\,\mathrm{s}, 1.090\,\mathrm{s}\}$, by constructing individual autonomous SSM-reduced models. Each model is trained on eight trajectories using only the segments lying approximately on the manifold and evaluated on two unseen trajectories. The results (see Fig. 17) demonstrate accurate reconstruction across unseen parameter values, with an average NMTE below 1%, even as a supercritical Hopf bifurcation occurs at the origin.

We employ a 2D SSM with a third-order polynomial parametrization of the manifold and fifth-order polynomial reduced dynamics. The delay-embedding space has dimension 7, using all three state variables as observables. We remark that, because interpolation is used to construct the parametric SSM model, all individual SSM reductions must share the same SSM dimension, delay-embedding dimension, SSM approximation order, and reduced-dynamics approximation order.

F. Parametric SSM-reduced model for the analysis of multiple local bifurcations of limit cycles in systems with distributed delay

We now consider the Cushing delay equation from Ref. 9, 51, which is a distributed-delay equation with bounded delay. The parametric SSM-reduced ODE model explains the mechanism underlying qualitative changes in the system dynamics that lead to unusual behavior of observables as the time delay increases.

10 November 2026 11:30:50

© Author(s) 2026

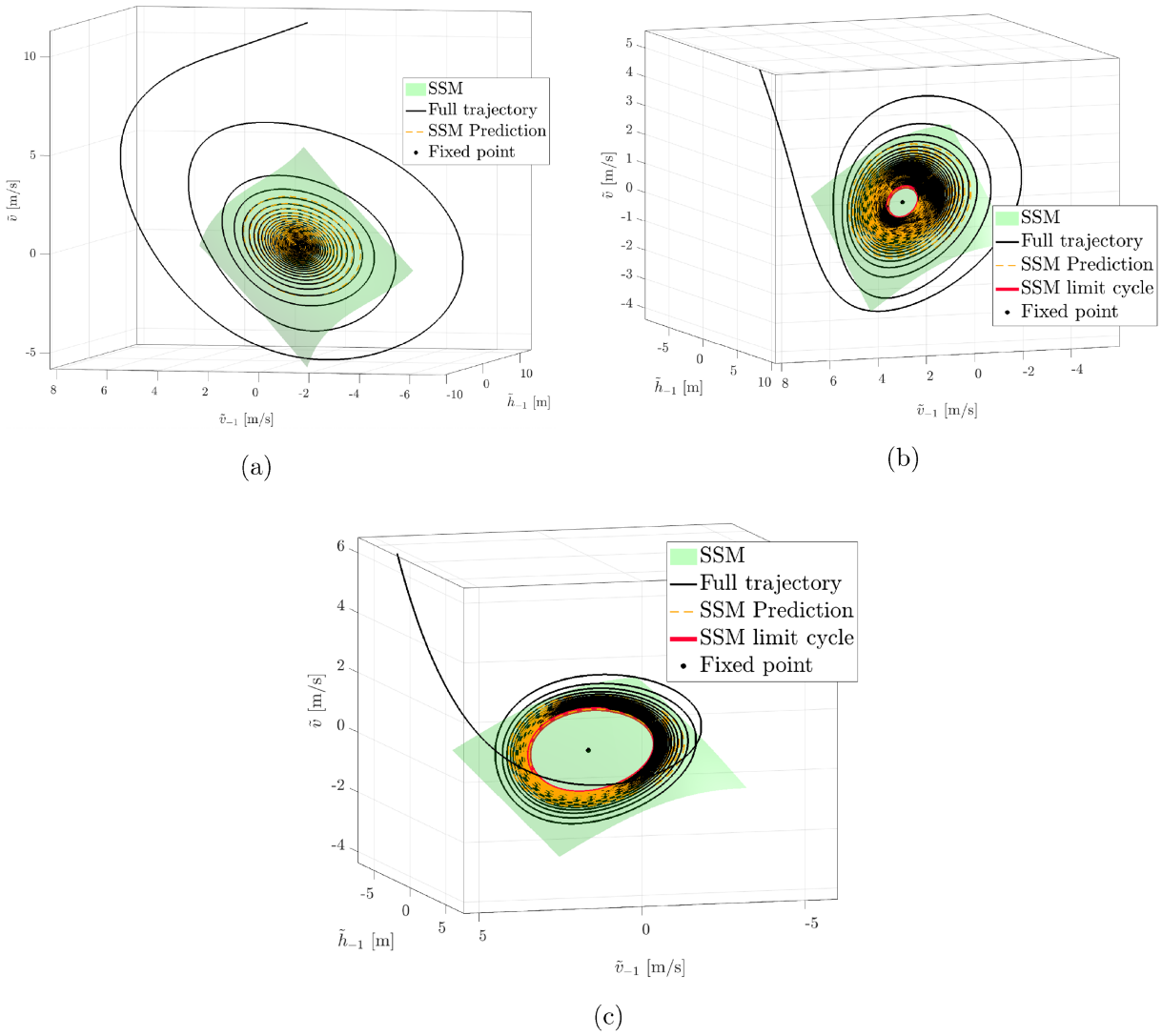


FIG. 17. For system (16), 3D projections of the delay embedding space showing the learned SSM (semi-transparent green), the full-system trajectory approaching the SSM (black), and the SSM prediction (orange dashed) for three unseen values of the delay parameter: (a) $\tau = 1.040$ s, (b) $\tau = 1.065$ s, and (c) $\tau = 1.080$ s. The plots illustrate the onset of the Hopf bifurcation, known to occur in the full system at approximately $\tau = 1.064$ s, as identified by tracking the slowest pair of eigenvalues using the root-finding algorithm.[49,50] They also show the corresponding increase in limit cycle amplitude, while demonstrating that the SSM-based reduced model retains predictive accuracy. (a) $\tau = 1.040$ s, (b) $\tau = 1.065$ s, (c) $\tau = 1.080$ s.

The system in question is governed by

$$\dot{x}(t) = b \int_0^\tau x(t-\vartheta)\, d\vartheta + a\big(x(t) - \sin(x(t))\big), \tag{17}$$

where $x(t) \in \mathbb{R}$, $\tau > 0$ is the delay, and $a = 1$, $b = -3$ are system parameters.

An equation-driven reduction for $\tau = 1$ was obtained in Ref. 9, whose general formula can be applied directly. Alternatively, the system can be reformulated as a discrete-delay equation by introducing the auxiliary variable if one wishes to carry out the equation-driven reduction following Szaksz *et al.*[28],

$$z(t) = \int_{t-\tau}^{t} x(s)\, ds,$$

which transforms (17) into the equivalent delay system

$$\begin{aligned} \dot{x}(t) &= b\, z(t) + a\big(x(t) - \sin(x(t))\big), \\ \dot{z}(t) &= x(t) - x(t-\tau). \end{aligned} \tag{18}$$

© Author(s) 2026

10 November 2026 11:30:50

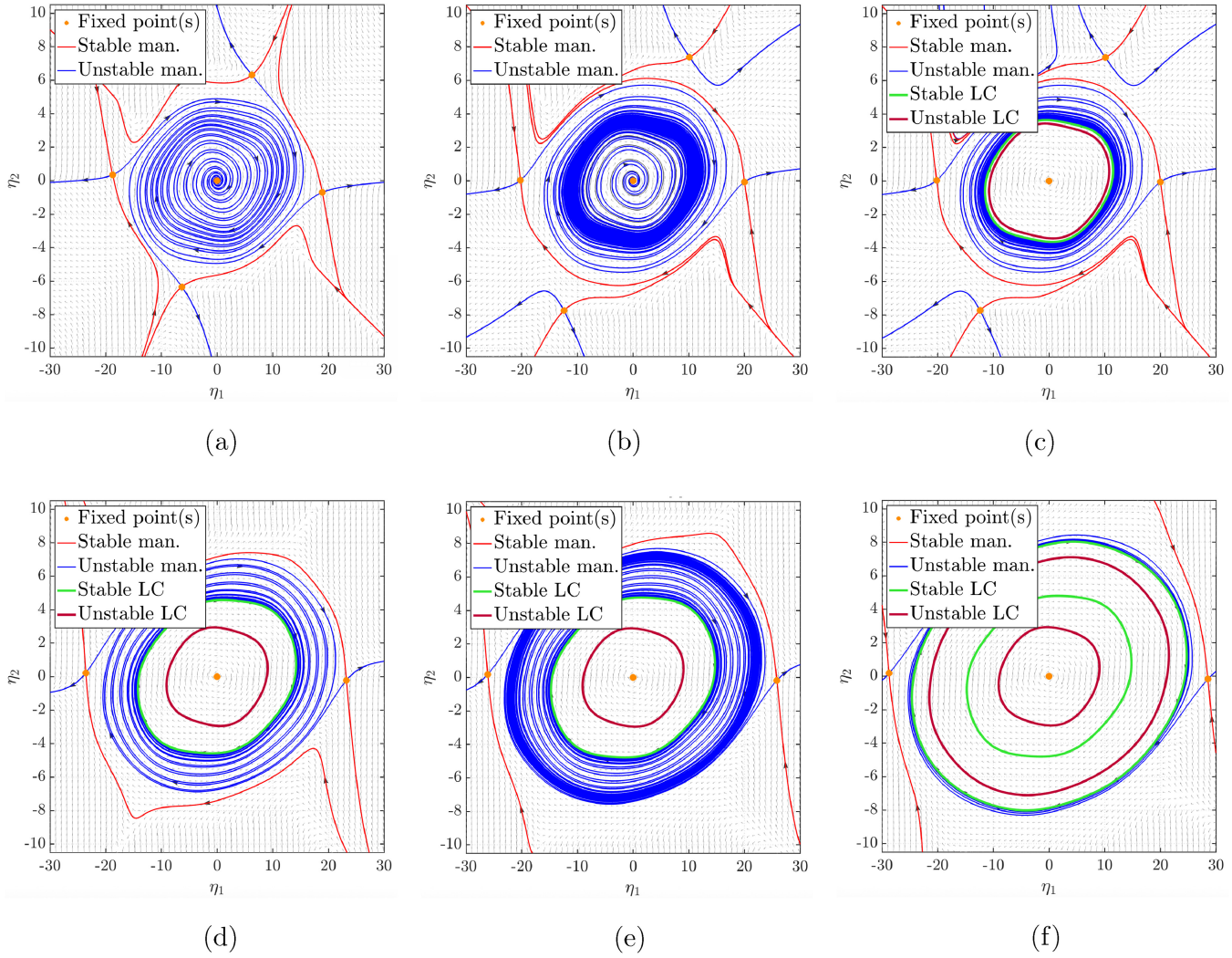


FIG. 18. Predicted and verified portraits of the parametric SSM-reduced dynamics of system (17) at six previously unseen values of the delay τ, shown for increasing τ. The reduced dynamics captures a sequence of two saddle-node bifurcations of limit cycles, which explains the qualitative change of the dynamics underlying the unusual behavior of the observables. (a) $\tau = 0.98$ s, (b) $\tau = 1.0074$ s, (c) $\tau = 1.0078$ s, (d) $\tau = 1.025$ s, (e) $\tau = 1.0294$ s, (f) $\tau = 1.0299$ s.

Thus, the scalar distributed-delay equation is recast as a 2D equation with a single discrete delay. The equilibrium of interest is the origin, $(x, z) = (0, 0)$.

The equation is symmetric under the transformation $x \mapsto -x$; therefore, this symmetry is expected to be preserved in the phase portrait of the reduced dynamics. In particular, for instance, every fixed point (η_1^*, η_2^*) should have a symmetric counterpart $(-\eta_1^*, -\eta_2^*)$. However, because the reduced dynamics are only approximated from data, they are not necessarily exactly odd. This slight symmetry breaking may further stem from the fact that the approximated manifold does not exactly satisfy odd symmetry.

We construct a parametric model following the approach in Ref. 19. In the present setting, however, the construction of the SSMs can be justified directly by Theorem 1, whose conditions are verified. By contrast, the models in Ref. 19 were obtained by analogy with the finite-dimensional SSM theory for ODEs. Linear interpolation suffices to obtain an SSM-based model across multiple limit-cycle saddle-node bifurcations near the origin (see Fig. 18). We use eight parameter values, $\tau = \{0.95\,\text{s}, 0.97\,\text{s}, 0.99\,\text{s}, 1\,\text{s}, 1.01\,\text{s}, 1.02\,\text{s}, 1.03\,\text{s}, 1.035\,\text{s}\}$, to construct individual autonomous 2D SSM models following the procedure detailed in Sec. III. Cubic-order polynomials are employed for the manifold approximation and 13th-order polynomials for the reduced dynamics, required to ensure accuracy of the SSM-based model at every training parameter point. Each model is trained on 26 trajectories, with 4 reserved for testing. This sampling is more than sufficient to achieve high accuracy.

10 November 2026 11:30:50

© Author(s) 2026

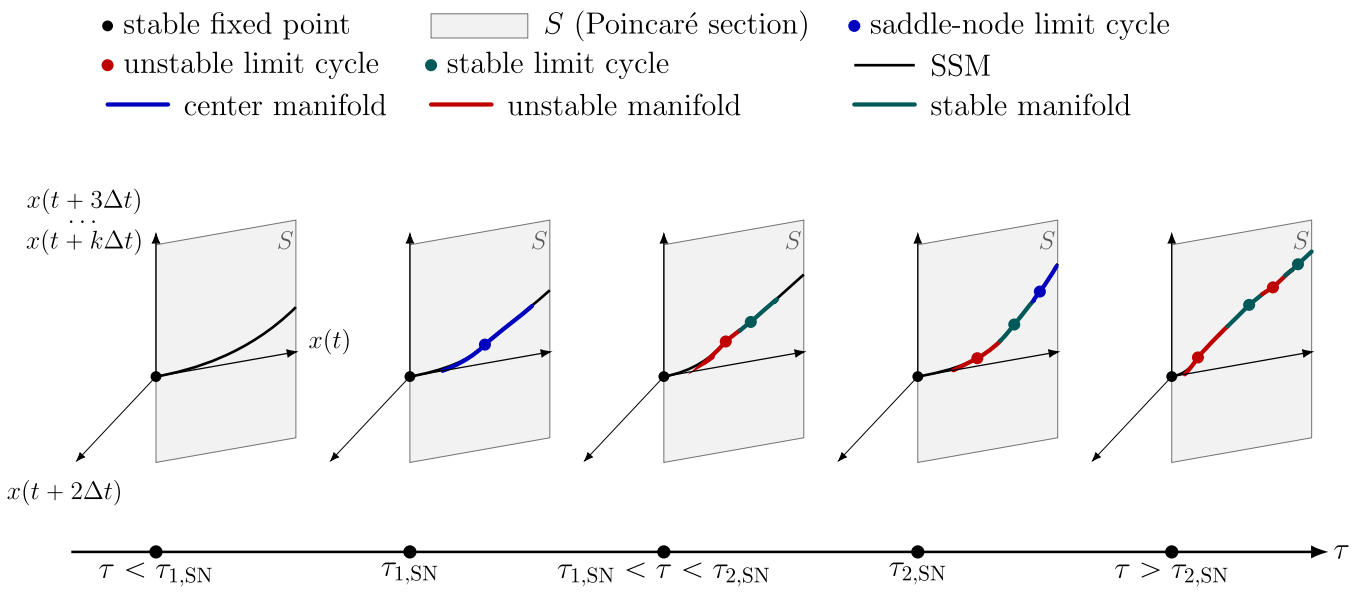


FIG. 19. Illustration of the codimension one Poincaré section viewed in the delay embedding space extended with the bifurcation delay parameter. Limit cycles can be found as fixed points of the associated 1D Poincaré map of the 2D SSM-reduced dynamics via, e.g., Newton–Raphson iteration. It is shown how one SSM-reduced ODE model is able to contain manifolds of the limit cycles along the parameter thus giving accurate reduced model of the full, infinite dimensional DDE across multiple saddle node bifurcations of periodic orbits. One should note that the manifolds (unstable/stable/center) of limit cycles are well approximated by the SSM at least locally in the phase space, but far from the fixed point from which they emanate they might in general deviate off the SSM due to higher order terms which are not captured by the fixed utilized order of the SSM.

Limit cycles are identified as fixed points of the Poincaré map, obtained by tracking oriented intersections of trajectories of the SSM-reduced ODE with a chosen codimension-one section in the reduced space, a straight line within the 2D tangent space. This yields a further reduction to a one-dimensional (1D) discrete map of the original infinite-dimensional DDE. However, this reduction loses information on coexisting isolated fixed points, restricting the validity of the reduced dynamics to regions where only the origin equilibrium and limit cycles exist.

A bifurcation diagram can then be constructed from the Poincaré map by plotting the positions of limit cycles in the section against the delay parameter, revealing two subsequent saddle-node bifurcations of periodic orbits.

The parametric SSM, corresponding to the 2D slow stable subspace at the origin extended by the parameter direction, approximates well an extended center manifold (i.e., a center manifold in the delay embedding space extended with the delay parameter direction) associated with a saddle-node limit cycle, for the case of both bifurcations, arising near $\tau \approx 1.0075$ and $\tau \approx 1.0295$. Near each bifurcation in the parameter direction, the emerging stable and unstable limit cycles lie on such an extended center manifold emanating from the saddle-node limit cycle, which is locally captured by the SSM. Consequently, a single parametric SSM is able to model the birth and evolution of these newborn limit cycles across the parameter sweep.

We now extend our analysis to a broader range of parameter values, rather than restricting attention to local behavior near critical parameter values. Specifically, by considering the 1D Poincaré section in the reduced space and the associated Poincaré map, lifted in the delay embedding space in the illustration we provide in Fig. 19, we can more clearly observe that a 2D SSM (associated with the stable eigenvalue and the zero eigenvalue corresponding to the parameter direction) emanating from the origin provides a good approximation, at least locally in phase space extended with the parameter and up to a sufficiently high polynomial order of a Taylor expansion, of the 2D spectral submanifold associated with the saddle-node bifurcating eigenvalue and the center eigenvalue (corresponding to the parameter direction) emanating from the inner saddle-node limit cycle around $\tau_{2,SN}$ and of that emanating from the outer saddle-node limit cycle $\tau_{2,SN}$ (fixed points of the Poincaré map). As such, the SSM emanating from the origin captures, over a global range of the parameter, the evolution of both the inner pair of stable and unstable limit cycles and the outer pair of stable and unstable limit cycles, simultaneously.

We emphasize that our SSM is only an approximation, as the saddle-node limit cycles, together with the newborn unstable and stable limit cycles, lie on a particular extended center manifold of a family of extended center manifolds. Moreover, these invariant objects also lie on a specific SSM chosen from a family of SSMs, which are not unique in the present setting of delay differential equations.

10 November 2026 11:30:50

© Author(s) 2026

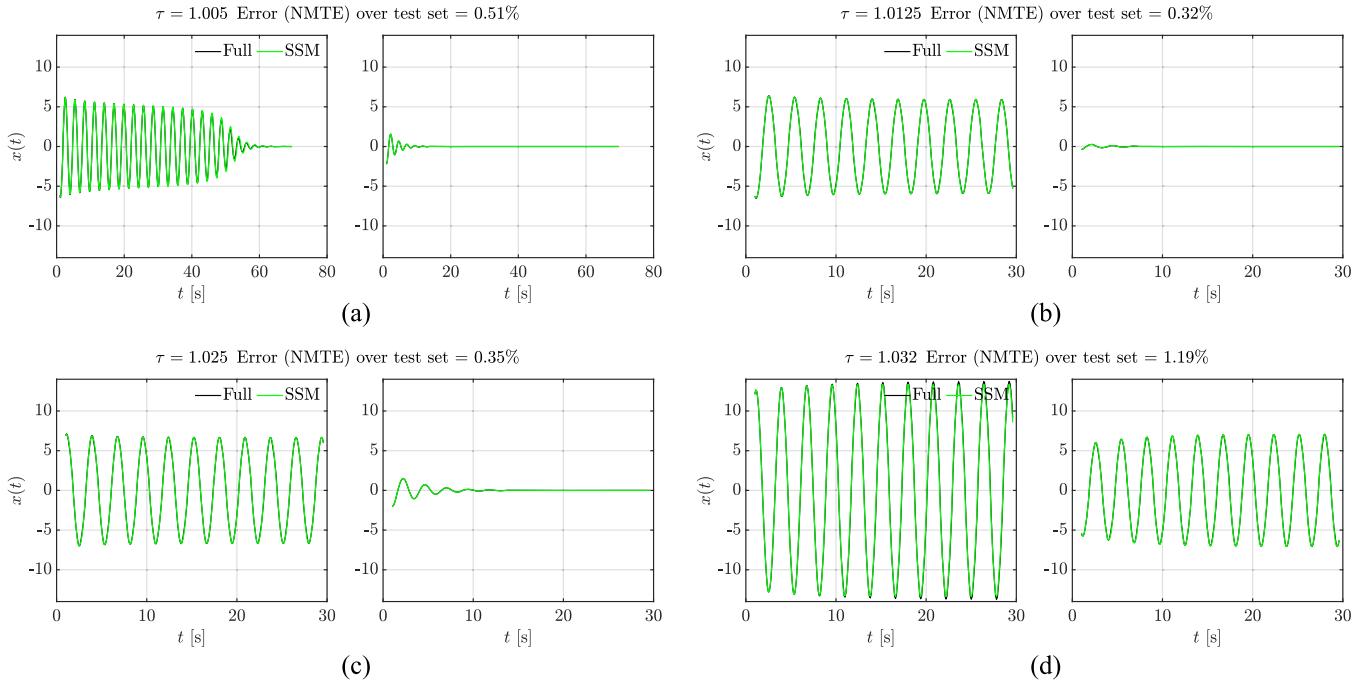


FIG. 20. Validation of the parametric SSM model for system (17) at unseen delay values. The model captures the onset of a saddle-node limit cycle (a), stable limit cycles [(b) and (c)], and the coexistence of two limit cycles (d). The NMTE is reported in each panel. (a) $\tau = 1.005$ s, (b) $\tau = 1.0125$ s, (c) $\tau = 1.025$ s, (d) $\tau = 1.032$ s.

If the order of polynomials used to approximate the SSM from data were increased, the discrepancy between the computed SSM and the actual particular SSM on which the saddle-node limit cycles, unstable limit cycles, and stable limit cycles lie would also increase, since higher-order polynomials would select a more specific member of the non-unique family of SSMs. Guided by Taylor series considerations, for lower polynomial orders, this discrepancy is less pronounced and we can conflate all the infinitely many SSMs with the one we have computed. This approximation provides a good representation of the SSM that actually contains the saddle-node limit cycles, unstable limit cycles, and stable limit cycles, as well as of the particular extended center manifold of the saddle-node limit cycle on which the unstable limit cycle and stable limit cycle are going to be born. Finally, we stress that our approach provides a polynomial approximation inferred from data, rather than computing the Taylor series.

More generally, away from the bifurcation values, each stable (respectively unstable) limit cycle possesses a unique 1D stable (respectively unstable) manifold in the Poincaré section for a fixed parameter value. Each of these manifolds is captured, i.e., well approximated at least locally in phase space and up to a sufficiently high polynomial order, by the 1D computed SSM emanating from the origin.

An alternative approach to constructing the bifurcation diagram is to compute the extended normal-form transformation and introduce polar coordinates. This yields a 2D ODE in $(\dot{\rho}, \dot{\vartheta})$, where the $\dot{\rho}$ equation decouples from $\dot{\vartheta}$. A parametric study of the $\dot{\rho}$ equation (e.g., via interpolation) then provides a bifurcation diagram of ρ vs τ. However, this approach is difficult to implement from data, as the extended normal-form transformation is highly sensitive and does not interpolate reliably across parameter values. Instead, one could proceed in an equation-driven manner, which is computationally demanding, especially given the high polynomial order (13th order in this case) required to obtain an accurate parametric SSM-reduced model capturing the two local bifurcations of four coexisting limit cycles.

This behavior is inherently nonlinear and cannot be captured by linear models. For instance, any principal Koopman eigenfunction whose domain contains the fixed point and the inner unstable limit cycle must identically vanish along both, thereby trivializing the dynamics.

Predictions of the parametric SSM model remain accurate for unseen delay values, as shown in Fig. 20, with the NMTE remaining below 1.2%. Panel (a) shows the onset of a saddle-node limit cycle, indicated by the gradual decay of oscillation amplitude toward a stable fixed point. Panels (b) and (c) show stable limit cycles after the first bifurcation, while panel (d) exhibits the coexistence of two limit cycles with different amplitudes after the second bifurcation.

10 November 2026 11:30:50

© Author(s) 2026

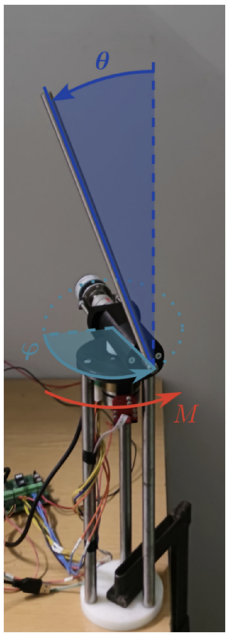


FIG. 21. Experimental rig used to control the Furuta pendulum.

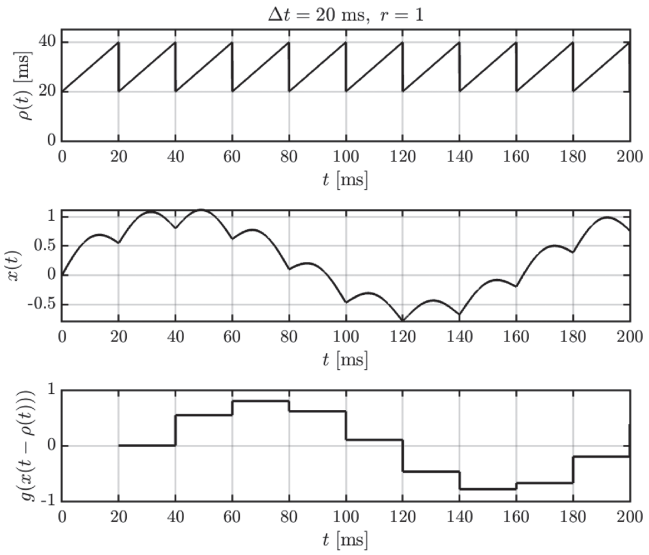
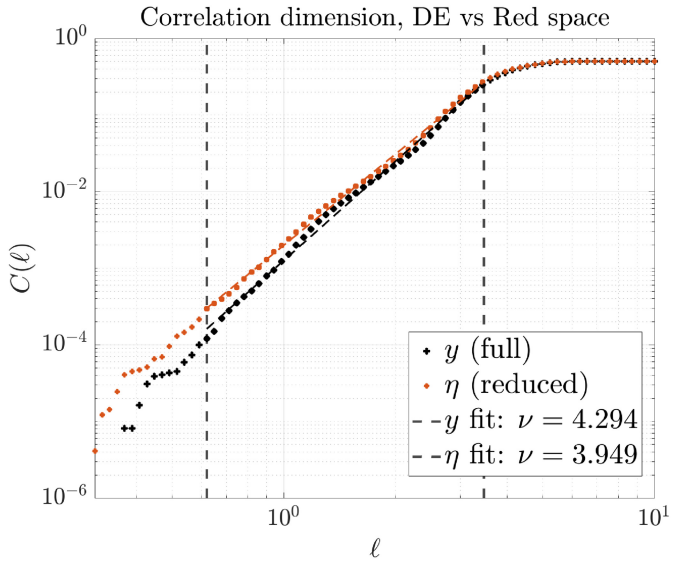


FIG. 22. Illustration of the periodic-delay mechanism induced by the ZOH for a scalar DDE of the form (20), with $f \in C^1$, sampling time $\Delta t = 20$ ms, and feedback delay $r = 1$. Top: periodic delay $\rho(t)$. Middle: state trajectory $x(t)$. Bottom: delayed control action $g(x(t-\rho(t)))$, shown as a piecewise-constant signal due to the sample-and-hold action of the digital controller.

G. SSM-reduced modeling from periodically delayed experimental data

Here, we verify the existence of an SSM in the data-driven modeling of a PD-controlled mechanical system with delayed feedback and quantization using experimental data collected from the setup shown in Fig. 21. The experiments were conducted at the Department of Applied Mechanics, Budapest University of Technology and Economics (BME), under the supervision of Professor Gábor Stépán. These data were previously made publicly available



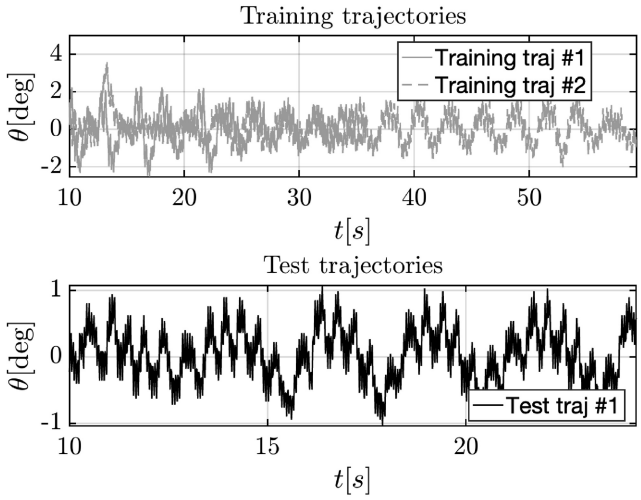


FIG. 23. Left: correlation dimension of the chaotic attractor, yielding a value of approximately 4.3. Right: training and test trajectories used for identification and validation of the first-order, 10-dimensional SSM with RBF-approximated SSM-reduced dynamics.

10 November 2026 11:30:50

© Author(s) 2026

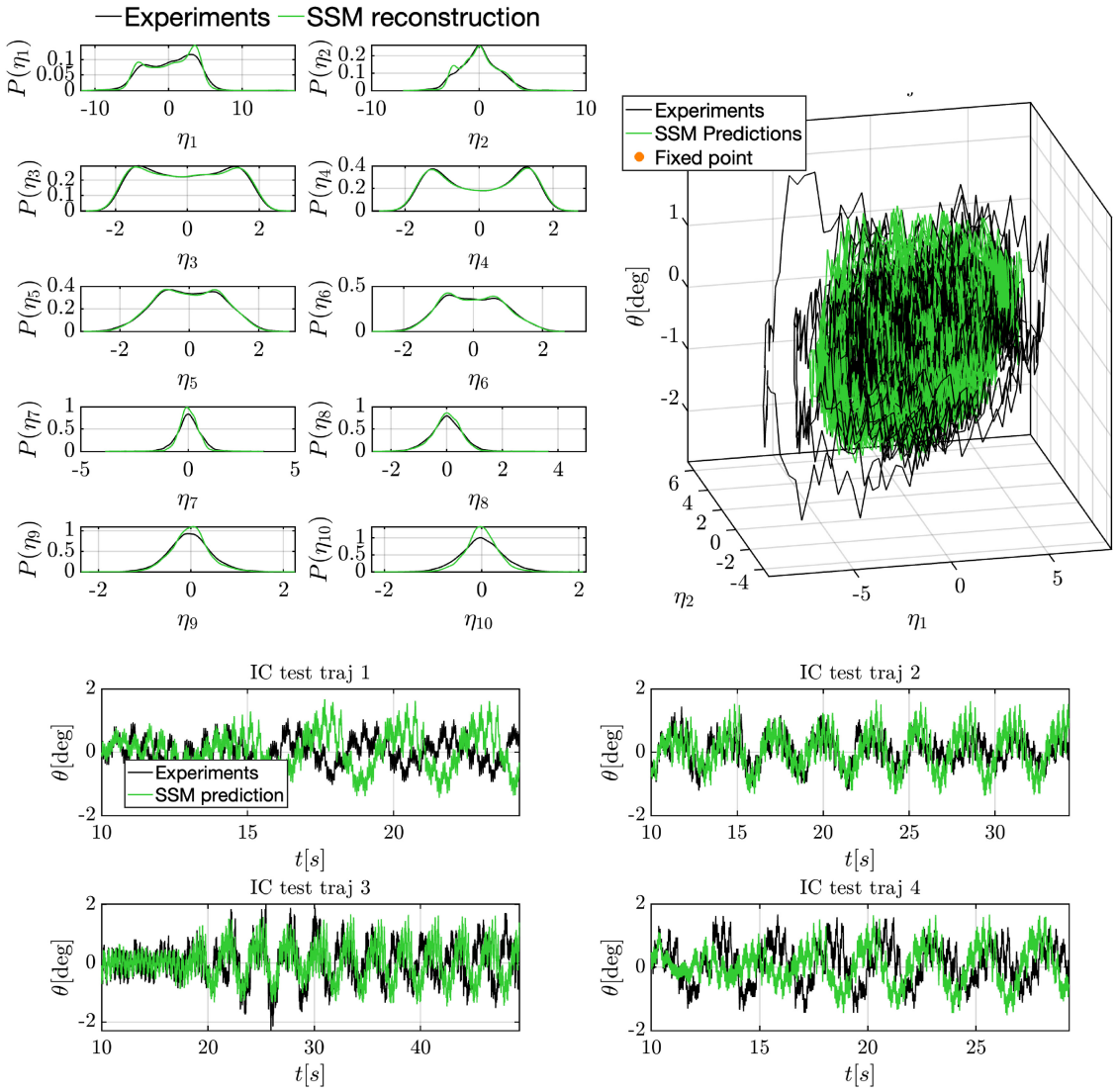


FIG. 24. SSM-based model predictions for the Furuta pendulum experiments on previously unseen trajectory data. Top left: probability density functions of the reduced coordinates of training trajectories from experimental data and their reconstruction from the RBF-based SSM model. Top right: Two full system's test trajectories (in black) evolving on the chaotic attractor together with their reduced model predictions (in green). Bottom: short-time predictions for two test trajectories, illustrating attraction toward the chaotic invariant set.

in Ref. 19. In that study, SSMs are employed to model global bifurcations and chaotic dynamics.

In the experimental setting considered there, a periodic delay $\rho(t)$ arises from the ZOH logic of the digital controller implementation,

$$\rho(t) = t - \Delta t \left\lfloor \tfrac{t}{\Delta t} \right\rfloor + r\,\Delta t, \qquad r \in \mathbb{N}, \tag{19}$$

where $\lfloor \cdot \rfloor$ denotes the integer part. The resulting controller simultaneously accounts for the constant feedback (discrete) delay $r\,\Delta t$ (with $r = 1$ for the system studied here) and the additional delay induced by the ZOH mechanism,

$$t - \Delta t \left\lfloor \tfrac{t}{\Delta t} \right\rfloor,$$

which is periodic in time. The closed-loop system can therefore be written as

$$\dot{x}(t) = \underbrace{f(x(t))}_{\text{uncontrolled system}} + \underbrace{g(x(t-\rho(t)))}_{\text{linear controller}}. \tag{20}$$

The control action is updated at the beginning of each sampling interval and then held constant over the interval of length Δt, as

10 November 2026 11:30:50

© Author(s) 2026

shown in Fig. 22. This mechanism produces a periodic sawtooth-like delay, as discussed in Ref. 8, where an expression for its average value is also derived.

In light of the new theoretical results detailed in Theorem 2, which extend the Theorem 1[9] to DDEs with periodic delay, we carry out data-driven SSM-reduction following Sec. III.

Due to the ZOH logic, the control action g is in theory non-smooth. In reality, however, the control action is smooth with high gradients instead of nonsmooth, as a jump at the beginning of each and every sampling interval would require infinite power to occur, which is not possible. The system is thus C^1, allowing us to apply Theorem 2 to digital controllers (20).

We first reduce the system to a Poincaré section associated with sampling at intervals of length Δt. This yields an autonomous DDE whose Poincaré map is C^1 and, by Theorem 2, admits infinitely many d-dimensional SSMs in the Poincaré section emanating from the equilibrium at 0, all tangent to a selected spectral subspace and with regularity C^1. Infinitely many periodic SSMs and the associated periodic spectral subspace exist with regularity C^1 as well in the extended phase space $X \times S^1$. These periodic objects can be reconstructed from data by periodically interpolating the SSMs and spectral subspaces obtained in different Poincaré sections.

By subsampling the experimental time series of the observable ϑ at intervals Δt, we obtain observations corresponding to intersections of the continuous-time flow with a codimension-one Poincaré section S in the delay-embedding space extended with time $\phi \doteq t \bmod \Delta t \in S^1$. The SSMLearn algorithm is then used, following Sec. III, to fit a polynomial approximation of the SSM in S, whose existence is guaranteed by Theorem 2, emanating from the unstable upright equilibrium of the pendulum in Ref. 19, corresponding to the angular position of the vertical arm $\theta = 0$.

The reduced dynamics on the manifold are subsequently learned by projecting the data onto the tangent space and identifying a discrete-time map that approximates the Poincaré map. In this work, we employ RBFs, as the quantization inherent in the digital controller induces microchaos in the feedback-delayed PD controlled system.[5,52] Finally, the SSM in the full extended delay-embedding space can be reconstructed by gluing the SSMs computed on each Poincaré section, parametrized by the phase variable $\phi \in S^1$.

The chaotic attractor has an estimated fractal dimension of approximately 4.3. Assuming that the chaotic attractor is contained in one of the SSMs in X, we seek an SSM of sufficiently high dimension to ensure a correct embedding of the attractor in the reduced space within the delay-coordinate space.[41] In this sense, a 10-dimensional embedding is adopted as a sufficient, not necessary choice. We therefore fit a first-order, 10-dimensional SSM, with the reduced dynamics approximated by radial basis functions (RBFs). The model is trained on four trajectories and tested on four additional trajectories (see Fig. 23).

For the delay-coordinate map, the lag is chosen to coincide with the zero-order-hold sampling time, namely, $\Delta t = 20$ ms, to retrieve the intersections with the Poincaré section. To improve accuracy, we use an overembedding dimension of 15.

As discussed in the previous examples, Fig. 24 shows short-time trajectory predictions, the PDFs of reduced coordinates, and a three-dimensional projection of the delay embedding, where the two test trajectories are seen to approach the chaotic invariant set.

V. CONCLUSIONS

We have shown that a data-driven approach based on a recent extension of spectral submanifold (SSM) theory to delay differential equations (DDEs) yields predictive reduced-order models for autonomous systems with bounded delays. These SSM-reduced models remain accurate even in the presence of chaotic dynamics and without prior knowledge of the number or magnitude of delays.

Furthermore, parametric SSM-reduction provides models that remain predictive across both local and global bifurcations, while revealing the mechanisms underlying loss of stability in the infinite-dimensional phase space of the underlying and possibly unknown DDE.

In the extension of the theory to nonautonomous DDEs with periodic delay, a family of d-dimensional SSMs exists, parametrized by time on a periodic interval, all of which are tangent to a time-periodic spectral subspace and with at least C^1 regularity. We have recalled the underlying theory in Theorem 1 and extended it to systems with periodic delays in Theorem 2, with a proof in Appendix C. This extension enables the rigorously justified reduction of experimental data from a PD-controlled mechanical system subject to feedback delay and the quantization effect of the digital controller.

We note that all results presented here concern bounded delays. Extensions to systems with unbounded delay, or memory effects, are an active area of research. Theoretical foundations can be found in Ref. 53.

ACKNOWLEDGMENTS

This work was supported by the Swiss National Science Foundation (Grant No. 200021_214908). The authors are grateful to Professor Gábor Stépán for making the experimental data publicly available.

AUTHOR DECLARATIONS

Conflict of Interest

The authors have no conflicts to disclose.

Author Contributions

Giacomo Abbasciano: Conceptualization (equal); Data curation (lead); Formal analysis (lead); Investigation (lead); Methodology (lead); Software (lead); Validation (lead); Visualization (lead); Writing – original draft (lead); Writing – review & editing (lead). **Gergely Buza:** Conceptualization (equal); Formal analysis (lead); Investigation (lead); Methodology (lead); Writing – original draft (supporting); Writing – review & editing (equal). **George Haller:** Conceptualization (lead); Formal analysis (supporting); Funding acquisition (lead); Investigation (supporting); Methodology (supporting); Project administration (lead); Supervision (lead); Writing – review & editing (equal).

10 November 2026 11:30:50

© Author(s) 2026

DATA AVAILABILITY

The software and data that support the findings of this study are openly available in GitHub at https://github.com/haller-group/SSMLearn Ref. 61.

APPENDIX A: DATA-DRIVEN SPECTRAL SUBMANIFOLDS FOR AUTONOMOUS SYSTEMS

The theory of SSMs and their data-driven reconstruction via delay embedding is well established (see Ref. 11). Here, we summarize only the essentials to the present analysis.

1. SSM reconstruction via delay embedding

Full-state measurements are typically unavailable,[13,43] motivating reconstruction from limited observables. By Takens' theorem,[39] a d-dimensional manifold can be embedded using $m > 2d$ delayed samples of a generic scalar observable.[54]

The reduced dynamics

$$\dot{\eta} = R(\eta), \quad \eta \in \mathbb{R}^d,$$

on a d-dimensional SSM $\mathcal{W}(E)$, tangent to a spectral subspace E, with associated flow $R^t : \eta_0 \mapsto \eta(t)$, are conjugate to the restriction of the full system flow $F^t : \mathbb{R}^n \to \mathbb{R}^n$ to $\mathcal{W}(E) \subset \mathbb{R}^n$. This conjugacy is realized through a smooth parametrization $M : \mathbb{R}^d \to \mathbb{R}^n$, satisfying

$$F^t \circ M = M \circ R^t. \tag{A1}$$

Consider a scalar time series $s(t) = \xi(x(t))$, obtained by observing the full system, where $\xi : \mathbb{R}^n \to \mathbb{R}$. The delay-coordinate map $\Psi : \mathbb{R}^n \to \mathbb{R}^m$ is constructed by stacking m uniformly spaced samples of $s(t)$ with sampling interval T_s,

$$y(t) = \Psi(x(t)) = [\, s(t),\, s(t+T_s),\, \ldots,\, s(t+(m-1)T_s)\,]^{\mathrm{T}} \in \mathbb{R}^m. \tag{A2}$$

Denote by $F^t_\Psi : \mathbb{R}^m \to \mathbb{R}^m$ the induced flow in the delay embedding space. If $\xi(0) = 0$, then the equilibrium $x = 0$ maps to the fixed point $y = 0$, i.e., $F^t_\Psi(0) = 0$. For a generic observable ξ, and assuming nondegeneracy conditions on the SSM-reduced dynamics, Takens' theorem guarantees that for $m > 2d$, the restriction of Ψ to $\mathcal{W}(E)$ yields an embedding into $\mathbb{R}^m$ with probability one. As a result, the image $\widetilde{\mathcal{W}}(E) = \Psi(\mathcal{W}(E))$ is diffeomorphic to $\mathcal{W}(E)$.

This results enables the identification of an SSM anchored at $y = 0$ in delay space via the conjugacy between the embedded dynamics F^t_Ψ on $\widetilde{\mathcal{W}(E)}$ and the reduced dynamics on $\mathcal{W}(E)$,

$$F^t_\Psi \circ \Psi = \Psi \circ F^t\big|_{\mathcal{W}(E)}. \tag{A3}$$

2. Data-driven modeling of spectral submanifolds in a delay embedding space

Following Liu *et al.*,[43] we denote by $y \in \mathbb{R}^m$ the delay-embedded observations, and by $\eta \in \mathbb{R}^d$ the reduced coordinates associated with the spectral subspace E of $D\Psi(0)E$. In a neighborhood of the fixed point, the embedded SSM can be locally represented as a polynomial graph tangent to this linear subspace.

Let $\mathcal{K}$ be the maximal degree of the expansion. We approximate $\mathcal{W}(E)$ through the parametrization

$$M(\eta) = V_1\,\eta + \sum_{|\mathbf{k}|=2}^{\mathcal{K}} V_{\mathbf{k}}\,\eta^{\mathbf{k}}, \qquad \mathbf{k} = (k_1,\ldots,k_d) \in \mathbb{N}^d, \quad V_1, V_{\mathbf{k}} \in \mathbb{R}^{m\times d}, \tag{A4}$$

where $\eta^{\mathbf{k}} = \eta_1^{k_1}\cdots\eta_d^{k_d}$ denotes the monomial associated with the multi-index $\mathbf{k}$.

The reduced coordinates are obtained via projection, $\eta = V_1^{\mathrm{T}} y$, where $V_1 \in \mathbb{R}^{m\times d}$ has orthonormal columns spanning the tangent space of $\widetilde{\mathcal{W}(E)} \subset \mathbb{R}^m$ at $y = 0$. The coefficients are identified using SSMLearn[13] by solving

$$V^* = \left[V_1^*,\, V_{2:\mathcal{K}}^*\right] = \underset{V_1,\,\{V_{\mathbf{k}}\}_{|\mathbf{k}|\geq 2}}{\arg\min} \sum_j \left\| y_j - V_1\,V_1^{\mathrm{T}} y_j - \sum_{|\mathbf{k}|=2}^{\mathcal{K}} V_{\mathbf{k}}\,(\eta_j)^{\mathbf{k}} \right\|_2^2, \tag{A5}$$

subject to $V_1^{\mathrm{T}} V_1 = I$ and $V_1^{\mathrm{T}} V_{\mathbf{k}} = 0$ for all $|\mathbf{k}| \geq 2$.

3. Data-driven modeling of the SSM-reduced dynamics

In the present work, we approximated the reduced dynamics on the SSM using either polynomial regression or radial basis functions (RBFs) interpolation.

a. Polynomial reduced dynamics

We represent the reduced dynamics in polynomial form as

$$\dot{\eta} = R_1\,\eta + \sum_{|\mathbf{k}|=2}^{\mathcal{K}} R_{\mathbf{k}}\,\eta^{\mathbf{k}}, \quad \mathbf{k} = (k_1,\ldots,k_d) \in \mathbb{N}^d, \quad R_{\mathbf{k}} \in \mathbb{R}^{d\times d}, \tag{A6}$$

where the coefficient matrices are identified through a least-squares regression,

$$R^* = \underset{R}{\arg\min} \sum_j \left\| \dot{\eta}_j - \sum_{|\mathbf{k}|=1}^{\mathcal{K}} R_{\mathbf{k}}\,(\eta_j)^{\mathbf{k}} \right\|_2^2, \quad \mathbf{k} = (k_1,\ldots,k_d) \in \mathbb{N}^d, \qquad R = \left[R_1,\, R_{2:\mathcal{K}}\right] \in \mathbb{R}^{d\times\sum_{k=1}^{\mathcal{K}} d_k}. \tag{A7}$$

Here, the number of monomials of total degree k is $d_k = \binom{d+k-1}{k}$.

b. RBF reduced dynamics

The SSM-reduced dynamics can be approximated using RBFs, following Xu *et al.*,[44] in the form of a discrete-time map,

$$\eta_{n+1} = F(\eta_n) = \sum_{i=1}^{K} C_i\,k\big(\|\eta_n - \eta_i\|\big). \tag{A8}$$

Here, k is a radial kernel that depends on the distance between η_n and the sampled points η_i. In this work, we adopt the linear kernel $k(r) = r$ due to its simplicity and effectiveness.[15,19,44]

10 November 2026 11:30:50

© Author(s) 2026

4. Parametric SSM-reduced order models

About nonresonant points, the SSM and its associated reduced dynamics inherit smooth parameter dependence from the system vector field.[11,12] This justifies constructing parameter-dependent SSMs via polynomial regression or smooth interpolation. This is achieved by interpolating the coefficients of the multivariate polynomial expansions describing the reduced space, the manifold and its reduced dynamics (e.g., using splines or linear interpolation, as in this paper), resulting in coefficient functions of $\mu \in \mathbb{R}^p$, following Abbasciano *et al.*[19]

The question of persistence and regularity of SSM across resonant points is addressed in Ref. 25. As mentioned therein, the limitations that resonance bring about are less pronounced in the data-driven setting. The corresponding reduced-order models can capture local bifurcations of equilibria and invariant tori, as well as global bifurcation phenomena in a neighborhood of the anchor point.

For illustration, in the case of a two-dimensional SSM ($d=2$), the parameter-dependent reduced dynamics in modal coordinates can be expressed as

$$\begin{aligned}\dot{\eta}_1 &= \lambda_1(\mu)\eta_1 + a_{11}(\mu)\eta_1^2 + a_{12}(\mu)\eta_1\eta_2 + a_{13}(\mu)\eta_2^2 + \mathcal{O}\big(|\eta|^3\big),\\ \dot{\eta}_2 &= \lambda_2(\mu)\eta_2 + a_{21}(\mu)\eta_1^2 + a_{22}(\mu)\eta_1\eta_2 + a_{23}(\mu)\eta_2^2 + \mathcal{O}\big(|\eta|^3\big).\end{aligned} \tag{A9}$$

APPENDIX B: EQUATION-DRIVEN REDUCTION OF THE HUTCHINSON DELAY SYSTEM

1. Formal procedure for SSM reduction employed in Szaksz *et al.*[28]

We present the equation-driven SSM reduction of the Hutchinson delay system following Refs. 2, 28 based on previous work.[26,27] The Hutchinson equation, taken from Ref. 32, is

$$x'(t) = r\,x(t)\left(1 - \frac{x(t-\tau)}{K}\right), \quad r>0,\ K>0,\ \tau>0. \tag{B1}$$

Its equilibria are $x_* \in \{0, K\}$. Shifting the equilibrium $x_* = K$ to the origin, we obtain

$$\dot{y}(t) = L\,y(t) + R\,y(t-\tau) + N(y(t), y(t-\tau)), \tag{B2}$$

with $L=0$, $R=-r$, and $N(u,v) = -\frac{r}{K}\,u\,v$. The state at time t is the history segment $y_t(\vartheta) = y(t+\vartheta)$, $\vartheta \in [-\tau, 0]$, with phase space $X := C([-\tau, 0], \mathbb{R})$.

For $r=1.8$, $K=10$, and $\tau=1$, the dominant eigenvalues of the linearized system (B2) form an unstable complex-conjugate pair. The existence of a C^∞ SSM follows from Ref. 9, since the corresponding spectral subspace is spanned by eigenvectors associated with a simple unstable complex pair. We construct a two-dimensional SSM associated with the dominant complex-conjugate eigenvalue pair and use one complex reduced coordinate $z \in \mathbb{C}$, corresponding to two real dimensions via $(\Re z, \Im z)$.

The characteristic matrix is

$$\Delta(\mu) := \mu I - L - Re^{-\mu\tau}. \tag{B3}$$

Computing the infinitely many roots of the quasi-polynomial (B3) is nontrivial. To this end, we use the method developed in Refs. 49, 50 to compute the dominant part of the spectrum, as shown in Fig. 4. This yields $\lambda_1 = 0.097 - 1.6i$, $\lambda_2 = \overline{\lambda_1} = 0.097 + 1.6i$, while all other eigenvalues satisfy $\Re(\lambda_j) < \Re(\lambda_1)$. To construct a third-order polynomial expansion of the manifold, we must verify that the nonresonance conditions up to cubic order are satisfied, namely, $\Delta(j\lambda_1 + k\lambda_2) \neq 0$ for all integer pairs (j, k) with $j+k \in \{2, 3\}$. Equivalently, $\Delta(2\lambda_1)$, $\Delta(\lambda_1+\lambda_2)$, $\Delta(2\lambda_2)$, $\Delta(3\lambda_1)$, $\Delta(2\lambda_1+\lambda_2)$, $\Delta(\lambda_1+2\lambda_2)$, and $\Delta(3\lambda_2)$ must all be nonzero. This prevents division by zero when solving the homological equations.

The right eigenfunctions are

$$\phi_1(\vartheta) = q_1 e^{\lambda_1\vartheta}, \quad \phi_2(\vartheta) = q_2 e^{\lambda_2\vartheta}, \quad \vartheta \in [-\tau, 0], \qquad \text{where } q_1 = \bar{q}_2 \in \mathbb{C}\backslash\{0\}. \tag{B4}$$

For convenience, we set $q_1 = 1$. The left eigenfunctions are

$$\psi_1(\theta) = p_1^*\left(I + Re^{-\lambda_1\tau}\frac{e^{\lambda_1\theta} - 1}{\lambda_1}\right), \quad \psi_2 = \bar{\psi}_1, \quad \theta \in [0, \tau], \qquad p_1^* \in \mathbb{C}\backslash\{0\}. \tag{B5}$$

a. Normalization

Imposing $\langle \psi_i, \phi_i \rangle = 1$ for $i \in \{1, 2\}$ fixes the remaining degree of freedom: $p_i^* = 1/(\Delta'(\lambda_i)q_i)$, where the pairing is defined by

$$\langle \Psi, \Phi \rangle = \Psi(0)\,\Phi(0) + \int_0^\tau \Psi'(\theta)\,\Phi(-\theta)\,d\theta. \tag{B6}$$

Henceforth, ψ_1 denotes the normalized adjoint eigenfunction.

b. SSM parametrization in history space

We parametrize histories on the two-dimensional SSM by $z \in \mathbb{C}$:

$$y_t(\cdot) = W(z(t), \bar{z}(t), \cdot).$$

The reality of the manifold requires $W(\bar{z}, z, \vartheta) = \overline{W(z, \bar{z}, \vartheta)}$. We expand up to cubic order, $W = W_1 + W_2 + W_3 + O(|z|^4)$, with

$$\begin{aligned} W_1(z, \bar{z}, \vartheta) &= W_{10}(\vartheta)z + W_{01}(\vartheta)\bar{z} = \phi_1(\vartheta)z + \phi_2(\vartheta)\bar{z},\\ W_2(z, \bar{z}, \vartheta) &= \frac{1}{2}\Big(W_{20}(\vartheta)z^2 + 2W_{11}(\vartheta)z\bar{z} + W_{02}(\vartheta)\bar{z}^2\Big),\\ W_3(z, \bar{z}, \vartheta) &= \frac{1}{6}\Big(W_{30}(\vartheta)z^3 + 3W_{21}(\vartheta)z^2\bar{z}\\ &\qquad + 3W_{12}(\vartheta)z\bar{z}^2 + W_{03}(\vartheta)\bar{z}^3\Big).\end{aligned} \tag{B7}$$

With $\dot{z} = f(z, \bar{z})$ and $\dot{\bar{z}} = \overline{f(z, \bar{z})}$, the reduced dynamics truncated at cubic order are

$$\begin{aligned}\dot{z} &= \lambda z + \beta_{20}z^2 + \beta_{11}z\bar{z} + \beta_{02}\bar{z}^2 + \beta_{30}z^3 + \beta_{21}z^2\bar{z} + \beta_{12}z\bar{z}^2\\ &\quad + \beta_{03}\bar{z}^3 + O(|z|^4),\\ \dot{\bar{z}} &= \bar{\lambda}\bar{z} + \overline{\beta_{02}}z^2 + \overline{\beta_{11}}z\bar{z} + \overline{\beta_{20}}\bar{z}^2 + \overline{\beta_{03}}z^3 + \overline{\beta_{12}}z\bar{z}^2 + \overline{\beta_{21}}\bar{z}^2 z\\ &\quad + \overline{\beta_{30}}\bar{z}^3 + O(|z|^4).\end{aligned} \tag{B8}$$

10 November 2026 11:30:50

© Author(s) 2026

The invariance of the spectral submanifold can be expressed by the PDE

$$\frac{\partial}{\partial t} y_t = \frac{\partial}{\partial \vartheta} y_t, \tag{B9}$$

which yields equations in the interior, $\vartheta \in [-\tau, 0)$, and at the boundary, $\vartheta = 0$.

c. Interior invariance PDE

$\partial_\vartheta W = \partial_z W \dot{z} + \partial_{\bar{z}} W \dot{\bar{z}} \quad , \quad \vartheta \in [-\tau, 0).$

The left-hand side, up to cubic order, can be computed from (B7) as

$$\begin{aligned}\partial_\vartheta W &= \partial_\vartheta W_1 + \partial_\vartheta W_2 + \partial_\vartheta W_3 + O(|z|^4) \\ &= \left(W'_{10} z + W'_{01} \bar{z}\right) + \frac{1}{2}\left(W'_{20} z^2 + 2W'_{11} z\bar{z} + W'_{02} \bar{z}^2\right) + \frac{1}{6}\left(W'_{30} z^3 + 3W'_{21} z^2\bar{z} + 3W'_{12} z\bar{z}^2 + W'_{03} \bar{z}^3\right) + O(|z|^4).\end{aligned} \tag{B10}$$

For the right-hand side, we obtain

$$\begin{aligned}\partial_z W \dot{z} &= \lambda W_{10} z + \left((W_{10}\beta_{20} + \lambda W_{20}) z^2 + (W_{10}\beta_{11} + \lambda W_{11}) z\bar{z} + W_{10}\beta_{02}\, \bar{z}^2\right) + \Big((W_{10}\beta_{30} + W_{20}\beta_{20} + \tfrac{\lambda}{2} W_{30}) z^3 \\ &\quad + (W_{10}\beta_{21} + W_{20}\beta_{11} + W_{11}\beta_{20} + \lambda W_{21}) z^2\bar{z} + (W_{10}\beta_{12} + W_{20}\beta_{02} + W_{11}\beta_{11} + \tfrac{\lambda}{2} W_{12}) z\bar{z}^2 + (W_{10}\beta_{03} + W_{11}\beta_{02})\bar{z}^3\Big) + O(|z|^4), \\ \partial_{\bar{z}} W \dot{\bar{z}} &= \bar{\lambda} W_{01}\, \bar{z} + \left(W_{01}\bar{\beta}_{02}\, z^2 + (W_{01}\bar{\beta}_{11} + \bar{\lambda} W_{11}) z\bar{z} + (W_{01}\bar{\beta}_{20} + \bar{\lambda} W_{02})\bar{z}^2\right) + \Big((W_{01}\bar{\beta}_{03} + W_{11}\bar{\beta}_{02}) z^3 + (W_{01}\bar{\beta}_{12} + W_{11}\bar{\beta}_{11} + W_{02}\bar{\beta}_{02} \\ &\quad + \tfrac{\bar{\lambda}}{2} W_{21}) z^2\bar{z} + (W_{01}\bar{\beta}_{21} + W_{11}\bar{\beta}_{20} + W_{02}\bar{\beta}_{11} + \bar{\lambda} W_{12}) z\bar{z}^2 + (W_{01}\bar{\beta}_{30} + W_{02}\bar{\beta}_{20} + \tfrac{\bar{\lambda}}{2} W_{03})\bar{z}^3\Big) + O(|z|^4).\end{aligned} \tag{B11}$$

d. Boundary invariance PDE

$\partial_z W(0)\dot{z} + \partial_{\bar{z}} W(0)\dot{\bar{z}} = L\, W(0) + R\, W(-\tau) + N(W(0), W(-\tau))$ at $\vartheta = 0$.

The expansion of the nonlinearity up to cubic order is obtained by substituting (B7).
Define $\phi_{1,\tau} = e^{-\lambda\tau}$ and $\phi_{2,\tau} = e^{-\bar{\lambda}\tau}$. Truncating W at second order is sufficient for a third-order expansion of N,

$$\begin{aligned}N\big(W(0), W(-\tau)\big) &= -\frac{r}{K}\left(\phi_{1,\tau} z^2 + (\phi_{1,\tau} + \phi_{2,\tau}) z\bar{z} + \phi_{2,\tau}\bar{z}^2\right) - \frac{r}{2K}\Big(\big(W_{20}(-\tau) + \phi_{1,\tau} W_{20}(0)\big) z^3 \\ &\quad + \big(W_{20}(-\tau) + 2W_{11}(-\tau) + 2\phi_{1,\tau} W_{11}(0) + \phi_{2,\tau} W_{20}(0)\big) z^2\bar{z} \\ &\quad + \big(W_{02}(-\tau) + 2W_{11}(-\tau) + \phi_{1,\tau} W_{02}(0) + 2\phi_{2,\tau} W_{11}(0)\big) z\bar{z}^2 + \big(W_{02}(-\tau) + \phi_{2,\tau} W_{02}(0)\big)\bar{z}^3\Big) + O(|z|^4).\end{aligned} \tag{B12}$$

We compute approximate solutions of the invariance PDE by solving the associated homological equations obtained from the interior and boundary invariance conditions order by order. This procedure yields the coefficients of both the manifold parametrization and the reduced dynamics up to the desired order, here cubic.

e. Order 1

Solving the interior invariance equation at first order, using (B10) and (B11), yields

$$W_{10}(\vartheta) = q_1 e^{\lambda\vartheta}, \quad W_{01}(\vartheta) = q_2 e^{\bar{\lambda}\vartheta}. \tag{B13}$$

Substitution into the boundary invariance equations, derived from (B11) and (B12), leads to

$$\begin{aligned}[z]: &\quad \lambda = L + Re^{-\lambda\tau} \iff \Delta(\lambda) = 0, \\ [\bar{z}]: &\quad \bar{\lambda} = L + Re^{-\bar{\lambda}\tau} \iff \Delta(\bar{\lambda}) = 0,\end{aligned}$$

which ensures tangency to the spectral subspace spanned by the right eigenfunctions in X.

f. Order 2

From (B10) and (B11), we derive the second-order interior invariance equations, solve them by variation of constants, evaluate them at $\vartheta \in \{-\tau, 0\}$, and substitute the resulting expressions into the boundary equations. Together with the following projection conditions, which we arbitrarily impose to fix the coefficients β_{ij} by removing the second-order component of the manifold along the spectral subspace directions,

$$\langle \psi_1, W_{jk} \rangle = 0, \quad \langle \psi_2, W_{jk} \rangle = 0, \quad j + k = 2, \tag{B14}$$

this yields, for each monomial, a 3×3 linear system with unknowns $(W_{jk}(0), \beta_{jk}, \overline{\beta}_{jk})$. The projections (B14) are conditions chosen arbitrarily to render the system determined. This choice forces the

10 November 2026 11:30:50

© Author(s) 2026

component tangent to the spectral subspace entirely into β_{jk} rather than W_{jk}.

g. Notation for the projections

For any scalar exponential, define

$$\Pi_i(a) := \langle \psi_i, e^{a\vartheta} \rangle = \frac{1}{\Delta'(\lambda_i)} \left[1 + R\, e^{-\lambda_i \tau} \frac{e^{(\lambda_i - a)\tau} - 1}{\lambda_i - a} \right], \quad a \neq \lambda_i, \quad i = 1, 2.$$

In the limit $a \to \lambda_i$,

$$\Pi_i(\lambda_i) = \frac{1}{\Delta'(\lambda_i)} \left[1 + R\, \tau\, e^{-\lambda_i \tau} \right] = 1.$$

As an example, we compute $(W_{20}(0), \beta_{20}, \overline{\beta}_{02})$. The boundary equation is

$$\underbrace{\left(\lambda - \tfrac{L}{2} - \tfrac{R}{2}\phi_{1,\tau}^2\right)}_{=:a_{20} = \frac{1}{2}\Delta(2\lambda) \to \text{nonres. cond.}} W_{20}(0) + \underbrace{\left(1 - \tfrac{R}{\lambda}(\phi_{1,\tau}^2 - \phi_{1,\tau})\right)}_{=:b_{20}} \beta_{20} + \underbrace{\left(1 - \tfrac{R}{\overline{\lambda} - 2\lambda}(\phi_{2,\tau} - \phi_{1,\tau}^2)\right)}_{=:c_{20}} \overline{\beta_{02}} = \underbrace{-\tfrac{r}{K}\phi_{1,\tau}}_{=:d_{20}}. \tag{B15}$$

The projection conditions read

$$0 = \langle \psi_i, W_{20}(\vartheta) \rangle = \Pi_i(2\lambda)\, W_{20}(0) + \frac{2\beta_{20}}{\lambda}\big(\Pi_i(2\lambda) - \Pi_i(\lambda)\big) + \frac{2\overline{\beta_{02}}}{\overline{\lambda} - 2\lambda}\big(\Pi_i(\overline{\lambda}) - \Pi_i(2\lambda)\big), \quad i \in \{1, 2\}. \tag{B16}$$

This leads to the following linear system for $(W_{20}(0), \beta_{20}, \overline{\beta}_{02})$:

$$\begin{bmatrix} \frac{1}{2}\Delta(2\lambda) & b_{20} & c_{20} \\ \Pi_1(2\lambda) & \frac{2}{\lambda}\big(\Pi_1(2\lambda) - \Pi_1(\lambda)\big) & \frac{2}{\overline{\lambda} - 2\lambda}\big(\Pi_1(\overline{\lambda}) - \Pi_1(2\lambda)\big) \\ \Pi_2(2\lambda) & \frac{2}{\lambda}\big(\Pi_2(2\lambda) - \Pi_2(\lambda)\big) & \frac{2}{\overline{\lambda} - 2\lambda}\big(\Pi_2(\overline{\lambda}) - \Pi_2(2\lambda)\big) \end{bmatrix} \times \begin{bmatrix} W_{20}(0) \\ \beta_{20} \\ \overline{\beta_{02}} \end{bmatrix} = \begin{bmatrix} d_{20} \\ 0 \\ 0 \end{bmatrix}. \tag{B17}$$

The interior equation then reconstructs $W_{20}(\vartheta)$. The same procedure applies to $(W_{11}(0), \beta_{11}, \overline{\beta}_{11})$ and $(W_{02}(0), \beta_{02}, \overline{\beta}_{20})$.

h. Order 3

Proceeding as at second order, the cubic interior equations, derived from (B10) and (B11), are solved by variation of constants, evaluated at $\vartheta \in \{-\tau, 0\}$, and substituted into the boundary equations. Together with (B14) applied for $j + k = 3$, each monomial yields a 3×3 linear system for $(W_{jk}(0), \beta_{jk}, \overline{\beta}_{jk})$, for all $j + k = 3$.

Again, as an example, we present the computation for $(W_{30}(0), \beta_{30}, \overline{\beta}_{03})$. The boundary equation is

$$\left(\tfrac{\lambda}{2} - \tfrac{L}{6}\right) W_{30}(0) + \beta_{30} + \overline{\beta_{03}} - \tfrac{R}{6} W_{30}(-\tau) = D_{30}, \tag{B18}$$

with projection constraints

$$0 = \langle \psi_i, W_{30} \rangle = \Pi_i(3\lambda) W_{30}(0) + \mathcal{J}_{30}^{(i)} + 6\beta_{30} \frac{\Pi_i(3\lambda) - \Pi_i(\lambda)}{2\lambda} + 6\overline{\beta_{03}} \frac{\Pi_i(\overline{\lambda}) - \Pi_i(3\lambda)}{\overline{\lambda} - 3\lambda}. \tag{B19}$$

Hence, the linear system for $(W_{30}(0), \beta_{30}, \overline{\beta}_{03})$ reads

$$\begin{bmatrix} A_{30} & B_{30} & C_{30} \\ \Pi_1(3\lambda) & 6\frac{\Pi_1(3\lambda) - \Pi_1(\lambda)}{2\lambda} & 6\frac{\Pi_1(\overline{\lambda}) - \Pi_1(3\lambda)}{\overline{\lambda} - 3\lambda} \\ \Pi_2(3\lambda) & 6\frac{\Pi_2(3\lambda) - \Pi_2(\lambda)}{2\lambda} & 6\frac{\Pi_2(\overline{\lambda}) - \Pi_2(3\lambda)}{\overline{\lambda} - 3\lambda} \end{bmatrix} \begin{bmatrix} W_{30}(0) \\ \beta_{30} \\ \overline{\beta_{03}} \end{bmatrix} = \begin{bmatrix} E_{30} \\ -\mathcal{J}_{30}^{(1)} \\ -\mathcal{J}_{30}^{(2)} \end{bmatrix}, \tag{B20}$$

where

$$A_{30} := \left(\tfrac{\lambda}{2} - \tfrac{L}{6}\right) - \tfrac{R}{6}\phi_{1,\tau}^3 = \frac{1}{6}\Delta(3\lambda), \quad B_{30} := 1 - R\,\frac{\phi_{1,\tau}^3 - \phi_{1,\tau}}{2\lambda}, \quad C_{30} := 1 - R\,\frac{\phi_{2,\tau} - \phi_{1,\tau}^3}{\overline{\lambda} - 3\lambda},$$

$$D_{30} := -\frac{r}{2K}\Big(W_{20}(-\tau) + \phi_{1,\tau} W_{20}(0)\Big) - \Big(W_{20}(0)\beta_{20} + W_{11}(0)\overline{\beta_{02}}\Big), \quad E_{30} := D_{30} + \tfrac{R}{6} M_{30}.$$

Here, D_{30} depends only on second-order quantities, and the known forcing terms are

$$F_{30}(\vartheta) := 6\Big(W_{20}(\vartheta)\beta_{20} + W_{11}(\vartheta)\overline{\beta_{02}}\Big), \tag{B21}$$

$$M_{30} := \int_0^{-\tau} e^{3\lambda(-\tau - s)} F_{30}(s)\, ds, \quad \mathcal{J}_{30}^{(i)} := \left\langle \psi_i, \int_0^{\vartheta} e^{3\lambda(\vartheta - s)} F_{30}(s)\, ds \right\rangle.$$

The interior equation then reconstructs $W_{30}(\vartheta)$. After solving all homological equations, we verify the conditions implied by the reality of the manifold, $W_{jk}(\vartheta) = \overline{W_{kj}(\vartheta)}$. Higher-order expansions can be derived analogously, but the number of coefficients grows rapidly, especially with increasing SSM dimension. This motivates data-driven formulations even when the governing equations are available.

2. Alternative procedure for SSM-reduction developed in Ref. 9

The continuous embedding $\iota : X \hookrightarrow X^{\odot\star}$ defined by $\varphi \mapsto (\varphi(0), \varphi)$, where the sun-star subspace $X^{\odot\star} = \mathbb{R} \times L^\infty([-\tau, 0]; \mathbb{R})$ is introduced in Ref. 27, allows us to transition from the

10 November 2026 11:30:50

© Author(s) 2026

update rule (9) into the evolution Eq. (B22)

$$\iota \frac{d}{dt} y_t = A^{\odot\star} \iota y_t + R(y_t), \tag{B22a}$$

$$y_0 = \varphi, \quad \varphi \in O, \tag{B22b}$$

where the linear part is, explicitly for system (B22),

$$\mathrm{dom}\left(A^{\odot *}\right) = \left\{(c,\varphi) \;\middle|\; \varphi \text{ is Lipschitz with } \varphi(0) = c\right\}, \tag{B23a}$$

$$A^{\odot *}(c,\varphi) = (-r\varphi(-\tau), \dot{\varphi}), \tag{B23b}$$

while the nonlinear remainder is $R : X \to X^{\odot\star}$,

$$R(\varphi) = \left(-\frac{r}{K}\varphi(0)\varphi(-\tau), 0\right), \tag{B24}$$

so that $R \in C^\infty$, $R(0) = 0$ and the first derivative vanishes, that is, $DR(0) = 0$.

We define the spectral set $\Sigma = \{\lambda, \bar{\lambda}\}$. For each eigenvalue μ, the corresponding eigenfunction in X has the form $w_\mu(\vartheta) = q_\mu e^{\mu\vartheta}$. Since the DDE is scalar, we fix $q_\mu = 1$ and set

$$w_1(\vartheta) = e^{\lambda\vartheta}, \quad w_2(\vartheta) = e^{\bar{\lambda}\vartheta}.$$

We precompute derivatives of the nonlinear part R, as they will be useful below. The second derivative is

$$\left(D^2R(0)[u,v]\right) = \left(-\frac{r}{K}\left(u(0)v(-\tau) + v(0)u(-\tau)\right), 0\right) \quad u, v \in X. \tag{B25}$$

System (B22) has no cubic term, so $D^3R(0) = 0$. In particular,

$$\left(D^2R(0)[w_1,w_1]\right) = \left(-\frac{r}{K}\left(1\cdot e^{-\lambda\tau} + 1\cdot e^{-\lambda\tau}\right), 0\right) = \left(-\frac{2r}{K}e^{-\lambda\tau}, 0\right),$$

$$\left(D^2R(0)[w_1,w_2]\right) = \left(-\frac{r}{K}\left(e^{-\lambda\tau} + e^{-\bar{\lambda}\tau}\right), 0\right),$$

$$\left(D^2R(0)[w_2,w_2]\right) = \left(-\frac{2r}{K}e^{-\bar{\lambda}\tau}, 0\right).$$

We now seek a two-dimensional SSM tangent to the spectral subspace X_Σ. As in Sec. B 1, we wish to parametrize our reduced dynamics via a single complex coordinate $z \in \mathbb{C}$. Lemma 24 in Ref. 9, however, is posed with reduced space taken as the spectral subspace X_Σ. To bridge this gap, we introduce $\Theta : \mathbb{C} \to X_\Sigma$ given by

$$\Theta(z) = (\vartheta \mapsto z w_1(\vartheta) + \bar{z} w_2(\vartheta)).$$

The reduced dynamics may then be posed on $\mathbb{C}$, which will be of the general form

$$\dot{z}(z,\bar{z}) = g_1 z + \frac{1}{2}\left(g_{20}z^2 + 2g_{11}z\bar{z} + g_{02}\bar{z}^2\right) + \frac{1}{6}\left(g_{30}z^3 + 3g_{21}z^2\bar{z} + 3g_{12}z\bar{z}^2 + g_{03}\bar{z}^3\right) + \mathcal{O}(4). \tag{B26}$$

a. Computation of W. The formulas provided in Lemma 24,[9] extract W as a map $X_\Sigma \to X$. To relate this to our reduced coordinate z, we need to precompose with Θ, i.e., our final manifold embedding will be $W \circ \Theta : \mathbb{C} \to X$.

b. Linear term DW(0). The linear part is given as

$$DW(0) = \iota_\Sigma : X_\Sigma \hookrightarrow X,$$

enforcing the graph style of parametrization.

c. Quadratic term $D^2W(0)$. As in Lemma 24 of Buza and Haller,[9]

$$D^2W(0) = \iota^{-1}\int_0^\infty T^{\odot\star}(s)\, P_{\Sigma'}^{\odot\star}\, D^2R(0)\left[T(-s)\iota_\Sigma,\ T(-s)\iota_\Sigma\right] ds. \tag{B27}$$

On the spectral subspace X_Σ, the linear evolution is given by $T(-s)|_{X_\Sigma} = e^{-sA_\Sigma}$, so that

$$T(-s)w_1 = e^{-\lambda s}w_1, \quad T(-s)w_2 = e^{-\bar{\lambda}s}w_2. \tag{B28}$$

Therefore, using (B28) and bilinearity,

$$D^2R(0)\left[T(-s)w_i,\ T(-s)w_j\right] = e^{-(\lambda_i+\lambda_j)s}\, D^2R(0)[w_i,w_j], \quad (i,j) \in \{(1,1),(1,2),(2,2)\}. \tag{B29}$$

The three second-order directions in X_Σ are (w_1, w_1), (w_1, w_2), and (w_2, w_2). Applying (B27) to each of these pairs gives

$$D^2W(0)[w_i,w_j] = \iota^{-1}\int_0^\infty T^{\odot\star}(s)\, P_{\Sigma'}^{\odot\star}\, e^{-(\lambda_i+\lambda_j)s}\, D^2R(0)[w_i,w_j]\, ds, \quad (i,j) \in \{(1,1),(1,2),(2,2)\}. \tag{B30}$$

Under a suitable spectral gap assumption, so that the integrals converge and the resolvents exist, we use the resolvent identity

$$\iota^{-1}\int_0^\infty e^{-\nu s}\, T^{\odot\star}(s)\, P_{\Sigma'}^{\odot\star}\, ds = P_{\Sigma'}\, \iota^{-1}\, (\nu I - A^{\odot\star})^{-1}, \tag{B31}$$

where $\nu \in \mathbb{C}$ satisfies $\mathrm{Re}(\nu) > \sup\ \mathrm{Re}(\Sigma')$. Applying (B31) to (B30) yields

$$D^2W(0)[w_i,w_j] = P_{\Sigma'}\, \iota^{-1}\, \left((\lambda_i+\lambda_j)I - A^{\odot\star}\right)^{-1}\, D^2R(0)[w_i,w_j], \quad (i,j) \in \{(1,1),(1,2),(2,2)\}. \tag{B32}$$

$D^2R(0)[w_i, w_j]$, viewed in $X^{\odot\star} = \mathbb{R} \times L^\infty([-\tau,0],\mathbb{R})$, has the form $(c_{ij}, 0)$. The resolvent then becomes

$$(\nu I - A^{\odot\star})^{-1}(c,0) = \left(\Delta(\nu)^{-1}c,\ \vartheta \mapsto e^{\nu\vartheta}\Delta(\nu)^{-1}c\right), \tag{B33}$$

so that applying ι^{-1} simply extracts the history component

$$\iota^{-1}(\nu I - A^{\odot\star})^{-1}(c,0) = \vartheta \mapsto e^{\nu\vartheta}\Delta(\nu)^{-1}c. \tag{B34}$$

Therefore, defining

$$U_\nu(\vartheta; c) := e^{\nu\vartheta}\Delta(\nu)^{-1}c,$$

and using $P_{\Sigma'} = I - P_\Sigma$, Eq. (B32) becomes

$$D^2W(0)[w_i,w_j](\vartheta) = (I - P_\Sigma)\, U_{\lambda_i+\lambda_j}\left(\vartheta; c_{ij}\right), \quad (i,j) \in \{(1,1),(1,2),(2,2)\}, \tag{B35}$$

10 November 2026 11:30:50

© Author(s) 2026

where P_Σ is the spectral projection onto the 2D spectral subspace X_Σ.

We now need an explicit formula for P_Σ, that is, for $P_{\{\lambda\}}$ and $P_{\{\bar\lambda\}}$. We recall from Ref. 27, exercise IV.3.12,

$$P_{\{\lambda\}}u(\vartheta) = \frac{p^*\left[u(0) + \int_0^\tau d\zeta(s)\int_0^s e^{-\lambda\eta}u(\eta - s)\,d\eta\right]q}{p^*\Delta'(\lambda)q}e^{\lambda\vartheta}, \quad u \in X. \tag{B36}$$

Here,

$$\int_0^\tau d\zeta(s)\,u(-s) = Lu(0) + Ru(-\tau) = -ru(-\tau). \tag{B37}$$

Let q and p^* denote, respectively, the right and left eigenvectors associated with λ, satisfying

$$\Delta(\lambda)q = 0 \quad \text{and} \quad p^*\Delta(\lambda) = 0.$$

Substituting this into (B36), we obtain

$$P_{\{\lambda\}}u(\vartheta) = \frac{p^*\left[u(0) - r\int_0^\tau e^{-\lambda\eta}\,u(\eta - \tau)\,d\eta\right]q}{p^*\Delta'(\lambda)q}\,e^{\lambda\vartheta}. \tag{B38}$$

Define the scalar functionals

$$\alpha_\lambda(u) := \frac{p^*\left[u(0) - r\int_0^\tau e^{-\lambda s}\,u(s-\tau)\,ds\right]q}{p^*\Delta'(\lambda)q},$$
$$\alpha_{\bar\lambda}(u) := \frac{\overline{p}^*\left[u(0) - r\int_0^\tau e^{-\bar\lambda s}\,u(s-\tau)\,ds\right]\overline{q}}{\overline{p}^*\Delta'(\bar\lambda)\overline{q}}. \tag{B39}$$

Therefore, for $u(\vartheta) = Ce^{\nu\vartheta}$,

$$(P_\Sigma u)(\vartheta) = \alpha_\lambda(Ce^{\nu\cdot})\,e^{\lambda\vartheta} + \alpha_{\bar\lambda}(Ce^{\nu\cdot})\,e^{\bar\lambda\vartheta}. \tag{B40}$$

c.1 (w_i, w_j) component. Thus,

$$D^2W(0)[w_i, w_j](\vartheta) = U_{\lambda_i+\lambda_j}(\vartheta; c_{ij}) - \left(\alpha_\lambda U_{\lambda_i+\lambda_j}(\vartheta; c_{ij})e^{\lambda\vartheta} + \alpha_{\bar\lambda}U_{\lambda_i+\lambda_j}(\vartheta; c_{ij})e^{\bar\lambda\vartheta}\right), \tag{B41}$$
$$(i,j) \in \{(1,1),(1,2),(2,2)\}. \tag{B42}$$

d. Linear term DH(0). From Lemma 24 in Ref. 9, we have $DH(0) = A_\Sigma$. This translates to $g_1 = \lambda$ in (B26).

e. Quadratic term $D^2H(0)$. From Lemma 24 in Ref. 9,

$$D^2H(0) = \widetilde{P}_\Sigma^{\odot\star}\,D^2R(0)[\iota_\Sigma, \iota_\Sigma].$$

That is,

$$D^2H(0)[w_i, w_j](\vartheta) = \widetilde{P}_\Sigma^{\odot\star}\left(D^2R(0)[w_i, w_j]\right)(\vartheta) = \widetilde{P}_\Sigma^{\odot\star}(c_{ij}, 0)(\vartheta).$$

The projection onto $\{\lambda\}, \{\bar\lambda\}$ is, for a term $(c,0) \in X^{\odot\star}$,

$$\widetilde{P}_{\{\lambda\}}^{\odot\star}(c,0)(\vartheta) = \frac{p^*\,c}{p^*\Delta'(\lambda)q}\,q\,e^{\lambda\vartheta}, \quad \widetilde{P}_{\{\bar\lambda\}}^{\odot\star}(c,0)(\vartheta) = \frac{\overline{p}^*\,c}{\overline{p}^*\Delta'(\bar\lambda)\overline{q}}\,\overline{q}\,e^{\bar\lambda\vartheta}.$$

Moreover,

$$\widetilde{P}_\Sigma^{\odot\star} = \widetilde{P}_{\{\lambda\}}^{\odot\star} + \widetilde{P}_{\{\bar\lambda\}}^{\odot\star}$$

is precisely the projection onto the two-dimensional spectral subspace.

Explicitly,

$$D^2H(0)[w_i, w_j](\vartheta) = \frac{p^*\,c_{ij}}{p^*\Delta'(\lambda)q}\,q\,e^{\lambda\vartheta} + \frac{\overline{p}^*\,c_{ij}}{\overline{p}^*\Delta'(\bar\lambda)\overline{q}}\,\overline{q}\,e^{\bar\lambda\vartheta},$$
$$(i,j) \in \{(1,1),(1,2),(2,2)\}.$$

Any $u \in X_\Sigma$ can be written uniquely as $u = \Theta(z) = (\vartheta \mapsto zw_1(\vartheta) + \bar z w_2(\vartheta))$ for some $z \in \mathbb{C}$. Then, for the quadratic reduced coefficients in $\dot z$,

$$g_{20} = \frac{p^*\,c_{20}}{p^*\Delta'(\lambda)q}, \qquad g_{11} = \frac{p^*\,c_{11}}{p^*\Delta'(\lambda)q}, \qquad g_{02} = \frac{p^*\,c_{02}}{p^*\Delta'(\lambda)q}. \tag{B43}$$

Analogously, the coefficients in $\dot{\bar z}$ are obtained from the w_2 component by replacing λ with $\bar\lambda$ and (p^*, q) with $(\overline{p}^*, \overline{q})$.

f. Cubic term $D^3H(0)$. From Lemma 24 in Ref. 9, we have

$$\begin{aligned} D^3H(0)[u,v,w] = {} & \widetilde{P}_\Sigma^{\odot\star}D^3R(0)[DW(0)u, DW(0)v, DW(0)w] \\ & + \widetilde{P}_\Sigma^{\odot\star}\Big(D^2R(0)[D^2W(0)[u,v], DW(0)w] \\ & + D^2R(0)[D^2W(0)[u,w], DW(0)v] \\ & + D^2R(0)[D^2W(0)[v,w], DW(0)u]\Big). \end{aligned} \tag{B44}$$

For the Hutchinson equation, the vector field is quadratic, hence $D^3R(0) = 0$, and (B44) simplifies accordingly.

f.1 Cubic contribution z^3. We compute the trilinear term $D^3H(0)[w_1, w_1, w_1]$, which produces the z^3 contribution in the reduced dynamics. Evaluating at (w_1, w_1, w_1) and using $DW(0)w_1 = w_1$ and $D^2W(0)[w_1, w_1] = W_{20}$, we obtain

$$D^3H(0)[w_1, w_1, w_1] = 3\,\widetilde{P}_\Sigma^{\odot\star}D^2R(0)[W_{20}, w_1]. \tag{B45}$$

The corresponding boundary coefficient is

$$D^2R(0)[W_{20}, w_1] \equiv (c_{30}, 0) \quad \text{in } X^{\odot\star},$$

where

$$c_{30} := \left(D^2R(0)[W_{20}, w_1]\right)(0) = -\frac{r}{K}\left(e^{-\lambda\tau}W_{20}(0) + W_{20}(-\tau)\right). \tag{B46}$$

Projecting onto $\Sigma = \{\lambda, \bar\lambda\}$ gives

$$\begin{aligned} D^3H(0)[w_1,w_1,w_1](\vartheta) &= 3\,\widetilde{P}_\Sigma^{\odot\star}(c_{30},0)(\vartheta) \\ &= 3\left(\frac{p^*\,c_{30}}{p^*\Delta'(\lambda)q}\,q\,e^{\lambda\vartheta} + \frac{\overline{p}^*\,c_{30}}{\overline{p}^*\Delta'(\bar\lambda)\overline{q}}\,\overline{q}\,e^{\bar\lambda\vartheta}\right). \end{aligned}$$

f.2 Cubic contribution $z^2\bar z$. We next compute the trilinear term producing the $z^2\bar z$ contribution in the reduced dynamics. Evaluating at (w_1, w_1, w_2) and using the notation $W_{20} = D^2W(0)[w_1, w_1]$ and

10 November 2026 11:30:50

© Author(s) 2026

$W_{11} = D^2 W(0)[w_1, w_2]$, we obtain

$$
\begin{aligned}
&D^3 H(0)[w_1, w_1, w_2] \\
&\quad = \widetilde{P}_{\Sigma}^{\odot\star}\Big(D^2 R(0)[D^2 W(0)[w_1, w_1], w_2] \\
&\qquad + 2\, D^2 R(0)[D^2 W(0)[w_1, w_2], w_1] \Big) \qquad \text{(B47)} \\
&\quad = \widetilde{P}_{\Sigma}^{\odot\star}\Big(D^2 R(0)[W_{20}, w_2] + 2\, D^2 R(0)[W_{11}, w_1] \Big) \\
&\quad = \widetilde{P}_{\Sigma}^{\odot\star}(c_{21}, 0)(\vartheta) \qquad \text{(B48)} \\
&\quad = \left(\frac{p^*\, c_{21}}{p^* \Delta'(\lambda) q}\, q\, e^{\lambda \vartheta} + \frac{\overline{p}^*\, c_{21}}{\overline{p}^* \Delta'(\bar{\lambda}) \overline{q}}\, \overline{q}\, e^{\bar{\lambda}\vartheta} \right). \qquad \text{(B49)}
\end{aligned}
$$

Similarly, one obtains the terms corresponding to $z\bar{z}^2$ and $\bar{z}^3$.

g. Comparison between the two methods. The two methods presented in this appendix are equivalent. Here, we verify their equivalence by comparing the coefficients obtained for the manifold up to second order and for the reduced dynamics up to third order (Fig. 25).

g.1 SSM expansion coefficients. The manifold can be expressed as

$$
\begin{aligned}
W(z, \bar{z}, \vartheta) &= W_{10}(\vartheta) z + W_{01}(\vartheta) \bar{z} \\
&\quad + \frac{1}{2}\left(W_{20}(\vartheta) z^2 + 2 W_{11}(\vartheta) z\bar{z} + W_{02}(\vartheta) \bar{z}^2 \right) + O(|z|^3).
\end{aligned}
$$

g.2 SSM-reduced dynamics coefficients. Table I contains the reduced-dynamics coefficients obtained with both methods up to third order, yielding identical results:

a. Use of the table in the reduced dynamics. The coefficients reported in Table I are the complex coefficients b_{jk}, with an overall factor 10^{-2} collected outside the table. They enter directly into the reduced dynamics and its complex conjugate:

$$
\dot{z} = \lambda z + \sum_{j+k=2}^{3} b_{jk}\, z^j \bar{z}^k + \mathcal{O}(|z|^4), \quad \dot{\bar{z}} = \bar{\lambda} \bar{z} + \sum_{j+k=2}^{3} \overline{b_{jk}}\, \bar{z}^j z^k + \mathcal{O}(|z|^4). \qquad \text{(B50)}
$$

The equivalence of the two methods is expected, since the gauge is chosen identically in both cases. In both formulations, the tangential component of the manifold correction along the spectral subspace is

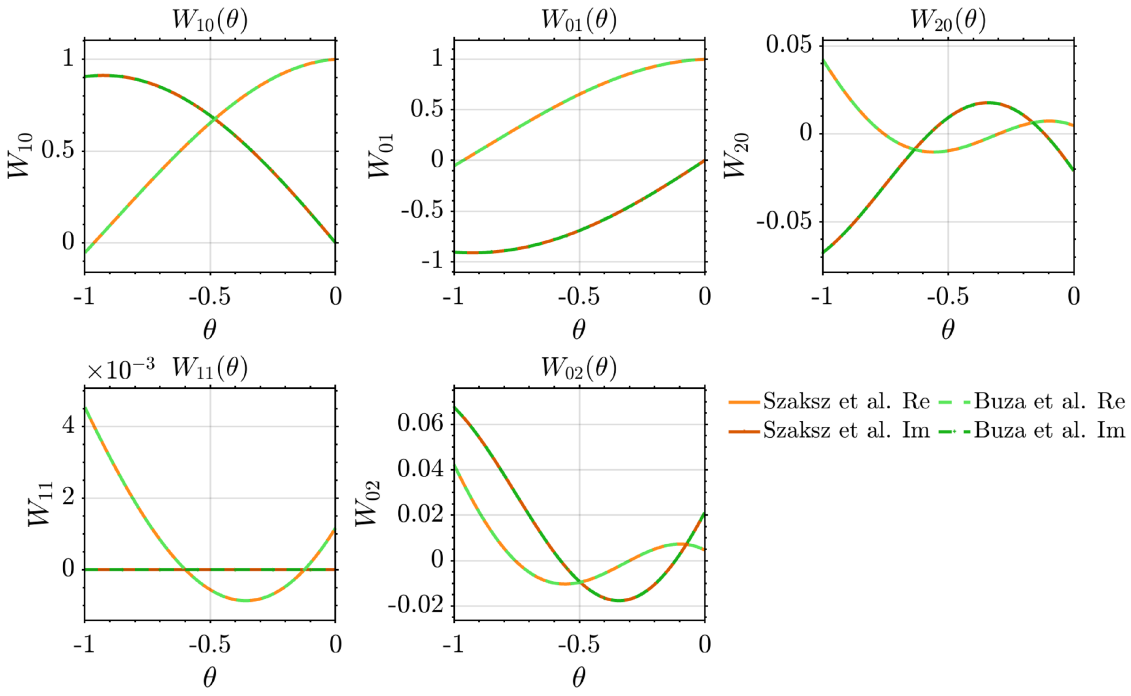


FIG. 25. Comparison of the manifold coefficients obtained with the two SSM-reduction approaches, namely, the equation-driven method in Ref. 28 and the semigroup-based method of Buza and Haller.[9] The figure shows real and imaginary parts of the first- and second-order coefficient functions $W_{10}(\vartheta)$, $W_{01}(\vartheta)$, $W_{20}(\vartheta)$, $W_{11}(\vartheta)$, and $W_{02}(\vartheta)$ over the delay interval $\vartheta \in [-\tau, 0]$. The two formulations yield the same manifold parametrization up to second order, consistently with the identical gauge choice used to remove tangential components along the spectral subspace.

10 November 2026 11:30:50

© Author(s) 2026

TABLE I. Reduced-dynamics coefficients (with a factor 10^{-2} collected outside the table).

20	11	02	30	21	12	03
7.2-4.2 i	0.55+0.82 i	−6.6+5.0 i	−0.39-0.073 i	−0.34+0.054 i	0.18-0.30 i	0.080-0.39 i

removed at every order higher than one. In Buza and Haller[9] formulation, this is expressed through the operator $(I - P_\Sigma)$, whereas in Szaksz *et al.*[28] formulation it is imposed through the pairing conditions $\langle W_{jk}, \psi_i \rangle = 0$. In other words, every higher-order manifold correction is chosen to be normal to the spectral subspace, while the tangential contribution is absorbed into the reduced dynamics coefficients.

APPENDIX C: EXTENSION OF SSM THEORY TO THE TIME-PERIODIC CASE

Let $X := C([-h, 0]; \mathbb{R}^n)$; here $h > 0$ denotes the maximal delay and $n \in \mathbb{N}$. Let $O \subset X$ denote an open set containing the origin. We consider systems of the form

$$\dot{x}(t) = f(t, x_t), \quad t \geq s \in \mathbb{R}, \tag{C1a}$$

$$x_s = u, \tag{C1b}$$

for $f : \mathbb{R} \times O \to \mathbb{R}^n$ continuous, time-periodic, i.e., $f(t+p, u) = f(t, u)$ for some $p > 0$ and all $(t, u) \in \mathbb{R} \times O$, and $f(t, 0) = 0$ for all $t \in \mathbb{R}$. We suppose moreover that $f(t, \cdot)$ is C^k, with $k \geq 1$ for all $t \in \mathbb{R}$. We shall also suppose $(t, u) \mapsto D_2^j f(t, u)$ is continuous for all $j \leq k$.

1. Sun-star setting

We cast the system (C1) into the sun-star setting of Diekmann *et al.*[27] (We assume familiarity with this setting. For details, we refer to Diekmann *et al.*[27] [Chapter II].) As usual, we denote by $\{T_0(t)\}_{t\geq 0}$ the shift semigroup acting on X; its generator by A_0. The $(\cdot)^\odot$ notation should be interpreted with respect to the semigroup $\{T_0(t)\}_{t\geq 0}$. Recall that $X^{\odot *} \cong \mathbb{R}^n \times L^\infty([-h, 0]; \mathbb{R}^n)$, and let $\iota : X \hookrightarrow X^{\odot *}$ denote the continuous embedding $u \mapsto (u(0), u)$ defined by the pairing between X and $X^\odot$. Let

$$r_i^{\odot *} := (e_i, 0) \in X^{\odot *}, \quad 1 \leq i \leq n,$$

where $(e_1, \ldots, e_n)$ is the canonical basis of $\mathbb{R}^n$. We declare $F : \mathbb{R} \times O \to X^{\odot *}$ to be

$$F(t, u) := \sum_{i=1}^{n} \langle f(t, u), e_i \rangle_{\mathbb{R}^n} r_i^{\odot *}. \tag{C2}$$

We further dissect (C2) into linear and nonlinear parts as

$$B(t) := D_2 F(t, 0),$$
$$R(t, u) := F(t, u) - D_2 F(t, 0)[u].$$

The integral equation,

$$x_t = T_0(t)u + \iota^{-1} \int_s^t T_0^{\odot *}(t - \tau) F(\tau, x_\tau)\, d\tau, \quad u \in O,\ t \geq s, \tag{C3}$$

determines a *time-dependent semiflow*, i.e., a continuous map $S : \mathcal{D}^S \to X$ defined by

$$S(t, s; u) := x_t, \quad \mathcal{D}(S) := \{(t, s; u) \in [s, \infty) \times \mathbb{R} \times O \mid t \in I_u\}, \tag{C4}$$

where x_t is determined by (C3) and I_u is the maximal interval of existence for (C3). For more details, see Ref. 55 [Section 2.3]. It can be shown that $S(t, s; \cdot)$ is of class C^k via an implicit function argument, as in Ref. 9 [Appendix B]. Moreover, solutions of (C1) and (C3) are in one-to-one correspondence, provided we allow (C1) to be satisfied in a weaker sense (see Ref. 27 [Section VII.6] for a more elaborate description).

a. Linearized semiflow

In Diekmann *et al.*,[27] [Chapter XII], it is shown, under the present assumption of B being strongly continuous, that

$$U(t, s)u = T_0(t - s)u + \iota^{-1} \int_s^t T_0^{\odot *}(t - \tau) B(\tau) U(\tau, s) u\, ds, \quad u \in X,\ t \geq s, \tag{C5}$$

uniquely determines a strongly continuous forward evolution system $\{U(t, s)\}_{t\geq s}$. Since $D_3 S(t, s; 0)$ also satisfies (C5), we must have that $D_3 S(t, s; 0) = U(t, s)$.

2. Recollection of Floquet theory

We collect the results we need from Ref. 27 [Chapter XIII] concerning Floquet theory in the following proposition.

Proposition 1: *The evolution system $\{U(t, s)\}_{t\geq s}$ defined by (C5) satisfies the following:*

(i) For all $t \geq s$, $U(t + p, s + p) = U(t, s)$.
(ii) The spectrum $\sigma(U) := \sigma(U(t + p, t))$ is independent of $t \in \mathbb{R}$, its only accumulation point is 0, and $\sigma(U(t + p, t)) \setminus \{0\} = \sigma_p(U(t + p, t)) \setminus \{0\}$.
(iii) For each spectral subset $\Sigma \subset \sigma(U) \setminus \{0\}$ there exists a continuous family projections $\{P_\Sigma(t)\}_{t\in\mathbb{R}}$ on X of finite dimensional range such that $P_\Sigma(t + p) = P_\Sigma(t)$ and $\sigma(U(t + p, t) P_\Sigma(t)) = \Sigma$ for all $t \in \mathbb{R}$. Moreover, for $t \geq s$, $U(t, s)$ maps $\mathrm{im}(P_\Sigma(s))$ onto $\mathrm{im}(P_\Sigma(t))$ isomorphically, such that $U(t, s) P_\Sigma(s) = P_\Sigma(t) U(t, s)$.

Proof. The first assertion is covered in Ref. 27 [Corollary XIII.2.2]. The second is a consequence of Ref. 27 [Theorem XIII.3.3(i)] and the fact that $U(t + p, t)^j$ is compact for some $j \in \mathbb{N}$ large enough—in particular, $\sigma(U(t + p, t))$ is as described in the statement and always contains 0. The third assertion follows from spectral properties of compact operators[27] [Theorem XIII.3.3(ii)]; and continuity of $t \mapsto P_\Sigma(t)$ follows from Ref. 56

10 November 2026 11:30:50

© Author(s) 2026

[Theorem IV.3.16] and time-periodicity of U. For a direct proof of continuity, see Ref. 55 [Appendix A.2]. □

3. Modification of the nonlinearity

To apply invariant manifold theory, one needs to control the global Lipschitz constant of the nonlinearity. The standard procedure in delay equations is to apply two cutoff functions (in order to preserve smoothness in a desired region),

$$R_{\rho,s}(t,u) := \chi_\rho(|P_\Sigma(s)u|_X)\chi_\rho(|u-P_\Sigma(s)u|_X)R(t,u),$$
$$(t,u)\in\mathbb{R}\times X,$$

where $\chi\colon[0,\infty)\to[0,1]$ is a C^∞ function satisfying

(i) $\chi(y)=1$ for $y\in[0,1]$,
(ii) $\chi(y)\in[0,1]$ for $y\in(1,2)$,
(iii) $\chi(y)=0$ for $y\geq 2$,
(iv) $|D\chi(y)|\leq 2$ for all $y\in\mathbb{R}^{\geq 0}$,

and $\chi_\rho(u):=\chi(u/\rho)$.

We remark that $(t,u)\mapsto R_{\rho,t}(t,u)$ preserves the smoothness of R on the set

$$\left\{(t,u)\in\mathbb{R}\times X \;\middle|\; |u-P_\Sigma(t)u|<\max\{\rho,2|P_\Sigma(t)u|\}\right\}. \tag{C6}$$

We quote the following Proposition from Ref. 55.

Proposition 2 (Proposition 6,[55]): *For $s\in\mathbb{R}$ and sufficiently small $\rho>0$, the operator $R_{\rho,s}(t,\cdot)$ is globally Lipschitz continuous for any $t\in\mathbb{R}$ with Lipschitz constant $Lip(R_{\rho,s}(t,\cdot))\to 0$ as $\rho\searrow 0$ independent of s.*

Hence, the time-dependent semiflow defined by

$$S_\rho(t,s;u)=T_0(t)u+\iota^{-1}\int_s^t T_0^{\odot *}(t-\tau)\left[B(\tau)S_\rho(\tau,s;u)+R_{\rho,\tau}(\tau,S_\rho(\tau,s;u))\right]d\tau,$$
$$u\in X,\ t\geq s, \tag{C7}$$

is globally defined for $\rho>0$ small enough, i.e., $\mathcal{D}(S_\rho)=[s,\infty)\times\mathbb{R}\times X$; moreover $S_\rho(t,s;\cdot)$ is Lipschitz on X.

Lemma 1: *For $t\geq s$, $S_\rho(t+p,s+p;\cdot)=S_\rho(t,s;\cdot)$.*

Proof. This is shown analogously to Diekmann *et al.*[27] [Proposition XIII.2.1] and Diekmann *et al.*[27] [Corollary XIII.2.2] noting that it only relies on the time-periodicity of the time-dependent term, not its linearity. □

4. Proof of Theorem 2

Proof of Theorem 2. We apply Ref. 57 [Theorem 3.1] to the maps $S_\rho(t+p,t;\cdot)$, $t\in\mathbb{R}$. For this, we set

$$\Phi_t(u)=L_tu+N_t(u),\quad (t,u)\in\mathbb{R}\times X,$$

with $L_t:=U(t+p,t)$ and $N_t(u):=S_\rho(t+p,t;\cdot)-U(t+p,t)$. We need to verify (H.3) and (H.4) of.[57] The prior follows from Proposition 1 applied with Σ as in the statement and the spectral radius formula,[58] [Theorem 5.2.7] whereas (H.4) follows from Proposition 2, by which we can also guarantee (H.3)–(H.4) hold for all $\{\Phi_t\}_{t\in\mathbb{R}}$ for a single choice of $\rho>0$.

Let $G_t(\gamma)$ denote the invariant Lipschitz manifold obtained by applying[57] [Theorem 3.1] to Φ_t according to the splitting $X=\mathrm{im}(P_\Sigma(t))\oplus\ker(P_\Sigma(t))$,

$$G_t(\gamma)=\left\{u\in X \;\middle|\; \text{there is a negative semiorbit of } \Phi_t,\ \{u_n\}_{n\leq 0},\ \text{with } u_0=u \text{ such that } \limsup_{n\to-\infty}\frac{1}{|n|}\ln|u_n|\leq-\ln\gamma\right\}.$$

We claim that $S_\rho(t,s,G_s(\gamma))\subset G_t(\gamma)$ for all $t\geq s$. Fix $u\in G_s(\gamma)$ and let $\{u_n\}_{n\leq 0}$ denote a negative semiorbit of Φ_s with $u_0=u$. Set $v:=S_\rho(t,s;u)$ and $v_n:=S_\rho(t,s;u_n)$, $n\leq 0$. Then $\Phi_t(v_n)=S_\rho(t+p,t;S_\rho(t,s;u_n))=S_\rho(t+p,s+p;u_{n+1})=v_{n+1}$ for $n\leq -1$ (recall Lemma 1), hence $\{v_n\}_{n\leq 0}$ is a negative semiorbit of Φ_t with $v_0=v$. Since $S_\rho(t,s;\cdot)$ is Lipschitzian, we have $|v_n|\leq C\,|u_n|$ for all $n\leq 0$ and hence

$$\limsup_{n\to-\infty}\frac{1}{|n|}\ln|v_n|\leq-\ln\gamma.$$

This shows the claim.

For the converse inclusion, $S_\rho(t,s,G_s(\gamma))\supset G_t(\gamma)$, we set $j\in\mathbb{N}$ to be the unique integer for which $t-jp\leq s<t-(j-1)p$. Fix $v\in G_t(\gamma)$ and let $\{v_n\}_{n\leq 0}$ denote a negative semiorbit under Φ_t such that $v_0=v$. We set $u:=S_\rho(s,t-jp;v_{-j})$, which is an element of $G_s(\gamma)$ by the previous claim and the fact that $v_{-j}\in G_{t-jp}(\gamma)=G_t(\gamma)$, which in turn follows from Ref. 57 [Theorem 3.1(ii)]. Computing $S_\rho(t,s;u)=\Phi_t^j(v_{-j})=v$ shows the converse inclusion.

Hence, $G_t(\gamma)=S_\rho(t,s,G_s(\gamma))$ for all $t\geq s$. This shows that $t\mapsto G_t(\gamma)$ is continuous. Recall from Ref. 57 [Equation (3.16)] and Proposition 2 that we can control the Lipschitz constant of the function whose graph is $G_t(\gamma)$ via adjusting ρ, uniformly with respect to t. Upon examining (C7) and the set (C6) on which $(t,u)\mapsto R_{\rho,t}(t,u)$ preserves the smoothness of R, we infer that Φ_t is C^k on a neighborhood of $G_t(\gamma)$. Thus, each $G_t(\gamma)$ is C^ℓ smooth according to Ref. 59. The local invariant manifold statements (i) and (ii) now follow by observing that $S_\rho=S$ on a small enough neighborhood of $[s,\infty)\times\mathbb{R}\times\{0\}$.

For statement (iii), we utilize the foliation part of Ref. 57 [Theorem 3.1]. For this, recall that leaves of said foliations are defined by

$$M_{t,u}(\gamma)=\left\{v\in X \;\middle|\; \limsup_{n\to\infty}\frac{1}{n}\ln|\Phi_t^n(u)-\Phi_t^n(v)|\leq\ln\gamma\right\}. \tag{C8}$$

We show $S_\rho(t,s,M_{s,u}(\gamma))\subset M_{t,S_\rho(t,s;u)}(\gamma)$ for $t\geq s$. Fix $v\in M_{s,u}(\gamma)$. We have $\Phi_t^n\circ S_\rho(t,s;\cdot)=S_\rho(t+np,s;\cdot)=S_\rho(t+np,s+np,\Phi_s^n(\cdot))$, hence

$$\limsup_{n\to\infty}\frac{1}{n}\ln|\Phi_t^n\circ S_\rho(t,s;v)-\Phi_t^n\circ S_\rho(t,s;u)|\leq\ln\gamma,$$

using the Lipschitzness of $S_\rho(t,s;\cdot)$ once more. This shows the desired property, and hence, upon using a contraction mapping argument to define π_t^ρ to be the continuous projection mapping $M_{t,u}(\gamma)$ to its unique intersection with $G_t(\gamma)$ (see Ref. 60 [Section 4]), we obtain (5) globally for the cutoff setting; the local version then follows as above.

Finally, we observe that (6) follows by (C8). Recall from Chen *et al.* [57] [Theorem 3.1(iv)] that one can replace γ by $\gamma-\varepsilon$ for $\varepsilon>0$

10 November 2026 11:30:50

© Author(s) 2026

$$
\begin{aligned}
\dot{\eta}_1 &= 0.07\eta_1 - 3\eta_2 + 0.6\eta_3 - 1\eta_4 - 1\eta_5 \\
&\quad -2\eta_6 + 0.01\eta_1^2 + 0.08\eta_1\eta_2 + 0.2\eta_1\eta_3 + 0.09\eta_1\eta_4 \\
&\quad -0.4\eta_1\eta_5 + 0.2\eta_1\eta_6 + 0.1\eta_2^2 + 0.5\eta_2\eta_3 + 0.3\eta_2\eta_4 \\
&\quad -0.9\eta_2\eta_5 + 0.5\eta_2\eta_6 + 0.6\eta_3^2 + 0.4\eta_3\eta_4 - 2\eta_3\eta_5 \\
&\quad 0.7\eta_3\eta_6 + 0.4\eta_4^2 - 0.3\eta_4\eta_5 + 2\eta_4\eta_6 + 1\eta_5^2 \\
&\quad 0.4\eta_5\eta_6 + 2\eta_6^2 + 0.003\eta_1^3 + 0.007\eta_1^2\eta_2 + 0.02\eta_1^2\eta_3 \\
&\quad -0.03\eta_1^2\eta_4 - 0.1\eta_1^2\eta_5 + 0.2\eta_1^2\eta_6 - 0.04\eta_1\eta_2^2 + 0.02\eta_1\eta_2\eta_3 \\
&\quad -0.3\eta_1\eta_2\eta_4 - 0.05\eta_1\eta_2\eta_5 - 0.1\eta_1\eta_2\eta_6 - 0.09\eta_1\eta_3^2 - 0.5\eta_1\eta_3\eta_4 \\
&\quad -1\eta_1\eta_3\eta_5 - 0.4\eta_1\eta_3\eta_6 - 0.4\eta_1\eta_4^2 + 1\eta_1\eta_4\eta_5 - 0.2\eta_1\eta_4\eta_6 \\
&\quad 0.4\eta_1\eta_5^2 + 0.7\eta_1\eta_5\eta_6 - 0.6\eta_1\eta_6^2 - 0.09\eta_2^3 + 0.06\eta_2^2\eta_3 \\
&\quad -0.5\eta_2^2\eta_4 + 0.1\eta_2^2\eta_5 - 0.9\eta_2^2\eta_6 + 0.3\eta_2\eta_3^2 - 0.2\eta_2\eta_3\eta_4 \\
&\quad -3\eta_2\eta_3\eta_5 - 3\eta_2\eta_3\eta_6 - 2\eta_2\eta_4^2 - 0.3\eta_2\eta_4\eta_5 - 4\eta_2\eta_4\eta_6 \\
&\quad -0.8\eta_2\eta_5^2 - 0.01\eta_2\eta_5\eta_6 - 7\eta_2\eta_6^2 + 0.2\eta_3^3 + 0.4\eta_3^2\eta_4 \\
&\quad -3\eta_3^2\eta_5 + 0.4\eta_3^2\eta_6 - 1\eta_3\eta_4^2 - 4\eta_3\eta_4\eta_5 + 1\eta_3\eta_4\eta_6 \\
&\quad -0.5\eta_3\eta_5^2 - 1 \times 10^1\eta_3\eta_5\eta_6 - 2 \times 10^1\eta_3\eta_6^2 - 2\eta_4^3 + 4\eta_4^2\eta_5 \\
&\quad -7\eta_4^2\eta_6 + 5\eta_4\eta_5^2 - 3 \times 10^1\eta_4\eta_5\eta_6 - 2 \times 10^1\eta_4\eta_6^2 + 2 \times 10^1\eta_5^3 \\
&\quad 3 \times 10^1\eta_5^2\eta_6 - 3 \times 10^1\eta_5\eta_6^2 + 6 \times 10^1\eta_6^3
\end{aligned}
$$

$$
\begin{aligned}
\dot{\eta}_2 &= 3\eta_1 + 2\eta_2 + 0.4\eta_3 - 0.6\eta_4 - 3\eta_5 \\
&\quad -4\eta_6 + 0.3\eta_1^2 + 1\eta_1\eta_2 + 2\eta_1\eta_3 + 0.2\eta_1\eta_4 \\
&\quad -4\eta_1\eta_5 - 0.5\eta_1\eta_6 + 1\eta_2^2 + 5\eta_2\eta_3 + 0.8\eta_2\eta_4 \\
&\quad -7\eta_2\eta_5 - 0.2\eta_2\eta_6 + 5\eta_3^2 - 0.04\eta_3\eta_4 - 1 \times 10^1\eta_3\eta_5 \\
&\quad -1\eta_3\eta_6 + 2\eta_4^2 + 3\eta_4\eta_5 + 9\eta_4\eta_6 + 1 \times 10^1\eta_5^2 \\
&\quad 1 \times 10^1\eta_5\eta_6 + 1 \times 10^1\eta_6^2 - 0.006\eta_1^3 - 0.2\eta_1^2\eta_2 + 0.3\eta_1^2\eta_3 \\
&\quad -0.8\eta_1^2\eta_4 - 1\eta_1^2\eta_5 - 0.8\eta_1^2\eta_6 - 0.8\eta_1\eta_2^2 + 0.9\eta_1\eta_2\eta_3 \\
&\quad -4\eta_1\eta_2\eta_4 - 4\eta_1\eta_2\eta_5 - 4\eta_1\eta_2\eta_6 + 0.5\eta_1\eta_3^2 - 3\eta_1\eta_3\eta_4 \\
&\quad -7\eta_1\eta_3\eta_5 - 4\eta_1\eta_3\eta_6 - 4\eta_1\eta_4^2 - 1\eta_1\eta_4\eta_5 - 3\eta_1\eta_4\eta_6 \\
&\quad -0.8\eta_1\eta_5^2 - 2\eta_1\eta_5\eta_6 - 3\eta_1\eta_6^2 - 0.9\eta_2^3 + 0.5\eta_2^2\eta_3 \\
&\quad -5\eta_2^2\eta_4 - 3\eta_2^2\eta_5 - 6\eta_2^2\eta_6 + 3\eta_2\eta_3^2 - 6\eta_2\eta_3\eta_4 \\
&\quad -2 \times 10^1\eta_2\eta_3\eta_5 - 2 \times 10^1\eta_2\eta_3\eta_6 - 1 \times 10^1\eta_2\eta_4^2 - 3\eta_2\eta_4\eta_5 - 2 \times 10^1\eta_2\eta_4\eta_6 \\
&\quad -2\eta_2\eta_5^2 + 6\eta_2\eta_5\eta_6 - 1 \times 10^1\eta_2\eta_6^2 + 0.7\eta_3^3 + 5\eta_3^2\eta_4 \\
&\quad -1 \times 10^1\eta_3^2\eta_5 + 6\eta_3^2\eta_6 - 1 \times 10^1\eta_3\eta_4^2 - 4 \times 10^1\eta_3\eta_4\eta_5 - 2 \times 10^1\eta_3\eta_4\eta_6 \\
&\quad -2 \times 10^1\eta_3\eta_5^2 - 4 \times 10^1\eta_3\eta_5\eta_6 - 6 \times 10^1\eta_3\eta_6^2 - 7\eta_4^3 + 3 \times 10^1\eta_4^2\eta_5 \\
&\quad -9\eta_4^2\eta_6 + 5 \times 10^1\eta_4\eta_5^2 - 5\eta_4\eta_5\eta_6 - 5 \times 10^1\eta_4\eta_6^2 + 7 \times 10^1\eta_5^3 \\
&\quad 2 \times 10^2\eta_5^2\eta_6 + 3 \times 10^1\eta_5\eta_6^2 + 3 \times 10^2\eta_6^3
\end{aligned}
$$

$$
\begin{aligned}
\dot{\eta}_3 &= 0.2\eta_1 + 1\eta_2 + 2\eta_3 - 8\eta_4 - 4\eta_5 \\
&\quad -5\eta_6 + 0.04\eta_1^2 + 0.3\eta_1\eta_2 + 0.7\eta_1\eta_3 + 0.3\eta_1\eta_4 \\
&\quad -1\eta_1\eta_5 + 0.7\eta_1\eta_6 + 0.5\eta_2^2 + 2\eta_2\eta_3 + 1\eta_2\eta_4 \\
&\quad -3\eta_2\eta_5 + 2\eta_2\eta_6 + 2\eta_3^2 + 2\eta_3\eta_4 - 6\eta_3\eta_5 \\
&\quad 2\eta_3\eta_6 + 1\eta_4^2 - 1\eta_4\eta_5 + 8\eta_4\eta_6 + 5\eta_5^2 \\
&\quad 1\eta_5\eta_6 + 6\eta_6^2 + 0.01\eta_1^3 + 0.02\eta_1^2\eta_2 + 0.08\eta_1^2\eta_3 \\
&\quad -0.1\eta_1^2\eta_4 - 0.5\eta_1^2\eta_5 + 0.6\eta_1^2\eta_6 - 0.1\eta_1\eta_2^2 + 0.06\eta_1\eta_2\eta_3 \\
&\quad -0.9\eta_1\eta_2\eta_4 - 0.2\eta_1\eta_2\eta_5 - 0.5\eta_1\eta_2\eta_6 - 0.3\eta_1\eta_3^2 - 2\eta_1\eta_3\eta_4 \\
&\quad -4\eta_1\eta_3\eta_5 - 1\eta_1\eta_3\eta_6 - 1\eta_1\eta_4^2 + 3\eta_1\eta_4\eta_5 - 0.6\eta_1\eta_4\eta_6 \\
&\quad 1\eta_1\eta_5^2 + 2\eta_1\eta_5\eta_6 - 2\eta_1\eta_6^2 - 0.3\eta_2^3 + 0.2\eta_2^2\eta_3 \\
&\quad -2\eta_2^2\eta_4 + 0.5\eta_2^2\eta_5 - 3\eta_2^2\eta_6 + 0.9\eta_2\eta_3^2 - 0.8\eta_2\eta_3\eta_4 \\
&\quad -9\eta_2\eta_3\eta_5 - 9\eta_2\eta_3\eta_6 - 6\eta_2\eta_4^2 - 1\eta_2\eta_4\eta_5 - 1 \times 10^1\eta_2\eta_4\eta_6 \\
&\quad -3\eta_2\eta_5^2 - 0.02\eta_2\eta_5\eta_6 - 2 \times 10^1\eta_2\eta_6^2 + 0.8\eta_3^3 + 1\eta_3^2\eta_4 \\
&\quad -1 \times 10^1\eta_3^2\eta_5 + 1\eta_3^2\eta_6 - 4\eta_3\eta_4^2 - 1 \times 10^1\eta_3\eta_4\eta_5 + 5\eta_3\eta_4\eta_6 \\
&\quad -1\eta_3\eta_5^2 - 3 \times 10^1\eta_3\eta_5\eta_6 - 6 \times 10^1\eta_3\eta_6^2 - 5\eta_4^3 + 1 \times 10^1\eta_4^2\eta_5 \\
&\quad -2 \times 10^1\eta_4^2\eta_6 + 2 \times 10^1\eta_4\eta_5^2 - 9 \times 10^1\eta_4\eta_5\eta_6 - 8 \times 10^1\eta_4\eta_6^2 + 7 \times 10^1\eta_5^3 \\
&\quad 1 \times 10^2\eta_5^2\eta_6 - 1 \times 10^2\eta_5\eta_6^2 + 2 \times 10^2\eta_6^3
\end{aligned}
$$

$$
\begin{aligned}
\dot{\eta}_4 &= 1\eta_1 + 2\eta_2 + 9\eta_3 - 0.8\eta_4 - 1\eta_5 \\
&\quad -5\eta_6 + 0.4\eta_1^2 + 2\eta_1\eta_2 + 3\eta_1\eta_3 + 0.2\eta_1\eta_4 \\
&\quad -5\eta_1\eta_5 - 0.7\eta_1\eta_6 + 2\eta_2^2 + 6\eta_2\eta_3 + 1\eta_2\eta_4 \\
&\quad -9\eta_2\eta_5 - 0.2\eta_2\eta_6 + 7\eta_3^2 - 0.01\eta_3\eta_4 - 2 \times 10^1\eta_3\eta_5 \\
&\quad -2\eta_3\eta_6 + 2\eta_4^2 + 3\eta_4\eta_5 + 1 \times 10^1\eta_4\eta_6 + 1 \times 10^1\eta_5^2 \\
&\quad 2 \times 10^1\eta_5\eta_6 + 2 \times 10^1\eta_6^2 - 0.008\eta_1^3 - 0.2\eta_1^2\eta_2 + 0.4\eta_1^2\eta_3 \\
&\quad -1\eta_1^2\eta_4 - 2\eta_1^2\eta_5 - 1\eta_1^2\eta_6 - 1\eta_1\eta_2^2 + 1\eta_1\eta_2\eta_3 \\
&\quad -6\eta_1\eta_2\eta_4 - 6\eta_1\eta_2\eta_5 - 6\eta_1\eta_2\eta_6 + 0.7\eta_1\eta_3^2 - 3\eta_1\eta_3\eta_4 \\
&\quad -9\eta_1\eta_3\eta_5 - 5\eta_1\eta_3\eta_6 - 5\eta_1\eta_4^2 - 1\eta_1\eta_4\eta_5 - 4\eta_1\eta_4\eta_6 \\
&\quad -1\eta_1\eta_5^2 - 2\eta_1\eta_5\eta_6 - 5\eta_1\eta_6^2 - 1\eta_2^3 + 0.7\eta_2^2\eta_3 \\
&\quad -7\eta_2^2\eta_4 - 4\eta_2^2\eta_5 - 8\eta_2^2\eta_6 + 4\eta_2\eta_3^2 - 8\eta_2\eta_3\eta_4 \\
&\quad -2 \times 10^1\eta_2\eta_3\eta_5 - 2 \times 10^1\eta_2\eta_3\eta_6 - 1 \times 10^1\eta_2\eta_4^2 - 4\eta_2\eta_4\eta_5 - 2 \times 10^1\eta_2\eta_4\eta_6 \\
&\quad -3\eta_2\eta_5^2 + 7\eta_2\eta_5\eta_6 - 2 \times 10^1\eta_2\eta_6^2 + 0.9\eta_3^3 + 7\eta_3^2\eta_4 \\
&\quad -1 \times 10^1\eta_3^2\eta_5 + 8\eta_3^2\eta_6 - 2 \times 10^1\eta_3\eta_4^2 - 6 \times 10^1\eta_3\eta_4\eta_5 - 2 \times 10^1\eta_3\eta_4\eta_6 \\
&\quad -3 \times 10^1\eta_3\eta_5^2 - 5 \times 10^1\eta_3\eta_5\eta_6 - 8 \times 10^1\eta_3\eta_6^2 - 8\eta_4^3 + 4 \times 10^1\eta_4^2\eta_5 \\
&\quad -1 \times 10^1\eta_4^2\eta_6 + 7 \times 10^1\eta_4\eta_5^2 - 4\eta_4\eta_5\eta_6 - 6 \times 10^1\eta_4\eta_6^2 + 9 \times 10^1\eta_5^3 \\
&\quad 2 \times 10^2\eta_5^2\eta_6 + 4 \times 10^1\eta_5\eta_6^2 + 4 \times 10^2\eta_6^3
\end{aligned}
$$

$$
\begin{aligned}
\dot{\eta}_5 &= -0.3\eta_1 - 0.9\eta_2 - 3\eta_3 - 3\eta_4 + 5\eta_5 \\
&\quad 1 \times 10^1\eta_6 - 0.06\eta_1^2 - 0.4\eta_1\eta_2 - 0.9\eta_1\eta_3 - 0.5\eta_1\eta_4 \\
&\quad 2\eta_1\eta_5 - 1\eta_1\eta_6 - 0.7\eta_2^2 - 2\eta_2\eta_3 - 1\eta_2\eta_4 \\
&\quad 4\eta_2\eta_5 - 3\eta_2\eta_6 - 3\eta_3^2 - 2\eta_3\eta_4 + 9\eta_3\eta_5 \\
&\quad -3\eta_3\eta_6 - 2\eta_4^2 + 2\eta_4\eta_5 - 1 \times 10^1\eta_4\eta_6 - 6\eta_5^2 \\
&\quad -2\eta_5\eta_6 - 9\eta_6^2 - 0.02\eta_1^3 - 0.03\eta_1^2\eta_2 - 0.1\eta_1^2\eta_3 \\
&\quad 0.2\eta_1^2\eta_4 + 0.7\eta_1^2\eta_5 - 0.8\eta_1^2\eta_6 + 0.2\eta_1\eta_2^2 - 0.04\eta_1\eta_2\eta_3 \\
&\quad 1\eta_1\eta_2\eta_4 + 0.1\eta_1\eta_2\eta_5 + 0.7\eta_1\eta_2\eta_6 + 0.5\eta_1\eta_3^2 + 2\eta_1\eta_3\eta_4 \\
&\quad 6\eta_1\eta_3\eta_5 + 2\eta_1\eta_3\eta_6 + 2\eta_1\eta_4^2 - 5\eta_1\eta_4\eta_5 + 0.7\eta_1\eta_4\eta_6 \\
&\quad -2\eta_1\eta_5^2 - 3\eta_1\eta_5\eta_6 + 4\eta_1\eta_6^2 + 0.5\eta_2^3 - 0.2\eta_2^2\eta_3 \\
&\quad 2\eta_2^2\eta_4 - 0.8\eta_2^2\eta_5 + 4\eta_2^2\eta_6 - 1\eta_2\eta_3^2 + 1\eta_2\eta_3\eta_4 \\
&\quad 1 \times 10^1\eta_2\eta_3\eta_5 + 1 \times 10^1\eta_2\eta_3\eta_6 + 9\eta_2\eta_4^2 + 2\eta_2\eta_4\eta_5 + 2 \times 10^1\eta_2\eta_4\eta_6 \\
&\quad 5\eta_2\eta_5^2 + 0.07\eta_2\eta_5\eta_6 + 4 \times 10^1\eta_2\eta_6^2 - 1\eta_3^3 - 2\eta_3^2\eta_4 \\
&\quad 2 \times 10^1\eta_3^2\eta_5 - 2\eta_3^2\eta_6 + 6\eta_3\eta_4^2 + 2 \times 10^1\eta_3\eta_4\eta_5 - 7\eta_3\eta_4\eta_6 \\
&\quad 0.9\eta_3\eta_5^2 + 5 \times 10^1\eta_3\eta_5\eta_6 + 8 \times 10^1\eta_3\eta_6^2 + 7\eta_4^3 - 2 \times 10^1\eta_4^2\eta_5 \\
&\quad 3 \times 10^1\eta_4^2\eta_6 - 2 \times 10^1\eta_4\eta_5^2 + 1 \times 10^2\eta_4\eta_5\eta_6 + 1 \times 10^2\eta_4\eta_6^2 - 1 \times 10^2\eta_5^3 \\
&\quad -2 \times 10^2\eta_5^2\eta_6 + 2 \times 10^2\eta_5\eta_6^2 - 3 \times 10^2\eta_6^3
\end{aligned}
$$

$$
\begin{aligned}
\dot{\eta}_6 &= 2\eta_1 + 4\eta_2 + 1 \times 10^1\eta_3 - 1\eta_4 - 2 \times 10^1\eta_5 \\
&\quad -9\eta_6 + 0.6\eta_1^2 + 3\eta_1\eta_2 + 5\eta_1\eta_3 + 0.6\eta_1\eta_4 \\
&\quad -8\eta_1\eta_5 - 1\eta_1\eta_6 + 3\eta_2^2 + 1 \times 10^1\eta_2\eta_3 + 2\eta_2\eta_4 \\
&\quad -2 \times 10^1\eta_2\eta_5 - 0.1\eta_2\eta_6 + 1 \times 10^1\eta_3^2 + 0.8\eta_3\eta_4 - 3 \times 10^1\eta_3\eta_5 \\
&\quad -2\eta_3\eta_6 + 3\eta_4^2 + 3\eta_4\eta_5 + 2 \times 10^1\eta_4\eta_6 + 2 \times 10^1\eta_5^2 \\
&\quad 2 \times 10^1\eta_5\eta_6 + 2 \times 10^1\eta_6^2 - 0.02\eta_1^3 - 0.4\eta_1^2\eta_2 + 0.7\eta_1^2\eta_3 \\
&\quad -2\eta_1^2\eta_4 - 3\eta_1^2\eta_5 - 2\eta_1^2\eta_6 - 2\eta_1\eta_2^2 + 2\eta_1\eta_2\eta_3 \\
&\quad -1 \times 10^1\eta_1\eta_2\eta_4 - 9\eta_1\eta_2\eta_5 - 1 \times 10^1\eta_1\eta_2\eta_6 + 1\eta_1\eta_3^2 - 5\eta_1\eta_3\eta_4 \\
&\quad -2 \times 10^1\eta_1\eta_3\eta_5 - 8\eta_1\eta_3\eta_6 - 9\eta_1\eta_4^2 - 3\eta_1\eta_4\eta_5 - 7\eta_1\eta_4\eta_6 \\
&\quad -0.7\eta_1\eta_5^2 - 5\eta_1\eta_5\eta_6 - 1 \times 10^1\eta_1\eta_6^2 - 2\eta_2^3 + 1\eta_2^2\eta_3 \\
&\quad -1 \times 10^1\eta_2^2\eta_4 - 7\eta_2^2\eta_5 - 1 \times 10^1\eta_2^2\eta_6 + 8\eta_2\eta_3^2 - 1 \times 10^1\eta_2\eta_3\eta_4 \\
&\quad -4 \times 10^1\eta_2\eta_3\eta_5 - 4 \times 10^1\eta_2\eta_3\eta_6 - 2 \times 10^1\eta_2\eta_4^2 - 6\eta_2\eta_4\eta_5 - 4 \times 10^1\eta_2\eta_4\eta_6 \\
&\quad -2\eta_2\eta_5^2 + 5\eta_2\eta_5\eta_6 - 3 \times 10^1\eta_2\eta_6^2 + 1\eta_3^3 + 1 \times 10^1\eta_3^2\eta_4 \\
&\quad -2 \times 10^1\eta_3^2\eta_5 + 1 \times 10^1\eta_3^2\eta_6 - 3 \times 10^1\eta_3\eta_4^2 - 9 \times 10^1\eta_3\eta_4\eta_5 - 4 \times 10^1\eta_3\eta_4\eta_6 \\
&\quad -4 \times 10^1\eta_3\eta_5^2 - 7 \times 10^1\eta_3\eta_5\eta_6 - 1 \times 10^2\eta_3\eta_6^2 - 1 \times 10^1\eta_4^3 + 6 \times 10^1\eta_4^2\eta_5 \\
&\quad -2 \times 10^1\eta_4^2\eta_6 + 1 \times 10^2\eta_4\eta_5^2 + 3 \times 10^1\eta_4\eta_5\eta_6 - 1 \times 10^2\eta_4\eta_6^2 + 1 \times 10^2\eta_5^3 \\
&\quad 4 \times 10^2\eta_5^2\eta_6 + 1 \times 10^2\eta_5\eta_6^2 + 6 \times 10^2\eta_6^3
\end{aligned}
$$

FIG. 26. Polynomial 6D ODE SSM-reduced model for the full system (13), with coefficients rounded to one significant digit.

small enough, since $\gamma \notin |\sigma(U)|$. Hence, for $u \in X$ and $s \in \mathbb{R}$ fixed, (C8) implies the existence of a $C > 0$ such that

$$|\Phi_s^n(u) - \Phi_s^n(\pi_s(u))| < C\gamma^n \quad \text{for all } n \in \mathbb{N}.$$

For $t \geq s$, there exists a unique $n \in \mathbb{N}$ for which $s + np \leq t < s + (n+1)p$. Therefore, using Lipschitzness of $S_\rho(t, s; \cdot)$ once more,

$$\begin{aligned}
|S_\rho(t, s; u) - S_\rho(t, s; \pi_s(u))| &\leq \widetilde{C}|\Phi_s^n(u) - \Phi_s^n(\pi_s(u))| \\
&< C\widetilde{C}\gamma^n \\
&\leq \hat{C}e^{(t-s)\ln(\gamma)/p}.
\end{aligned}$$

The local version follows as above. □

Remark 1: Note that, instead of considering (C3), we could have also considered the integral equation obtained by considering R as a perturbation above $\{U(t, s)\}_{t \geq s}$, using a sun-star calculus for $\{U(t, s)\}_{t \geq s}$. This would have enabled a more elegant proof conducted entirely in the time-dependent setting, without the need to appeal to Poincaré maps, just as in the case of periodic center manifolds.[55] Since we do not wish to derive rigorous formulas for the computation of manifold coefficients here (our example is dealt with in a data-driven setting), Theorem 2 suffices.

APPENDIX D: MACKEY-GLASS SSM-REDUCED DYNAMICS

Figure 26 reports the polynomial SSM-reduced dynamics identified from data for the Mackey–Glass system (13), discussed in Sec. IV B.

REFERENCES

[1] S. M. Al-Tuwairqi and S. K. Al-Harbi, "A time-delayed model for the spread of COVID-19 with vaccination," Sci. Rep. **12**, 19435 (2022).

[2] B. Szaksz, G. Orosz, and G. Stépán, "Reduction to spectral submanifolds in guided car-following with time delay," IFAC-PapersOnLine **58**(27), 67–72 (2024).

[3] B. Szaksz, G. Orosz, and G. Stépán, "Discretization based spectral submanifolds in guided car-following with time delay," IFAC-PapersOnLine **59**(13), 165–170 (2025).

[4] G. Orosz and T. G. Molnár, *Dynamics and Control of Connected Vehicles*, Surveys and Tutorials in the Applied Mathematical Sciences, 1st ed. (Springer, 2025).

[5] G. Stépán, J. G. Milton, and T. Insperger, "Quantization improves stabilization of dynamical systems with delayed feedback," Chaos **27**(11), 114306 (2017).

[6] T. Insperger and G. Stépán, *Semi-Discretization for Time-Delay Systems* (Springer, 2011), Vol. 178.

[7] M. B. Vizi, and G. Stépán, "Digital stability of the furuta pendulum based on angle detection," J. Vib. Control **30**, 588–597 (2024).

[8] T. Insperger, J. Milton, and G. Stépán, "Semi-discretization and the time-delayed PDA feedback control of human balance," IFAC-Pap. OnLine **48**, 93–98 (2015).

[9] G. Buza and G. Haller, "Existence of spectral submanifolds in time delay systems," J. Nonlin. Sci. (in press) (2025).

[10] M. C. Mackey and L. Glass, "Oscillation and chaos in physiological control systems," Science **197**(4300), 287–289 (1977).

[11] G. Haller, *Modeling Nonlinear Dynamics from Equations and Data–with Applications to Solids, Fluids, and Controls*, Computational Science & Engineering (Society for Industrial and Applied Mathematics, 2025), see https://doi.org/10.1137/1.9781611978353.

[12] G. Haller and S. Ponsioen, "Nonlinear normal modes and spectral submanifolds: Existence, uniqueness and use in model reduction," Nonlinear Dyn. **86**(3), 1493–1534 (2016).

[13] M. Cenedese, J. Axås, B. Bäuerlein, K. Avila, and G. Haller, "Data-driven modeling and prediction of non-linearizable dynamics via spectral submanifolds," Nat. Commun. **13**(1), 872 (2022).

[14] B. Kaszás and G. Haller, "Capturing the edge of chaos as a spectral submanifold in pipe flows," J. Fluid Mech. **979**, A48 (2024).

[15] B. Kaszás and G. Haller, "Joint reduced model for the laminar and chaotic attractors in plane couette flow," J. Fluid Mech. **1023**, A1 (2025).

[16] J. Axås, B. Bäuerlein, K. Avila, and G. Haller, "Data-driven modeling of subharmonic forced response due to nonlinear resonance," Sci. Rep. **14**(1), 25991 (2024).

10 November 2026 11:30:50

© Author(s) 2026

[17]L. Bettini, M. Cenedese, and G. Haller, "Model reduction to spectral submanifolds in piecewise smooth dynamical systems," Int. J. Nonlinear Mech. **163**, 104753 (2024).
[18]A. A. Morsy, Z. Xu, P. Tiso, and G. Haller, "Data-driven reduction of the finite-element model of a tribomechadynamics benchmark problem," Nonlinear Dyn. **113**, 24539–24555 (2025).
[19]G. Abbasciano, B. Endrész, G. Stépán, and G. Haller, "Data-driven modeling of global bifurcations and chaos in a mechanical system under delayed and quantized control," J. Sound Vib. **628**, 119660 (2026).
[20]J. I. Alora, M. Cenedese, E. Schmerling, G. Haller, and M. Pavone, "Data-driven spectral submanifold reduction for nonlinear optimal control of high-dimensional robots," arXiv (2022).
[21]J. I. Alora, M. Cenedese, E. Schmerling, G. Haller, and M. Pavone, "Practical deployment of spectral submanifold reduction for optimal control of high-dimensional systems," IFAC-PapersOnLine **56**(2), 4074–4081 (2023).
[22]J. I. Alora, M. Cenedese, G. Haller, and M. Pavone, "Discovering dominant dynamics for nonlinear continuum robot control," npj Robot. **3**, 5 (2025).
[23]R. S. Kaundinya, J. I. Alora, J. G. Matt, L. A. Pabon, M. Pavone, and G. Haller, "Data-driven soft robot control via adiabatic spectral submanifolds," arXiv:2503.10919 (2025).
[24]L. Bettini, A. Kazemipour, R. K. Katzschmann, and G. Haller, "Nonlinear spectral modeling and control of soft-robotic muscles from data," arXiv:2601.03247 (2026).
[25]J. King, B. Kaszás, G. Buza, W. Jussiau, and G. Haller, "Parametric spectral submanifolds across hopf bifurcations with applications to fluid dynamics," arXiv:2603.19079 (2026).
[26]G. Stépán and G. Haller, "Quasiperiodic oscillations in robot dynamics," Nonlinear Dyn. **8**(4), 513–528 (1995).
[27]O. Diekmann, S. M. Verduyn Lunel, S. A. van Gils, and H.-O. Walther, *Delay Equations: Functional-, Complex-, and Nonlinear Analysis*, Applied Mathematical Sciences Vol. 110 (Springer, 1995).
[28]B. Szaksz, G. Orosz, and G. Stépán, "Spectral submanifolds in time delay systems," Nonlinear Dyn. **113**, 14265–14286 (2025).
[29]S. L. Brunton, J. L. Proctor, and J. N. Kutz, "Discovering governing equations from data by sparse identification of nonlinear dynamical systems," Proc. Natl. Acad. Sci. **113**(15), 3932–3937 (2016).
[30]X. A. Ji and G. Orosz, "Learning time delay systems with neural ordinary differential equations," IFAC-PapersOnLine **55**(36), 79–84 (2022).
[31]X. A. Ji and G. Orosz, "Learn from one and predict all: Single trajectory learning for time delay systems," Nonlinear Dyn. **112**(5), 3505–3518 (2024).
[32]D. Breda, X. A. Ji, G. Orosz, and M. Tanveer, "Data-driven methods for delay differential equations," arXiv:2512.04894 (2025).
[33]A. Pecile, N. Demo, M. Tezzele, G. Rozza, and D. Breda, "Data-driven discovery of delay differential equations with discrete delays," J. Comput. Appl. Math. **461**, 116439 (2025).
[34]A. Sandoz, V. Ducret, G. A. Gottwald, G. Vilmart, and K. Perron, "Sindy for delay-differential equations: Application to model bacterial zinc response," Proc. R. Soc. A **479**, 20220556 (2023).
[35]A. Pazy, *Semigroups of Linear Operators and Applications to Partial Differential Equations*, Applied Mathematical Sciences Vol. 44 (Springer-Verlag, 1983).
[36]R. Szalai, "Invariant spectral foliations with applications to model order reduction and synthesis," Nonlinear Dyn. **101**, 2645–2669 (2020).
[37]L. Bettini, B. Kaszás, B. Zybach, J. Dual, and G. Haller, "Data-driven nonlinear model reduction to spectral submanifolds via oblique projection," Chaos **35**(4), 043135 (2025).
[38]L. Bettini, A. Kazemipour, R. K. Katzschmann, and G. Haller, "General oblique projections for model reduction via spectral submanifolds," Chaos **36**(5), 053122 (2026).
[39]F. Takens, "Detecting strange attractors in turbulence," in *Dynamical Systems and Turbulence, Warwick 1980* (Springer, 1981), Vol. 898, pp. 366–381.
[40]P. Grassberger and I. Procaccia, "Measuring the strangeness of strange attractors," Phys. D **9**(1-2), 189–208 (1983).
[41]T. Sauer, J. A. Yorke, and M. Casdagli, "Embedology," J. Stat. Phys. **65**(3-4), 579–616 (1991).
[42]G. Nastac, J. W. Labahn, L. Magri, and M. Ihme, "Lyapunov exponent as a metric for assessing the dynamic content and predictability of large-eddy simulations," Phys. Rev. Fluids **2**(9), 094606 (2017).
[43]A. Liu, J. Axås, and G. Haller, "Data-driven modeling and forecasting of chaotic dynamics on inertial manifolds constructed as spectral submanifolds," Chaos **34**(3), 033140 (2024).
[44]Z. Xu, B. Kaszás, M. Cenedese, G. Berti, F. Coletti, and G. Haller, "Data-driven modelling of the regular and chaotic dynamics of an inverted flag from experiments," J. Fluid Mech. **987**, R7 (2024).
[45]J. Axås, and G. Haller, "Model reduction for nonlinearizable dynamics via delay-embedded spectral submanifolds," Nonlinear Dyn. **111**, 22079–22099 (2023).
[46]A. Yang, J. Axås, F. Kádár, G. Stépán, and G. Haller, "Modeling nonlinear dynamics from videos," Nonlinear Dyn. **113**, 10881–10909 (2025).
[47]G. E. Hutchinson, "Circular causal systems in ecology," Ann. N. Y. Acad. Sci. **50**(4), 221–246 (1948).
[48]Z. Xu, R. S. Kaundinya, S. Jain, and G. Haller, "Nonlinear model reduction to random spectral submanifolds in random vibrations," J. Sound Vib. **600**, 118923 (2025).
[49]P. Appeltans, H. Silm, and W. Michiels, "TDS-CONTROL: A MATLAB package for the analysis and controller-design of time-delay systems," IFAC-PapersOnLine **55**(16), 272–277 (2022).
[50]P. Appeltans and W. Michiels, "Analysis and controller-design of time-delay systems using TDS-CONTROL: A tutorial and manual," arXiv:2305.00341 (2023).
[51]J. M. Cushing, "Time delays in single species growth models," J. Math. Biol. **4**(3), 257–264 (1977).
[52]G. Haller and G. Stépán, "Micro-chaos in digital control," J. Nonlinear Sci. **6**, 415–448 (1996).
[53]Y. Hino, S. Murakami, and T. Naito, *Functional Differential Equations with Infinite Delay*, Lecture Notes in Mathematics Vol. 1473 (Springer-Verlag, 1991).
[54]J. Axås, M. Cenedese, and G. Haller, "Fast data-driven model reduction for nonlinear dynamical systems," Nonlinear Dyn. **111**(9), 7941–7957 (2023).
[55]B. Lentjes, L. Spek, M. M. Bosschaert, and Y. A. Kuznetsov, "Periodic center manifolds for DDEs in the light of suns and stars," J. Dyn. Differ. Equ. **37**(1), 815–858 (2025).
[56]T. Kato, *Perturbation Theory for Linear Operators*, Grundlehren der mathematischen Wissenschaften Vol. 132 (Springer, Berlin, 2013), see https://doi.org/10.1007/978-3-662-12678-3.
[57]X.-Y. Chen, J. K. Hale, and B. Tan, "Invariant foliations for C^1 semigroups in Banach spaces," J. Differ. Equ. **139**, 283–318 (1997).
[58]T. Bühler, and D. A. Salamon, *Functional Analysis*, Graduate Studies in Mathematics Vol. 191 (American Mathematical Society, Providence, RI, 2018).
[59]M. C. Irwin, "A new proof of the pseudostable manifold theorem," J. Lond. Math. Soc. **s2-21**, 557–566 (1980).
[60]G. Buza, "Spectral submanifolds of the Navier–Stokes equations," SIAM J. Appl. Dyn. Syst. **23**, 1052–1089 (2024).
[61]G. Haller (2022). "SSMLearn," GitHub. https://github.com/haller-group/SSMLearn.

10 November 2026 11:30:50

© Author(s) 2026